The H2O Southern Galactic Plane Survey (HOPS) - I. Techniques and H2O maser data

A. J. Walsh, S. L. Breen, T. Britton, K. J. Brooks, M. G. Burton, M. R. Cunningham, J. A. Green, L. Harvey-Smith, L. Hindson, M. G. Hoare, et al.

Monthly Notices of the ROYAL ASTRONOMICAL SOCIETY

Mon. Not. R. Astron. Soc. **416,** 1764–1821 (2011) doi:10.1111/j.1365-2966.2011.19115.x

The H_2O Southern Galactic Plane Survey (HOPS) – I. Techniques and H_2O maser data

A. J. Walsh,[1⋆] S. L. Breen,[2] T. Britton,[2] K. J. Brooks,[2] M. G. Burton,[3] M. R. Cunningham,[3] J. A. Green,[2] L. Harvey-Smith,[2] L. Hindson,[2,4] M. G. Hoare,[5] B. Indermuehle,[2] P. A. Jones,[2,6] N. Lo,[6,7] S. N. Longmore,[8,9] V. Lowe,[2,3] C. J. Phillips,[2] C. R. Purcell,[5] M. A. Thompson,[4] J. S. Urquhart,[2] M. A. Voronkov,[2] G. L. White[1] and M. T. Whiting[2]

[1]*School of Engineering and Physical Sciences, James Cook University, Townsville, QLD 4811, Australia*
[2]*CSIRO Astronomy and Space Science, PO Box 76, Epping, NSW 1710, Australia*
[3]*School of Physics, University of New South Wales, Sydney, NSW 2052, Australia*
[4]*Centre for Astrophysics Research, Science and Technology Research Institute, University of Hertfordshire, Hatfield AL10 9AB*
[5]*School of Physics and Astronomy, University of Leeds, Leeds LS2 9JT*
[6]*Departamento de Astronomía, Universidad de Chile, Casilla 36-D, Santiago, Chile*
[7]*Laboratoire AIM Paris-Saclay, CEA/Irfu – Uni. Paris Didérot – CNRS/INSU, 91191 Gif-sur-Yvette, France*
[8]*Harvard–Smithsonian Center for Astrophysics, 60 Garden Street, Cambridge, MA 02138, USA*
[9]*European Southern Observatory, Karl Schwarzchildstrasse 2, Garching 85748, Germany*

Accepted 2011 May 19. Received 2011 May 17; in original form 2011 April 14

ABSTRACT

We present first results of the H_2O Southern Galactic Plane Survey (HOPS), using the Mopra Radio Telescope with a broad-band backend and a beam size of about 2 arcmin. We have observed 100 deg^2 of the southern Galactic plane at 12 mm (19.5–27.5 GHz), including spectral line emission from H_2O masers, multiple metastable transitions of ammonia, cyanoacetylene, methanol and radio recombination lines. In this paper, we report on the characteristics of the survey and H_2O maser emission. We find 540 H_2O masers, of which 334 are new detections. The strongest maser is 3933 Jy and the weakest is 0.7 Jy, with 62 masers over 100 Jy. In 14 maser sites, the spread in the velocity of the H_2O maser emission exceeds 100 km s^{-1}. In one region, the H_2O maser velocities are separated by 351.3 km s^{-1}. The rms noise levels are typically between 1 and 2 Jy, with 95 per cent of the survey under 2 Jy. We estimate completeness limits of 98 per cent at around 8.4 Jy and 50 per cent at around 5.5 Jy. We estimate that there are between 800 and 1500 H_2O masers in the Galaxy that are detectable in a survey with similar completeness limits to HOPS. We report possible masers in NH_3 (11,9) and (8,6) emission towards G19.61−0.23 and in the NH_3 (3,3) line towards G23.33−0.30.

Key words: masers – surveys – stars: formation – ISM: molecules – Galaxy: structure – radio lines: ISM.

1 INTRODUCTION

Understanding how the interstellar medium (ISM) is linked to stellar birth and death in our Galaxy is a major problem in astrophysics today. In order to understand the processes involved, it is often useful to conduct large-scale Galactic plane surveys. Such surveys, as the International Galactic Plane Survey (Taylor et al. 2003; McClure-Griffiths et al. 2005; Stil et al. 2006) in H I, as well as surveys of ^{12}CO (Dame, Hartmann & Thaddeus 2001) and ^{13}CO (Jackson et al. 2006), have been widely used in tracing out Galactic structure and motions, but these popular tracers are typically insensitive to a high-density gas. In order to understand the processes at the beginning of star formation, where gas and dust have accumulated to high-density regions, it is necessary to choose a tracer of such high densities, as well as other signposts of star formation activity.

We have completed a survey of 100 deg^2 of the southern Galaxy in multiple spectral lines, using the Mopra Radio Telescope in the 12 mm band (HOPS – The H_2O southern Galactic Plane Survey). Our main target lines are the H_2O ($6_{1,6}$–$5_{2,3}$) maser line, NH_3 (1, 1), (2, 2) and (3, 3) inversion transitions, radio recombination lines H62α and H69α and HCCCN (3–2).

H_2O masers are an important signpost of unusual astrophysical conditions such as outflows and shocked gas. They are known to

⋆E-mail: andrew.walsh@jcu.edu.au

occur in both high- and low-mass star-forming regions (e.g. Claussen et al. 1996; Forster & Caswell 1999), late M-type stars (Dickinson 1976), planetary nebulae (Miranda et al. 2001), Mira variables (Hinkle & Barnes 1979), asymptotic giant branch (AGB) stars (Barlow et al. 1996) and the centres of active galaxies (Claussen et al. 1984). The majority of currently known H_2O masers are found towards regions of star formation within our Galaxy. However, an untargeted survey is required to determine the relative occurrence of bright H_2O masers with other types of astrophysical objects. There is some evidence that within star-forming regions, H_2O masers may be observable at very early stages (e.g. Forster & Caswell 2000) of evolution. There is evidence that methanol masers may also be visible at these early stages (e.g. Walsh et al. 1998). The relative occurrence of these two masers can be assessed through the two untargeted surveys: the Methanol Multibeam Survey (Green et al. 2009) and HOPS, described in this paper. Recent research has focused on determining parallax distances to H_2O masers (e.g. Imai et al. 2007). A long-term goal is to accurately establish the dimensions of our Galaxy using bright maser sources throughout the Galaxy (e.g. Reid et al. 2009). It is hoped that the bright H_2O masers discovered in HOPS may be used for such distance determinations.

Thermal NH_3 emission in our Galaxy typically traces the high-density gas ($\sim 10^4$ cm^{-3}; Evans 1999). Properties of NH_3 spectral line emission can be used to understand the physical conditions of the gas. Lower order (J, K) inversion transitions of NH_3 commonly display a hyperfine structure (e.g. Ho & Townes 1983), which can be used to calculate the optical depth of the emission, to reduce confusing factors of optically thick emission, when trying to measure the total column density of the gas. Multiple inversion transitions of NH_3 are also commonly seen, which can be used to estimate the temperature of the excited gas. These inversion transitions occur within a few GHz of each other, making it possible to observe them simultaneously with the same telescope and a similar setup. This greatly eliminates sources of uncertainty when comparing multiple transitions, which in turn makes interpretation more reliable.

In cold, dense regions most molecules and ions are known to freeze out on to dust grains, with CO, CS and HCO^+ being classic examples (Bergin & Langer 1997; Willacy, Langer & Velusamy 1998; Caselli et al. 1999; Tafalla et al. 2002; Bergin et al. 2002). Thus, such species are unreliable tracers of the densest and coldest regions in our Galaxy. CO also has a low-effective critical density $\sim 10^2$ cm^{-3} (Evans 1999) making it a better tracer of the diffuse gas and susceptible to becoming optically thick in dense regions. CO, CS and HCO^+ are also known to be good tracers of outflow activity in star-forming regions. Therefore, a Galactic map of emission in these tracers can be difficult to interpret in terms of identifying the quiescent gas. On the other hand, NH_3 appears to be more robust than CO, CS or HCO^+ against freeze-out on to dust grains (e.g. Aikawa et al. 2001). This means that NH_3 can be used to probe the colder denser regions. In addition to this, N_2H^+, which is found under conditions very similar to NH_3, is known to avoid regions of outflow (e.g. Walsh et al. 2007b), tracing only the quiescent gas on large scales. This makes NH_3 a very reliable tracer of the cool, dense gas. Combined with the information derived from the NH_3 hyperfine structure and multiple inversion transitions, NH_3 can be used to reliably characterize the dense, quiescent gas component of the ISM.

In this paper, we concentrate on describing the survey as well as presenting the global properties of the H_2O maser data. In Paper II (Purcell et al. in preparation) we will present the NH_3 (1, 1) and (2, 2) data and the cloud catalogue as well as describe the emission-finding algorithm. Paper III (Longmore at al. in preparation) will detail the thermal line-fitting routines used on the NH_3 data and will present the physical properties of the unresolved clouds in the catalogue. Results from other spectral lines will be reported in later papers. In the follow-up work, we will accurately measure the positions of the H_2O masers using the Australia Telescope Compact Array (ATCA).

2 MOPRA CHARACTERIZATION

The Australia Telescope National Facility's Mopra Telescope is a 22-m antenna located 26 km outside the town of Coonabarabran in New South Wales, Australia. It is at an elevation of 850 m above sea level and at a latitude of 31° south.

The receivers use Indium Phosphide High Electron Mobility Transistor Monolithic Microwave Integrated Circuits as the amplifying elements. The receiver systems require no tuning and include noise diodes for system temperature determination. The nominal operating range for the 12 mm receiver is from 16 to 27 GHz; however, we have found that the receiver still performs well at frequencies as high as 27.5 GHz. Further general information on Mopra can be found in Urquhart et al. (2010).

2.1 The Mopra Spectrometer

The Mopra Spectrometer (MOPS) is the digital filterband backend used for the observations. It comprises a total bandwidth of 8.3 GHz, split into four overlapping intermediate frequencies (IFs), each with a width of 2.2 GHz. MOPS can be configured in two modes: either broadband mode, where the full 8.3 GHz is available, or in zoom mode, which was used for HOPS. In the zoom mode, each of the four IFs contains four zoom bands of 137.5 MHz each, available to take spectra. The positioning of the four 137.5 MHz zoom bands within each IF is highly flexible, which allows the user to observe virtually any of up to four spectral windows within each 2.2 GHz IF. Thus, it is possible to simultaneously observe up to 16 spectral windows throughout the full 8.3 GHz bandwidth. Each spectral window consists of 4096 channels, which is equivalent to a bandwidth and velocity resolution of 2114 and 0.52 km s^{-1} at 19.5 GHz or 1499 and 0.37 km s^{-1} at 27.5 GHz, respectively. Table 1 gives the details of centre frequencies for each band we observed, as well as the stronger spectral lines found within the bands.

For the H_2O maser observations, two contiguous bands (5 and 6) can be used together to search for masers in the velocity range of -2424 to $+1216$ km s^{-1}. At the H_2O maser frequency, each channel corresponds to 0.45 km s^{-1}.

2.2 Mopra beam shape

Bright water masers can be used to assess the shape of the Mopra beam at 22 GHz. However, due to their highly variable nature, water masers are not used to determine the efficiency of the telescope. The bright water maser G331.51−0.09 was mapped as part of HOPS. The strongest emission is found in the spectral channel at velocity −89.02 km s^{-1} and is shown in Fig. 1. This figure shows two diffraction rings around the maser peak. We note that a secondary water maser site (G331.44−0.19) coincides with the outer ring from G331.51−0.09 and can be seen in Fig. 1. There is also a maser (G331.56−0.12) that is located close to the inner ring, but the maser emission is not significant at this radial velocity and is thus not seen in the figure. Due to the confusion with G331.44−0.19, we do not fit the rings around G331.51−0.09. Instead, the maser G330.96−0.18, shown in Fig. 1, is used, which also shows the inner

Table 1. MOPS zoom band settings and strong lines found in each band. The first column lists the MOPS band number, with the total frequency range covered given in the second column. The third column lists the spectral lines that we might detect in HOPS. The spectral line frequency is given in Column 5. Column 6 indicates whether the spectral line is a thermal line, a maser line or both. The last column gives the reference for the spectral line frequency. Spectral lines that were detected in HOPS are shown in bold.

Band	Frequency Range covered (MHz)	Spectral line	Frequency (MHz)	Maser or thermal[a]	Frequency reference
1	19518–19655	**H69α**	19 591.110	Thermal	Lilley & Palmer (1968)
2	19932–20069	CH_3OH ($2_{1,1}$–$3_{0,3}$)E	19 967.396	Maser (II)	Mehrotra, Dreizler & Mäder (1985)
3	20691–20828	**NH_3(8,6)**	20 719.221	Both	Poynter & Kakar (1975)
3	20691–20828	NH_3(9,7)	20 735.452	Thermal	Poynter & Kakar (1975)
3	20691–20828	NH_3(7,5)	20 804.830	Thermal	Poynter & Kakar (1975)
4	21036–21173	**NH_3(11,9)**	21 070.739	Both	Poynter & Kakar (1975)
4	21036–21173	NH_3(4,1)	21 134.311	Thermal	Poynter & Kakar (1975)
5	22145–22277	**H_2O ($6_{1,6}$–$5_{2,3}$)**	22 235.080	Maser	Kukolich (1969)
6	22278–22415	C_2S (2_1–1_0)	22 344.030	Thermal	Kaifu et al. (1987)
7	23037–23174	CH_3OH ($9_{2,7}$–$10_{1,10}$)A^+	23 121.024	Maser (II)	Mehrotra et al. (1985)
7	23037–23174	NH_3(2,1)	23 098.819	Thermal	Kukolich & Wofsky (1970)
8	23382–23519	**H65α**	23 404.280	Thermal	Lilley & Palmer (1968)
8	23382–23519	**CH_3OH ($10_{1,9}$–$9_{2,8}$)A^-**	23 444.778	Maser (I)	Mehrotra et al. (1985)
9	23658–23795	**NH_3(1,1)**	23 694.471	Thermal	Kukolich (1967)
9	23658–23795	**NH_3(2,2)**	23 722.634	Thermal	Kukolich (1967)
10	23796–23933	**NH_3(3,3)**	23 870.130	Both	Kukolich (1967)
11	24900–25037	**CH_3OH ($3_{2,1}$–$3_{1,2}$)E**	24 928.707	Maser (I)	Müller, Menten & Mäder (2004)
11	24900–25037	**CH_3OH ($4_{2,2}$–$4_{1,3}$)E**	24 933.468	Maser (I)	Gaines, Casleton & Kukolich (1974)
11	24900–25037	**CH_3OH ($2_{2,0}$–$2_{1,1}$)E**	24 934.382	Maser (I)	Gaines et al. (1974)
11	24900–25037	**CH_3OH ($5_{2,3}$–$5_{1,4}$)E**	24 959.079	Maser (I)	Mehrotra et al. (1985)
11	24900–25037	**CH_3OH ($6_{2,4}$–$6_{1,5}$)E**	25 018.123	Maser (I)	Mehrotra et al. (1985)
12	25038–25175	**CH_3OH ($7_{2,5}$–$7_{1,6}$)E**	25 124.872	Maser (I)	Mehrotra et al. (1985)
12	25038–25175	**NH_3(6,6)**	25 056.025	Both	Kukolich & Wofsky (1970)
13	26556–26693	**HC_5N (10–9)**	26 626.533	Thermal	Jennings & Fox (1982)
14	26832–26969	**H62α**	26 939.170	Thermal	Lilley & Palmer (1968)
14	26832–26969	CH_3OH ($12_{2,10}$–$12_{1,11}$)E	26 847.205	Maser (I)	Müller et al. (2004)
15	27246–27383	**HCCCN (3–2)**	27 294.078	Thermal	Lafferty & Lovas (1978)
16	27384–27521	**NH_3(9,9)**	27 477.943	Thermal	Poynter & Kakar (1975)
16	27384–27521	CH_3OH ($13_{2,11}$–$13_{1,12}$)E	27 472.501	Maser (I)	Müller et al. (2004)

[a] CH_3OH masers are identified as either Class I or II.

beam ring and does not appear to have any other confusing masers nearby.

In Fig. 2, we show an azimuthally averaged histogram for G330.96−0.09. The histogram shows both the inner and outer beam rings. The inner ring occurs at a radius of about 3.8 arcmin and contains approximately 14 per cent of the flux of the main peak. The outer ring occurs at about 8.3 arcmin and contains approximately 3.5 per cent of the flux of the main peak. We estimate the full width at half-maximum (FWHM) of the beam from the radial profile to be 2.2 arcmin.

Recent observations by Urquhart et al. (2010) of the water masers in Orion-KL have been used to characterize the Mopra Radio Telescope. We find that the positions and intensities of the rings, as well as the size of the beam that we derive above, agree well with their results.

2.3 Mopra efficiency and stability

We adopt values from Urquhart et al. (2010) for the main beam size (2.2 arcmin at 22.2 GHz), efficiency (0.54 at 22.2 GHz) and Jy K^{-1} conversion factor (12.5 at 22.2 GHz).

During the course of the HOPS observations, we regularly performed observations of a number of well-known line sources in the sky, including Orion. These observations were typically conducted once each night and consisted of a position switch with 2 min on-source integration. The standard HOPS zoom configuration was used (Table 1). The purpose of these observations is to assess the stability of the telescope system over time and through different observing conditions. Whilst the zoom configuration includes strong maser lines, especially the H_2O maser line, we did not use this line for our calibration as the intensity is known to vary with time (Felli et al. 2007). Instead, we found the strong radio recombination emission lines (H69α and H62α) well suited for calibration, as they are not expected to significantly vary in intensity over the time-scale of our observations.

We measure the integrated intensity of the lines by fitting the spectrum with a single Gaussian curve and determining the area under that curve, using standard routines in the ASAP software package.[1]

Fig. 3 shows the distribution of measured integrated intensities for both radio recombination lines throughout the observations. Filled circles indicate integrated intensities for the H69α line and open squares indicate integrated intensities for the H62α line. We might expect that if there is significant atmospheric attenuation, then the integrated intensities might be correlated with elevation and/or system temperature. However, Fig. 3 shows that the distribution of integrated intensities for each line does not appear to correlate with either elevation or system temperature, but Fig. 3 does show a scatter of integrated intensities. We calculate that the standard deviation of

[1] The ATNF Spectral Analysis Package; http://svn.atnf.csiro.au/trac/asap

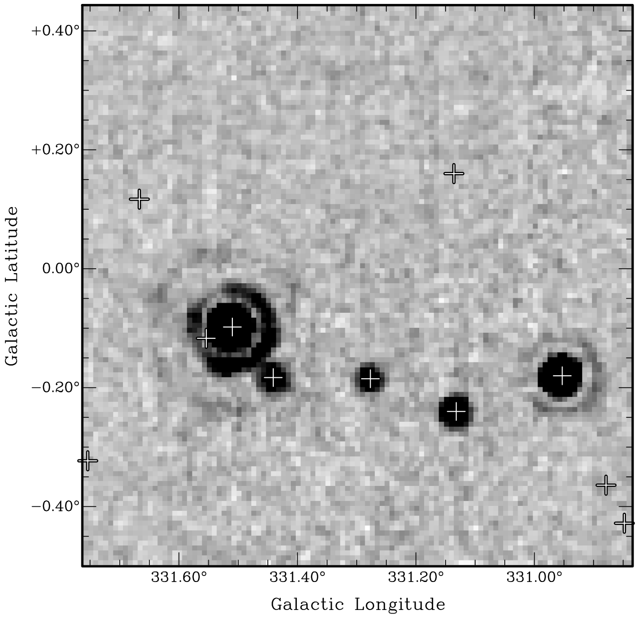

Figure 1. Water maser emission in one spectral channel at −89.02 km s^{-1}. Two strong masers can be seen: G331.51−0.09 (left) and G330.96−0.18 (right); both show diffraction rings. Plus symbols indicate the positions of identified water masers. Since the image is only a single channel of the data cube, not all masers are seen in the image, as they do not all emit at this velocity.

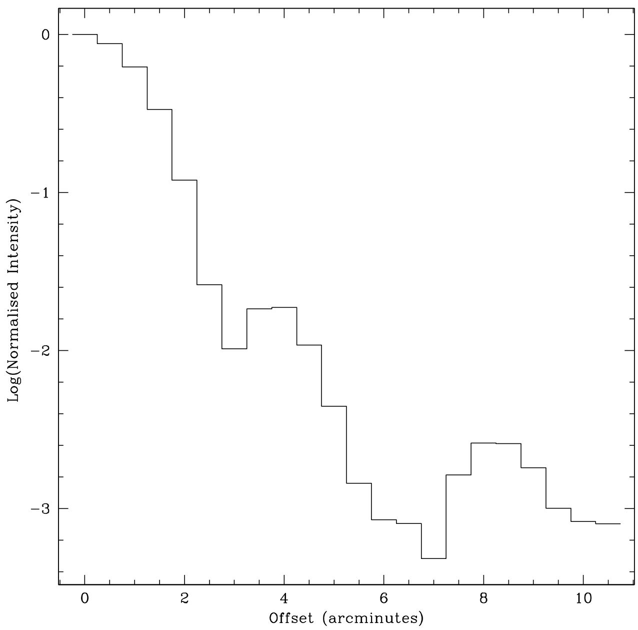

Figure 2. Azimuthally averaged beam profile around the water maser G330.96−0.18. The intensity scale has been normalized to the brightest pixel at the centre and is shown with a log scale on the *y*-axis.

integrated intensities is 15 per cent for H69α and 16 per cent for H62α. Thus, about 95 per cent (two standard deviations) of all integrated intensities are within 30 per cent of the mean integrated intensity. We assign 30 per cent as the uncertainty in the intensities of the HOPS data. Since the radio recombination line emission in Orion is extended, it is possible that the actual uncertainty is less than this as some of the scatter in Fig. 3 may be due to small pointing errors of the telescope. Thus, we consider 30 per cent as an upper limit.

Fig. 3 does show a significant difference in the integrated intensities of the two radio recombination lines, with the H62α line being weaker than the H69α line on average. Fig. 4 shows the distribution of the ratio of H69α/H62α integrated intensities for simultaneous observations. The mean of this distribution is 1.37, with a standard deviation of 0.07. This shows that the ratio of intensities appears stable over time. Therefore, whilst the absolute intensity scale may be uncertain by a factor of 30 per cent, the relative intensity scale of different spectral lines measured using simultaneous observations is likely to be no worse than 5 per cent. We note that the higher intensity of the H69α line compared to the H62α line is most likely because the beam at 19.6 GHz (the H69α line frequency) is larger than at 26.9 GHz (the H62α line frequency) and encompasses more extended radio recombination line emission.

3 SURVEY DESIGN

Previous observations of the Galactic plane in continuum (Schuller et al. 2009), thermal line (Dame et al. 2001; Jackson et al. 2006) and methanol maser emission (Walsh et al. 1998; Green et al. 2009) indicate that molecular material is concentrated in a region within about 30° in the Galactic longitude of the Galactic centre. The survey region for HOPS was tailored to cover the bulk of this emission, where the nominal survey region covered Galactic longitudes $290^\circ < l < 360^\circ$ and $0^\circ < l < 30^\circ$. The bulk of methanol masers (Walsh et al. 1998; Green et al. 2009) appear to be confined to within half a degree of the Galactic plane and H_2O and methanol masers are commonly found in the same star-forming regions, so the survey covered nominal Galactic latitudes from $-0.5^\circ < b < +0.5^\circ$. Our choice of survey region was also based on the amount of observing time that would be reasonably allocated in order to complete the project.

Based on our pilot observations (Walsh et al. 2008), we found the most suitable method was to divide the survey region into blocks of $0.5^\circ \times 0.5^\circ$. Each block was observed twice in the on-the-fly mapping mode, scanning once in Galactic longitude and once in Galactic latitude. Adjacent scans were separated by 51 arcsec to give Nyquist sampling of the beam at the highest observing frequency (27.5 GHz). At lower frequencies, the observations consequently oversample the mapped region. The scanning rate was 15 arcsec s^{-1} and spectra were stored every 2 s, giving a 30 arcsec spacing between spectra in each row. Each block requires about 2 h of continuous observations to complete. Thus, each square degree of the sky requires approximately 8 h to be fully observed. We calculate that each position was observed for effectively 1 min on-source using this method.

The positions of reference observations for the blocks of $0.5^\circ \times 0.5^\circ$ were chosen to typically lie at $b = +0.6^\circ$ or -0.6°, close to one corner of each block. Each reference position was initially checked for emission with a position-switch observation, with 2 min on-source integration time. Any potential reference position showing emission was discarded and a new reference position was chosen and checked in the same manner.

In order to minimize variations in sensitivity across the survey region, observations were generally limited to elevations of greater than 30°, although observations were occasionally made at slightly lower elevations during exceptionally good weather conditions. During good weather and at high elevation, typical system temperatures were 50 K at 19.5 GHz and 65 K at 27.5 GHz. We discarded all data with a system temperature of over 120 K. This upper

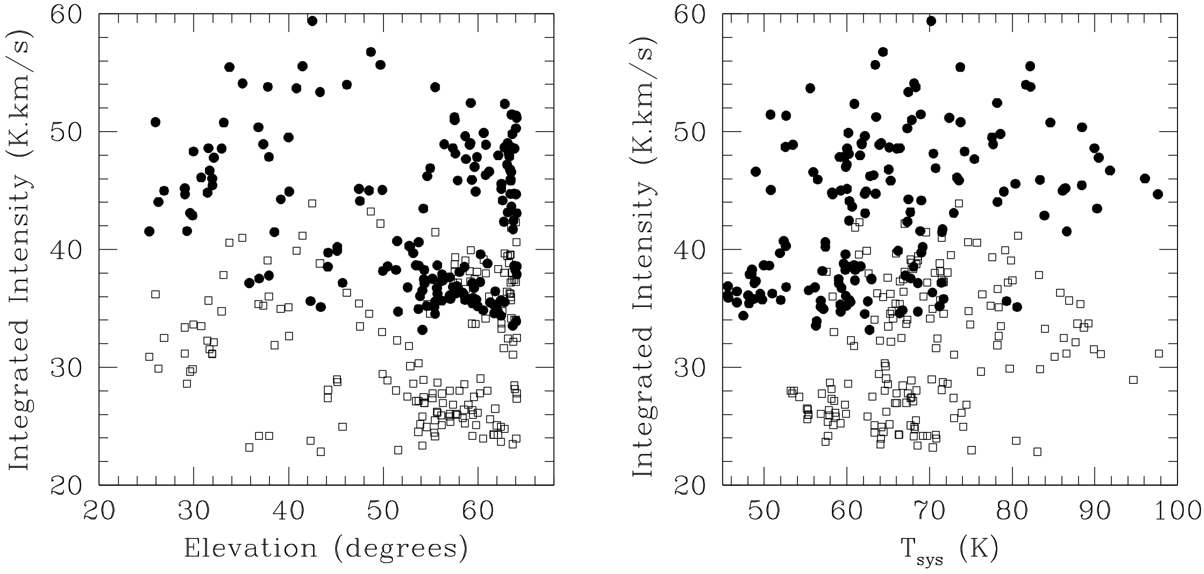

Figure 3. Distribution of integrated intensities for the H69α line (filled circles) and H62α line (open squares) in Orion, plotted against elevation (left) and system temperature (right). The distributions show that there is a spread of integrated intensities, implying that there is an inherent uncertainty in the HOPS absolute flux scale of about 30 per cent.

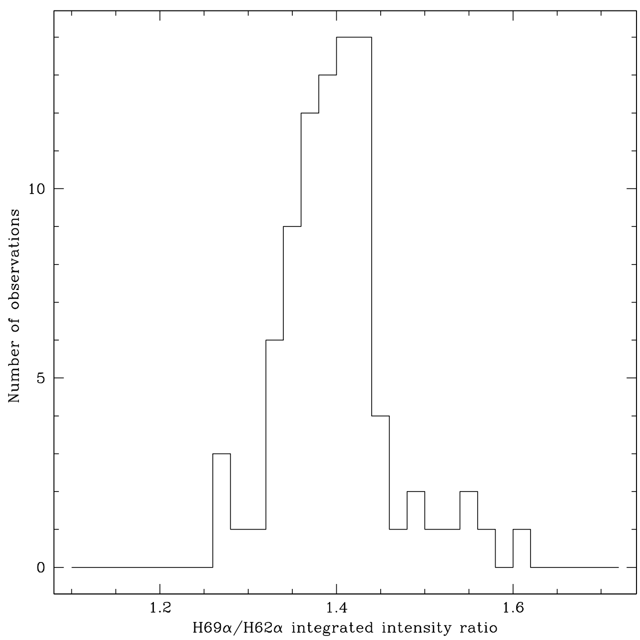

Figure 4. Distribution of the ratio of H69α/H62α integrated intensities in Orion. The ratio has a mean of 1.37 and standard deviation of 0.07, showing that the ratio of intensities is well defined.

limit was usually reached when observing through average weather conditions close to an elevation of 30° or during poor weather conditions. We also discarded data where the system temperature varied quickly due to clouds passing through the telescope beam. Such variations were typically of 20 K or greater and had the effect of producing striped features in the reduced data.

Pointing observations were conducted at the start of the survey at a variety of positions across the sky. We found that the global pointing model of Mopra was never more than 15 arcsec from the true position. We estimate that for the majority of HOPS observations the pointing was better than 10 arcsec, which is less than 10 per cent of the beamwidth. Consequently, regular pointing updates were not used in favour of the global pointing model.

4 DATA REDUCTION

Data were initially reduced using LIVEDATA and GRIDZILLA,[2] which are both AIPS++ packages written for the Parkes Radio Telescope and adapted for Mopra. LIVEDATA performs a bandpass calibration for each row along the scanning direction, using the preceding reference scan. A first-order polynomial (i.e. a straight line) is fitted to the baseline and then subtracted. In order to minimize the effects of noisy channels at the start and end of each zoom window, the first and last 150 channels were masked before performing the baseline fitting.

GRIDZILLA regrids and combines the data from multiple scanning directions on to a data cube. We chose to regrid on to pixels of 30 × 30 arcsec. Data were automatically weighted according to their system temperature, and data with system temperatures above 120 K were discarded. Data cubes were then processed in MIRIAD to smooth and/or bin the data, before the creation of peak temperature maps, which were used to find sources of emission. Peak temperature maps are created in MIRIAD, using the 'moment=-2' option in the task MOMENT. Peak temperature maps are two-dimensional maps similar to moment zero (integrated intensity) maps more commonly used in radio astronomy, but each pixel in the two-dimensional peak temperature map corresponds to the highest intensity pixel of the spectrum from the full data cube, at each position on the sky. We found that the peak temperature maps were more sensitive than moment zero maps in detecting weak emission, especially with imperfect baselines and wide bandwidths that were features of the HOPS data.

[2] Developed by Mark Calabretta: http://www.atnf.csiro.au/people/mcalabre/livedata.html

5 SOURCE FINDING

We employed a variety of methods to detect H_2O maser emission. These same methods were used to detect other rarer masers (see Section 7.3). Initially, we smoothed the data with a 90 × 90 arcsec two-dimensional Gaussian kernel. We found that this size effectively reduced the noise by about 15 per cent, compared to the maser emission. This kernel is slightly smaller than the size of the beam (132 arcsec); however, we found that a smoothing kernel the size of the beam produced maps that were not as sensitive to identifying weak masers.

After smoothing, the data were converted to peak temperature maps. These maps were visually inspected for maser candidates. Masers were initially identified by inspecting the spectrum at the position of a maser candidate in the peak temperature map and looking for a peak that contained at least two adjacent channels where at least one channel was greater than three times the rms noise level and where the sum of all emission channels was greater than five times the rms noise level. These values were chosen as they appear to give the best efficiency for detection of real features, with little contamination. Any weak maser candidates were then followed up with a position-switch observation, with 2 min on-source integration time, which typically had rms noise levels a factor of 1.4 better than the original map. Any maser candidate that was not seen in the follow-up spectrum was considered spurious and discarded.

After identifying masers with the above method, the spatially smoothed data cube was then spectrally binned (along the velocity axis), with three channels combined into each bin. A new peak temperature map was made from this spatially smoothed and spectrally binned map then visually inspected for other masers. This method was used because some masers show linewidths significantly greater than the channel width (0.45 km s^{-1}). Binning the data in this way allows us to pick out weak masers with linewidths of approximately 1.4 km s^{-1}. We also binned the data with eight channels per bin, but did not find any new detections over the unbinned and three-channel binned data.

We note that our method is well suited to finding weak H_2O masers that typically have large enough linewidths to appear in more than one channel. However, the method may miss some weak methanol masers, which are known to have very narrow linewidths, since the methanol maser may appear in a single channel and be flagged as a noise spike.

5.1 Positional accuracy

The reported positions of H_2O masers (see Section 6) are based on the position of the brightest emission pixel in the data cube. Whilst the Mopra beam is 2.2 arcmin at 22.2 GHz, the positions of bright masers should be more accurate than this. Some of the detected H_2O masers have been previously observed with the ATCA (Breen et al. 2010) to higher positional accuracy than our Mopra observations. We can therefore compare the positions of those masers that appear in both surveys. Fig. 5 shows the distribution of offsets for the masers we have detected with Mopra, compared to the positions given by Breen et al. (2010). We find that nearly all of our H_2O maser positions are no more than 1 arcmin offset from the corresponding ATCA position. We also find that the median offset is 20 arcsec, indicating that most of the reported positions of masers are probably no more than 20 arcsec off the real positions.

We also note that of the 34 maser sites that overlap with Breen et al. (2010), nine (i.e. 26 per cent) are identified as multiple sites by

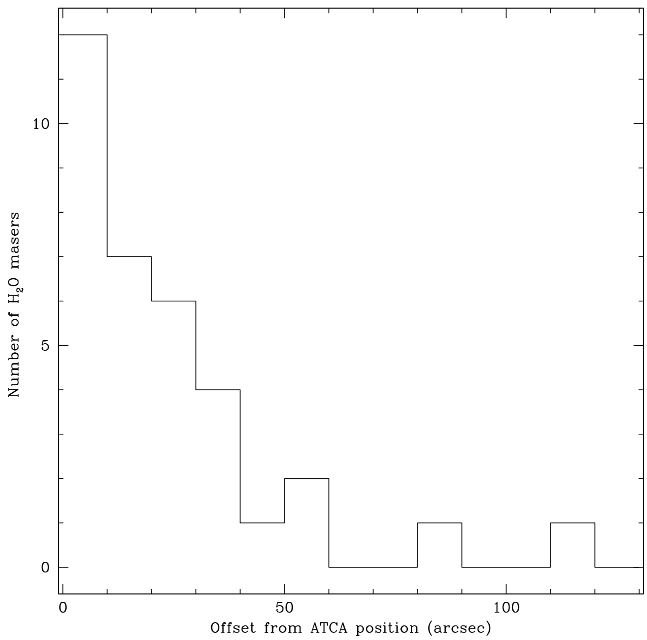

Figure 5. Distribution of Mopra H_2O maser offsets, compared to ATCA positions, using Breen et al. (2010). Note that there are two sites offset by more than 60 arcsec. These are G000.53+0.18 and G337.64+0.15. The emission features in our spectra of these sites lie close to, but not coincident with, emission features from Breen et al. (2010). Thus, it is possible that both sites detected in HOPS may be separate from those found by Breen et al. (2010).

Breen et al. (2010), but are not resolved by the Mopra beam in our observations. We expect that many more maser spectra identified in this work may consist of multiple maser sites.

6 RESULTS

Here we report the results on the H_2O maser emission detected in HOPS. Occasional detections of rare masers are reported in Section 7.3, and results from other thermal spectral lines such as NH_3, radio recombination lines and HCCCN (3–2) will be reported in later papers.

H_2O maser emission was found towards 540 distinct sites in the region observed in HOPS. The properties of these sites are summarized in Table 2. The source name (Column 1) is derived from the Galactic coordinates. Columns 2 and 3 list the coordinates of the site. The peak flux density, velocity and FWHM of the strongest maser spot in the spectrum are listed in Columns 4, 5 and 6, respectively. The minimum and maximum velocities over which emission has been detected are given in Columns 7 and 8, respectively. The last column lists whether a maser is a new detection or previously reported. Reference numbers to previously reported masers in the last column are the first detection of the maser and are given in Table 3. Spectra of the masers are presented in Fig. 6. The strongest maser (G27.18−0.08) has a peak flux density of 3933 Jy and the weakest maser (G305.56+0.01) has a peak flux density of 0.7 Jy. Note that the weakest maser was detected because it shows a broad line FWHM (5.0 km s^{-1}). The median peak flux density is 11.4 Jy. We detect 62 masers (9 per cent) with peak flux densities over 100 Jy. 334 of the detected H_2O maser sites are new detections (62 per cent). Note that since the Mopra beam for these observations is 2 arcmin, it is likely that many of the maser spectra are composed

Table 2. Properties of detected water masers. Column 1 lists the source name, derived from the Galactic coordinates. Right ascension and declination coordinates are given in Columns 2 and 3, respectively. Properties of the strongest maser spot are given in Columns 4–6: Column 4 lists the peak flux density, Column 5 lists the line centre velocity and Column 6 lists the line FWHM of the brightest maser spot. For maser sites with multiple maser spots, the minimum and maximum velocities of the maser spots are given in Columns 7 and 8, respectively. Otherwise, for maser sites with only a single maser spot, no velocity range is given. Column 9 lists whether the maser site is a new detection ('NEW') or a previous detection. Previous detections are listed as numbers which refer to Table 3. If a previous detection also identifies the maser site with an evolved star, this is also noted. If a previously known evolved star is associated with a newly discovered H_2O maser, then 'NEW' is written, as well as the reference number for the evolved star association.

Source name	RA (J2000) ($^{h\,m\,s}$)	Dec. (J2000) ($^{\circ}\,'\,''$)	Strongest maser spot Peak flux density (Jy)	Velocity (km s^{-1})	FWHM (km s^{-1})	Velocity range Min (km s^{-1})	Max	Comments[1]
G0.05−0.22	17 46 35.9	−29 00 15	7.4	12.4	0.8	11.7	14.7	1
G0.31−0.18	17 47 01.6	−28 46 00	39.2	10.6	0.8	−6.3	21.4	2
G0.31−0.21	17 47 10.3	−28 46 48	6.6	21.5	0.9	10.3	22.4	2
G0.34+0.09	17 46 04.0	−28 36 04	36.6	7.1	0.6	–	–	1
G0.37−0.17	17 47 09.7	−28 42 22	22.4	−9.1	0.9	−9.7	−5.2	1
G0.38+0.03	17 46 23.8	−28 35 50	31.8	40.0	1.6	30.3	41.5	3
G0.53+0.18	17 46 09.8	−28 23 29	6.8	−1.4	0.7	–	–	2
G0.60−0.00	17 47 03.2	−28 25 18	7.1	37.2	0.9	18.2	75.7	NEW
G0.67−0.04	17 47 20.7	−28 23 13	508.1	70.7	3.8	23.3	127.0	4
G1.01−0.24	17 48 56.4	−28 12 06	4.0	3.4	0.7	–	–	NEW
G1.05−0.07	17 48 21.8	−28 04 46	11.1	−37.1	2.8	–	–	NEW
G1.15−0.13	17 48 50.0	−28 01 18	177.5	−21.6	1.5	−25.7	−13.0	5
G1.17−0.04	17 48 31.0	−27 57 27	35.4	−22.3	1.6	–	–	NEW
G2.53−0.23	17 52 23.7	−26 53 18	4.2	1.5	0.6	–	–	NEW
G2.58−0.44	17 53 19.9	−26 56 44	72.6	−6.0	0.8	−25.5	4.8	6
G2.60−0.36	17 53 04.9	−26 53 18	9.1	−20.5	2.1	−21.9	−10.9	NEW
G2.90−0.43	17 54 01.0	−26 40 12	8.6	82.4	1.0	–	–	NEW
G2.93+0.28	17 51 22.3	−26 17 16	4.1	−42.8	0.5	–	–	NEW
G3.88+0.27	17 53 33.6	−25 28 18	4.3	10.3	0.9	–	–	NEW
G4.00+0.33	17 53 34.9	−25 20 07	3.5	13.6	0.9	–	–	NEW
G4.00−0.17	17 55 29.5	−25 35 12	2.8	−55.0	7.5	–	–	NEW
G4.83+0.22	17 55 51.2	−24 40 13	3.2	11.1	2.7	–	–	7
G4.89−0.13	17 57 19.9	−24 47 41	42.8	6.9	1.4	–	–	NEW
G5.37+0.05	17 57 41.2	−24 17 33	10.0	2.5	1.1	–	–	NEW
G5.52−0.25	17 59 09.9	−24 19 01	2.6	21.9	1.4	–	–	NEW
G5.63−0.29	17 59 34.0	−24 14 38	2.5	17.5	1.2	–	–	NEW
G5.66+0.42	17 56 57.0	−23 51 36	18.4	18.3	1.0	13.9	19.7	NEW
G5.71−0.50	18 00 31.9	−24 16 28	4.2	12.3	0.9	–	–	NEW, 8 – Mira variable
G5.88−0.39	18 00 29.8	−24 04 06	207.7	9.4	0.9	2.4	11.8	9
G5.90−0.43	18 00 41.6	−24 04 28	7.4	10.1	2.7	7.5	47.0	2
G5.91−0.39	18 00 33.1	−24 02 48	43.0	−61.5	2.2	−64.7	−52.6	2
G6.09−0.12	17 59 54.9	−23 45 34	6.8	3.0	0.7	–	–	10
G6.19−0.36	18 01 02.7	−23 47 11	5.9	−29.3	0.8	–	–	NEW
G6.20−0.01	17 59 43.4	−23 36 02	2.8	−35.1	4.9	−38.3	−30.4	NEW
G6.23−0.06	17 59 59.5	−23 36 21	4.8	16.9	0.9	–	–	NEW
G6.23+0.32	17 58 34.7	−23 24 54	11.9	18.1	1.2	2.4	87.2	NEW
G6.59−0.19	18 01 16.1	−23 21 22	4.6	−2.0	1.0	–	–	NEW
G6.61−0.08	18 00 54.7	−23 16 54	29.1	5.3	1.0	−0.7	7.5	2
G6.79−0.26	18 01 58.9	−23 12 57	7.8	11.7	0.8	5.5	13.2	2
G6.92−0.23	18 02 06.2	−23 05 21	8.8	−10.0	3.3	−14.0	−4.8	11
G7.38−0.09	18 02 34.7	−22 37 24	7.6	42.4	1.0	–	–	NEW
G7.46−0.28	18 03 27.3	−22 38 29	3.7	23.7	1.8	–	–	NEW
G7.47+0.05	18 02 14.1	−22 28 09	42.4	−16.3	1.6	−87.5	−10.3	NEW
G7.54−0.06	18 02 48.5	−22 27 38	4.4	−1.1	3.2	–	–	NEW
G8.00−0.27	18 04 34.3	−22 09 57	12.1	36.1	0.8	25.3	43.9	NEW
G8.08+0.15	18 03 11.2	−21 53 30	7.8	22.1	1.1	–	–	NEW
G8.20+0.13	18 03 29.2	−21 47 56	10.7	18.4	1.0	0.4	19.6	NEW
G8.32−0.10	18 04 38.0	−21 48 28	4.1	36.9	2.4	–	–	NEW
G8.41−0.30	18 05 33.7	−21 49 49	10.3	47.6	1.2	–	–	NEW
G8.63−0.24	18 05 48.4	−21 36 07	8.0	1.3	1.0	–	–	NEW

Table 2 – *continued*

Source name	RA (J2000) (h m s)	Dec. (J2000) (° ′ ″)	Strongest maser spot Peak flux density (Jy)	Velocity (km s^{-1})	FWHM (km s^{-1})	Velocity range Min (km s^{-1})	Max	Comments[1]
G8.67−0.36	18 06 19.7	−21 37 30	29.8	24.7	0.7	−5.5	44.8	12
G8.70−0.43	18 06 38.5	−21 37 57	4.9	32.8	1.3	–	–	NEW
G8.73−0.39	18 06 34.2	−21 35 40	6.0	46.7	0.7	30.4	47.4	NEW
G8.83−0.03	18 05 25.7	−21 19 24	38.9	−9.5	1.7	−13.3	−7.2	7
G8.93−0.02	18 05 35.6	−21 13 44	88.9	7.0	0.9	5.7	49.2	13 – M supergiant
G9.10−0.40	18 07 22.8	−21 16 14	18.3	62.9	1.2	−62.0	289.3	14 – Water fountain
G9.62+0.19	18 06 15.0	−20 31 43	60.2	5.6	1.7	−9.8	9.1	15
G9.95+0.46	18 05 57.2	−20 06 38	2.9	−65.8	1.1	−66.5	−61.9	NEW
G9.98−0.03	18 07 51.0	−20 19 15	13.4	45.2	1.7	43.7	59.6	7
G10.34−0.14	18 08 59.0	−20 03 58	19.9	19.2	1.1	5.8	35.7	16
G10.39−0.01	18 08 35.3	−19 57 26	7.2	45.9	1.2	–	–	NEW
G10.44−0.01	18 08 42.5	−19 54 24	19.7	70.4	1.8	67.8	83.8	2
G10.48+0.03	18 08 37.4	−19 51 28	108.3	70.7	1.1	40.7	88.1	17
G10.62−0.38	18 10 26.1	−19 55 52	381.5	0.3	3.1	−19.4	8.8	18
G10.64−0.50	18 10 56.1	−19 58 35	59.7	−67.9	3.9	−71.8	−46.1	NEW
G10.89+0.13	18 09 07.4	−19 27 20	13.8	23.9	2.2	9.0	26.0	NEW
G10.96+0.03	18 09 38.9	−19 26 18	25.7	24.3	0.5	–	–	19
G11.65−0.06	18 11 22.2	−18 52 28	1.4	3.7	6.1	−3.1	30.8	NEW
G11.73−0.18	18 11 57.2	−18 51 53	5.9	−43.0	0.9	–	–	NEW
G11.87+0.00	18 11 35.6	−18 39 21	21.6	21.2	0.9	20.2	38.9	NEW
G11.92−0.14	18 12 13.2	−18 40 49	7.1	33.8	0.8	23.8	49.6	12
G11.96−0.16	18 12 22.0	−18 39 09	6.2	40.3	1.4	38.5	45.2	NEW
G12.22−0.09	18 12 38.5	−18 23 39	3.2	20.8	4.6	–	–	4
G12.22+0.38	18 10 53.2	−18 09 56	20.9	37.7	0.9	–	–	NEW
G12.22−0.33	18 13 31.4	−18 29 57	21.5	−15.8	1.3	–	–	NEW
G12.55−0.18	18 13 39.2	−18 08 45	9.4	59.5	0.8	–	–	NEW
G12.68−0.18	18 13 53.5	−18 01 31	163.4	58.6	0.8	53.7	61.9	20
G12.82−0.19	18 14 13.3	−17 54 55	2.8	36.1	1.2	30.5	37.4	4
G12.91−0.02	18 13 45.5	−17 45 06	19.4	13.6	2.3	–	–	4
G12.92−0.24	18 14 36.4	−17 51 05	5.5	35.6	1.6	28.9	36.3	4
G12.94−0.04	18 13 55.1	−17 44 02	6.1	20.9	0.7	–	–	NEW
G12.94−0.07	18 14 00.7	−17 44 45	57.0	33.5	0.7	–	–	NEW
G13.19+0.06	18 14 03.2	−17 27 56	9.1	−4.1	3.5	–	–	4
G13.44+0.24	18 13 52.9	−17 09 31	9.0	48.2	0.9	40.7	55.4	NEW
G13.46+0.22	18 14 00.4	−17 09 23	7.1	16.4	1.1	–	–	NEW
G13.69−0.05	18 15 26.9	−17 04 39	31.9	44.7	0.9	–	–	NEW
G13.82+0.27	18 14 32.0	−16 48 58	2.9	70.9	1.3	–	–	NEW
G13.88+0.29	18 14 34.8	−16 44 50	20.0	−41.7	1.4	−45.6	−14.0	4
G14.03−0.31	18 17 04.6	−16 54 01	5.9	129	1.0	–	–	NEW
G14.11+0.09	18 15 45.3	−16 38 38	47.9	9.2	0.8	–	–	21
G14.17−0.05	18 16 23.6	−16 39 35	126.5	54.3	1.3	35.1	57.9	8
G14.20−0.18	18 16 56.9	−16 41 38	27.5	24.1	1.3	–	–	NEW
G14.61+0.03	18 16 59.6	−16 14 10	21.9	29.8	0.9	7.6	32.0	21
G14.68−0.05	18 17 24.2	−16 12 47	13.0	−5.2	0.8	−6.7	−0.9	NEW
G14.78−0.36	18 18 43.9	−16 16 16	4.9	31.6	1.3	30.0	34.0	NEW
G15.09+0.21	18 17 16.5	−15 43 22	21.4	28.0	0.9	20.7	32.1	22
G15.54−0.13	18 19 22.3	−15 29 28	4.3	23.1	0.6	–	–	NEW
G15.55+0.37	18 17 36.7	−15 14 38	2.0	70.1	2.9	–	–	NEW
G15.97+0.24	18 18 53.2	−14 56 09	49.5	58.3	0.6	−98.1	190.5	NEW
G16.05−0.13	18 20 24.7	−15 02 24	13.7	62.2	0.6	–	–	NEW
G16.25+0.19	18 19 37.0	−14 42 38	3.7	−1.3	1.7	–	–	NEW
G16.28+0.42	18 18 50.7	−14 34 55	1.0	−84.7	3.8	–	–	NEW
G16.46+0.44	18 19 06.7	−14 24 32	18.2	21.2	1.5	18.0	46.7	NEW
G16.58−0.04	18 21 07.1	−14 31 38	63.2	63.9	1.3	56.5	69.5	12
G17.55−0.12	18 23 15.8	−13 42 35	477.2	30.6	1.1	28.7	57.2	13
G17.64+0.17	18 22 24.5	−13 29 42	126.7	26.0	1.0	15.7	27.3	23
G17.97+0.09	18 23 18.5	−13 14 36	8.3	26.6	0.8	–	–	NEW
G17.98+0.24	18 22 47.8	−13 09 27	15.0	15.4	0.9	–	–	22
G18.16+0.39	18 22 36.8	−12 56 14	10.4	55.6	0.9	–	–	NEW
G18.24−0.12	18 24 35.2	−13 05 53	8.4	39.1	1.8	–	–	NEW
G18.52+0.15	18 24 09.9	−12 43 25	3.0	22.4	3.0	–	–	NEW

Table 2 – *continued*

Source name	RA (J2000) (h m s)	Dec. (J2000) (° ′ ″)	Strongest maser spot Peak flux density (Jy)	Velocity (km s^{-1})	FWHM (km s^{-1})	Velocity range Min (km s^{-1})	Max	Comments[1]
G18.55+0.04	18 24 38.0	−12 45 21	10.7	32.2	0.5	31.3	35.2	NEW
G18.61−0.08	18 25 10.3	−12 45 30	6.0	41.3	1.2	40.0	52.4	NEW
G18.73−0.22	18 25 55.3	−12 42 49	28.5	36.7	1.3	32.2	46.3	NEW
G18.88−0.47	18 27 07.0	−12 41 55	7.7	65.1	1.5	–	–	NEW
G19.00−0.23	18 26 27.8	−12 28 57	21.8	−15.9	7.2	–	–	NEW
G19.15−0.47	18 27 36.4	−12 27 23	41.0	30.2	0.7	22.1	37.3	NEW, 24 – M supergiant
G19.27+0.09	18 25 48.3	−12 05 25	3.4	28.6	1.9	–	–	NEW
G19.47+0.18	18 25 53.3	−11 52 26	5.0	−6.7	2.3	−12.6	20.7	NEW
G19.49+0.16	18 25 58.7	−11 52 14	4.5	27.0	1.1	22.4	28.3	NEW
G19.61−0.23	18 27 37.9	−11 56 32	127.4	41.9	3.4	23.0	57.9	25
G19.71−0.26	18 27 54.7	−11 51 55	6.4	38.9	1.0	38.1	44.1	NEW
G20.08−0.13	18 28 10.3	−11 28 39	19.7	46.4	0.8	37.5	47.4	12
G20.78−0.06	18 29 12.7	−10 49 47	37.8	59.2	1.8	–	–	26
G21.04−0.06	18 29 42.9	−10 35 36	5.4	35.6	1.5	–	–	27
G21.80−0.12	18 31 21.3	−09 56 56	83.2	106.2	2.1	−53.1	164.7	28 – Water fountain
G21.81+0.15	18 30 24.6	−09 49 02	7.3	2.7	4.3	−4.7	10.9	NEW, 29 – Carbon star
G21.88+0.02	18 31 01.8	−09 48 44	17.3	21.4	3.2	18.9	26.2	15
G21.95+0.01	18 31 11.3	−09 45 25	14.6	109.8	0.8	95.6	111.5	23
G22.00+0.07	18 31 03.0	−09 41 10	10.0	147.2	2.3	145.4	152.1	NEW, 30 – OH/IR star
G22.03+0.22	18 30 34.3	−09 35 39	12.7	53.7	0.7	–	–	31
G22.82−0.17	18 33 26.8	−09 04 10	7.9	41.0	1.2	–	–	NEW
G22.97−0.37	18 34 27.1	−09 01 54	3.3	74.8	2.0	–	–	NEW
G23.00−0.41	18 34 38.7	−09 01 05	167.8	68.9	1.3	62.3	82.6	31
G23.15−0.23	18 34 16.8	−08 48 09	19.8	110.2	0.9	108.8	113.3	NEW
G23.21−0.38	18 34 55.7	−08 49 12	13.8	79.4	1.2	77.1	143.5	31
G23.41−0.21	18 34 42.3	−08 33 58	5.0	102.5	1.5	100.8	135.8	32
G23.46−0.35	18 35 18.2	−08 35 12	4.1	105.6	2.3	–	–	NEW
G23.48+0.10	18 33 44.1	−08 21 26	10.5	87.0	2.5	49.2	89.5	NEW
G23.91+0.08	18 34 35.2	−07 59 16	3.7	73.1	4.2	71.3	97.9	19
G23.98+0.15	18 34 26.6	−07 53 38	13.8	31.5	1.6	–	–	33
G23.98+0.24	18 34 08.1	−07 50 43	11.3	99.8	1.2	94.5	107.6	NEW
G24.33+0.14	18 35 08.3	−07 35 16	16.3	110.9	1.4	–	–	31
G24.43+0.09	18 35 30.2	−07 31 19	3.7	111.9	1.4	–	–	NEW
G24.45+0.26	18 34 57.3	−07 25 24	10.7	113.9	0.5	–	–	NEW
G24.46+0.20	18 35 10.7	−07 26 35	34.0	120.7	1.9	115.7	122.6	NEW
G24.50−0.03	18 36 05.3	−07 30 50	20.1	111.3	0.8	73.7	153.0	13
G24.79+0.08	18 36 12.9	−07 12 04	226.7	111.2	2.4	89.5	116.4	18
G24.94−0.03	18 36 54.5	−07 07 17	10.5	−4.9	1.3	–	–	NEW
G24.94+0.08	18 36 31.3	−07 04 18	280.0	42.9	0.6	–	–	31
G24.99−0.17	18 37 29.7	−07 08 25	7.5	96.4	1.1	–	–	NEW
G25.06+0.27	18 36 02.3	−06 52 44	9.1	77.6	2.2	–	–	NEW, 34 – OH/IR star
G25.11−0.03	18 37 13.1	−06 58 27	7.5	101.2	2.2	93.8	109.1	NEW
G25.29−0.04	18 37 35.3	−06 48 52	4.6	114.7	1.4	105.7	119.3	NEW
G25.38−0.18	18 38 15.9	−06 47 56	111.8	68.6	1.0	–	–	35
G25.40+0.03	18 37 31.2	−06 41 03	26.1	−15.9	0.7	–	–	22
G25.52−0.11	18 38 14.6	−06 38 43	9.1	98.8	0.7	–	–	NEW
G25.73−0.11	18 38 37.7	−06 27 38	13.0	97.4	1.3	96.5	105.9	NEW
G25.82−0.05	18 38 35.2	−06 21 06	20.6	125.7	0.7	82.3	127.4	NEW
G25.83−0.18	18 39 02.9	−06 24 07	295.0	90.6	2.6	82.8	97.3	31
G25.91−0.08	18 38 50.7	−06 16 56	14.1	108.6	0.7	102.9	126.2	NEW
G25.98−0.08	18 39 00.0	−06 13 05	11.6	90.0	1.5	–	–	NEW
G26.11−0.09	18 39 16.7	−06 06 38	64.2	23.5	1.4	22.1	27.4	22
G26.13−0.03	18 39 06.1	−06 04 08	11.1	84.9	3.0	72.7	101.3	NEW
G26.40−0.10	18 39 50.7	−05 51 17	5.8	98.6	2.8	78.0	101.9	NEW
G26.51+0.28	18 38 40.7	−05 34 53	52.4	103.3	3.6	101.0	108.3	7
G26.53+0.40	18 38 17.4	−05 30 49	11.3	100.9	0.9	–	–	NEW
G26.55−0.29	18 40 47.6	−05 48 56	11.5	111.6	3.5	105.0	117.1	NEW
G26.85+0.16	18 39 44.3	−05 20 34	3.3	97.0	1.2	83.0	111.6	NEW
G27.01−0.03	18 40 42.6	−05 17 02	6.3	−15.2	0.9	−19.1	−14.0	NEW
G27.08+0.20	18 40 01.6	−05 06 43	1.0	27.8	13.3	–	–	NEW
G27.18−0.08	18 41 11.6	−05 08 53	3932.7	17.5	0.9	13.2	33.6	36

Table 2 – *continued*

Source name	RA (J2000) (h m s)	Dec. (J2000) (° ′ ″)	Strongest maser spot Peak flux density (Jy)	Velocity (km s^{-1})	FWHM (km s^{-1})	Velocity range Min (km s^{-1})	Max	Comments[1]
G27.33+0.18	18 40 33.7	−04 54 30	20.0	33.9	0.9	33.1	38.4	NEW, 29 – Carbon star
G27.37−0.16	18 41 49.6	−05 01 24	25.6	88.2	2.2	86.1	98.9	31
G27.41−0.05	18 41 31.1	−04 56 12	5.0	108.7	2.0	100.9	109.9	NEW
G27.50−0.28	18 42 31.1	−04 57 44	2.9	−15.4	1.3	−39.6	−11.2	NEW
G27.60+0.08	18 41 23.7	−04 42 21	4.1	35.4	0.9	23.4	41.6	NEW
G27.70+0.20	18 41 09.7	−04 33 48	2.4	62.1	5.3	–	–	NEW
G27.78+0.06	18 41 49.3	−04 33 14	8.3	98.4	1.2	92.4	109.6	31
G27.87−0.23	18 43 00.8	−04 36 47	21.0	12.3	0.7	–	–	19
G27.93+0.24	18 41 25.5	−04 20 39	58.1	62.4	1.3	35.4	65.9	37
G28.01−0.43	18 43 57.2	−04 34 38	18.0	19.3	0.6	–	–	NEW
G28.21−0.05	18 42 58.9	−04 13 40	23.7	95.4	1.1	–	–	NEW
G28.34+0.14	18 42 32.4	−04 01 18	41.3	17.5	2.0	–	–	NEW
G28.40+0.08	18 42 51.4	−03 59 50	201.1	77.7	0.7	76.9	86.1	31
G28.41+0.07	18 42 55.8	−03 59 47	26.6	34.5	0.9	21.4	40.3	31
G28.62+0.06	18 43 21.5	−03 48 31	37.7	−3.9	0.7	–	–	NEW
G28.65+0.03	18 43 29.6	−03 47 52	8.7	103.8	0.8	–	–	NEW
G28.79+0.24	18 43 00.5	−03 34 33	3.0	108.6	5.1	–	–	35
G28.81+0.37	18 42 36.5	−03 29 47	18.6	88.3	0.8	83.5	89.3	31
G28.85+0.50	18 42 12.6	−03 24 37	6.3	86.6	4.2	84.2	91.3	31
G28.86+0.07	18 43 46.2	−03 35 21	194.5	105.8	3.0	102.3	107.8	15
G28.88−0.03	18 44 07.9	−03 36 55	5.7	114.9	1.7	101.8	123.8	19
G28.96+0.40	18 42 46.0	−03 20 53	6.2	18.6	2.2	–	–	NEW
G29.25−0.24	18 45 34.8	−03 23 10	5.9	106.0	1.8	98.1	120.9	NEW
G29.28−0.13	18 45 13.6	−03 18 13	6.5	40.8	0.7	39.5	52.4	NEW
G29.33−0.16	18 45 25.3	−03 16 53	39.6	47.6	0.9	–	–	NEW
G29.49+0.19	18 44 29.1	−02 58 45	4.9	35.4	2.1	31.5	37.9	NEW
G29.92−0.04	18 46 05.1	−02 42 08	36.3	40.5	2.1	15.5	42.5	32
G29.96−0.01	18 46 02.6	−02 38 59	73.5	99.2	2.1	88.5	110.3	4
G29.98+0.12	18 45 38.7	−02 34 13	7.8	102.8	1.1	101.7	122.7	NEW
G291.37−0.21	11 14 08.3	−60 52 34	79.0	3.0	0.5	–	–	NEW
G291.58−0.42	11 15 05.2	−61 09 11	343.4	0.7	0.9	−8.5	19.3	38
G291.79+0.39	11 19 07.9	−60 28 04	7.3	−152.5	0.6	–	–	NEW
G292.58−0.29	11 23 17.2	−61 22 18	12.4	−14.0	3.1	–	–	NEW
G293.59−0.20	11 31 35.6	−61 36 55	17.2	29.4	0.7	–	–	NEW
G295.09−0.46	11 43 12.9	−62 17 09	11.1	25.1	1.3	23.9	27.0	NEW
G297.86−0.27	12 07 00.2	−62 41 59	13.1	−19.7	2.0	−20.9	2.5	NEW
G298.20−0.34	12 09 48.4	−62 49 47	3.6	81.0	1.5	–	–	NEW
G298.22−0.33	12 09 57.4	−62 49 28	3.2	36.7	1.2	33.1	38.7	39
G298.23−0.38	12 09 57.9	−62 52 31	13.4	40.4	1.1	29.6	41.3	NEW
G298.63−0.36	12 13 32.2	−62 54 47	30.4	40.0	1.5	39.2	44.3	NEW
G298.72−0.08	12 14 36.2	−62 39 11	34.7	18.1	1.3	–	–	NEW
G298.88+0.32	12 16 30.9	−62 16 48	26.7	18.4	2.1	9.5	21.1	NEW
G299.00+0.13	12 17 17.6	−62 29 09	115.2	19.3	0.8	−12.3	29.8	39
G300.32−0.27	12 28 24.3	−63 01 12	54.0	33.7	0.8	–	–	NEW
G300.50−0.17	12 30 01.1	−62 56 41	241.4	11.0	1.1	−9.0	12.6	38
G301.13−0.22	12 35 32.9	−63 02 21	834.1	−45.8	0.8	−66.8	−28.4	38
G301.35+0.02	12 37 32.9	−62 48 40	4.9	−26.8	0.8	–	–	NEW
G301.76+0.29	12 41 13.2	−62 33 23	15.6	−43.7	1.0	−61.5	−19.4	NEW
G302.48−0.03	12 47 28.7	−62 54 09	25.0	−30.9	0.7	−61.4	6.9	NEW
G303.70−0.41	12 58 18.3	−63 16 14	17.1	−54.6	1.0	−62.0	−40.2	NEW
G303.87+0.47	12 59 33.7	−62 23 31	3.5	−63.8	1.3	–	–	NEW
G304.06+0.44	13 01 09.5	−62 24 56	10.7	−51.1	1.5	−52.8	−41.4	NEW
G304.07+0.41	13 01 18.3	−62 26 24	18.4	−50.5	0.9	–	–	NEW
G304.37−0.34	13 04 09.3	−63 10 31	16.6	29.0	0.8	–	–	NEW
G305.01+0.43	13 09 21.7	−62 22 28	12.1	−54.5	1.0	–	–	NEW
G305.14+0.07	13 10 41.9	−62 43 02	4.2	−38.4	0.8	–	–	40
G305.19−0.00	13 11 13.7	−62 47 20	25.8	33.4	1.7	−47.5	36.6	38
G305.21+0.21	13 11 11.9	−62 34 36	180.0	−39.1	0.8	−47.8	−29.7	41
G305.27−0.00	13 11 52.3	−62 46 52	2.4	−37.9	1.5	−39.1	−32.5	40
G305.32+0.07	13 12 16.8	−62 42 08	903.4	−45.1	0.7	−45.7	−29.0	40

Table 2 – *continued*

Source name	RA (J2000) (h m s)	Dec. (J2000) (° ′ ″)	Strongest maser spot Peak flux density (Jy)	Velocity (km s^{-1})	FWHM (km s^{-1})	Velocity range Min (km s^{-1})	Max	Comments[1]
G305.36+0.15	13 12 34.3	−62 37 13	457.6	−35.6	3.0	−46.3	−29.7	42
G305.36+0.21	13 12 33.8	−62 33 33	170.9	−33.6	1.2	−90.5	52.7	43
G305.56+0.01	13 14 24.4	−62 44 48	0.7	−37.7	5.0	–	–	40
G305.66−0.10	13 15 24.1	−62 50 52	6.7	−68.9	1.8	–	–	44
G305.73+0.08	13 15 49.4	−62 39 19	4.1	−43.9	3.8	–	–	40
G305.80−0.24	13 16 40.8	−62 58 24	3023.5	−27.6	0.5	−43.2	−24.3	38
G305.82−0.12	13 16 44.8	−62 50 42	4.0	−27.5	0.6	−55.9	−15.6	44
G305.83−0.08	13 16 51.4	−62 48 31	41.2	−114.5	4.3	−120.1	−83.8	44
G305.89+0.02	13 17 14.4	−62 42 21	41.2	−28.3	1.4	−40.4	−26.5	44
G305.95+0.03	13 17 46.8	−62 41 26	3.7	−41.5	1.0	–	–	44,45 – AGB star
G307.13+0.32	13 27 38.3	−62 15 30	87.2	−42.8	0.8	–	–	NEW
G307.27+0.08	13 29 05.3	−62 28 17	3.9	−31.0	1.7	–	–	NEW
G307.34+0.18	13 29 36.4	−62 21 52	2.8	−93.8	5.3	–	–	NEW
G307.80−0.45	13 34 24.6	−62 55 08	47.4	−13.0	1.0	–	–	NEW
G307.95+0.03	13 35 00.0	−62 25 18	3.3	−45.0	5.4	–	–	NEW
G308.05−0.38	13 36 27.8	−62 48 24	8.0	−12.3	0.7	−17.5	−5.8	NEW
G308.08−0.42	13 36 43.7	−62 50 01	5.1	−16.3	1.2	−17.7	−8.1	NEW
G308.13−0.30	13 37 01.1	−62 42 21	36.1	0.6	0.7	–	–	NEW
G308.16−0.45	13 37 29.9	−62 51 13	4.4	5.2	3.1	–	–	NEW
G308.61−0.18	13 40 55.9	−62 30 25	2.9	−12.6	3.5	–	–	NEW
G308.70−0.00	13 41 23.3	−62 18 48	2.1	−66.3	1.3	–	–	NEW
G308.92+0.12	13 43 03.4	−62 09 08	3.7	−50.5	1.0	–	–	39
G309.29−0.47	13 47 11.3	−62 38 49	5.2	−5.8	2.4	–	–	NEW
G309.38−0.13	13 47 20.8	−62 18 07	8.5	−50.6	0.8	–	–	38
G309.90+0.33	13 50 48.5	−61 43 59	6.9	−54.3	0.8	−55.1	−47.0	NEW
G310.34−0.07	13 55 15.2	−62 00 58	6.0	−3.5	3.4	–	–	NEW
G310.52−0.22	13 57 03.4	−62 07 12	4.5	55.3	2.3	47.1	58.8	NEW
G310.58+0.38	13 56 19.0	−61 31 45	5.7	−30.8	0.9	−57.4	−28.1	37
G310.88+0.01	13 59 28.4	−61 48 33	15.4	−70.8	1.8	−82.0	−44.2	NEW
G311.23−0.03	14 02 29.7	−61 45 15	162.2	28.0	1.1	16.1	43.4	44
G311.56+0.23	14 04 30.2	−61 24 29	13.3	9.6	2.0	−1.1	12.6	NEW
G311.64−0.38	14 06 38.9	−61 58 35	215.5	32.2	2.2	14.6	52.9	38
G311.72+0.24	14 05 45.1	−61 21 21	108.1	−72.7	1.0	−80.3	−44.5	NEW
G312.07+0.09	14 08 54.7	−61 23 53	15.0	−32.8	1.7	−38.1	5.6	44
G312.11+0.01	14 09 27.1	−61 27 54	11.4	−41.8	1.6	−46.5	−27.6	44
G312.48−0.33	14 13 15.4	−61 40 46	11.7	−31.6	3.4	−43.3	−27.3	NEW
G313.46+0.07	14 19 55.3	−60 58 43	11.5	1.3	1.0	–	–	NEW
G313.47+0.20	14 19 38.8	−60 51 28	14.0	−9.7	0.7	−12.2	1.4	38
G313.57+0.32	14 20 04.5	−60 42 23	12.1	−45.2	0.8	−49.0	−39.8	2
G314.23+0.26	14 25 17.8	−60 32 29	6.4	−61.4	1.2	–	–	NEW
G314.33+0.11	14 26 29.6	−60 38 45	9.8	−41.8	1.2	–	–	2
G314.41+0.05	14 27 17.8	−60 40 12	152.5	−43.8	0.5	–	–	NEW
G314.98+0.03	14 31 38.3	−60 28 36	6.3	−54.1	2.2	–	–	NEW
G315.22−0.25	14 34 20.2	−60 38 45	6.4	−64.5	2.0	–	–	NEW
G315.23−0.11	14 33 57.3	−60 30 45	5.8	−16.2	5.6	–	–	NEW
G315.93+0.05	14 38 42.8	−60 05 15	13.6	−7.1	1.1	–	–	NEW
G316.09−0.07	14 40 14.5	−60 07 41	6.7	−53.0	0.9	–	–	NEW
G316.35−0.37	14 43 07.8	−60 17 43	6.8	1.5	2.4	−14.6	5.7	36
G316.40−0.32	14 43 19.7	−60 13 44	8.3	−11.5	1.5	−18.1	3.2	38
G316.63−0.09	14 44 16.6	−59 55 35	13.6	−21.1	2.9	−24.5	−5.6	9
G316.76−0.02	14 44 55.6	−59 48 21	39.9	−34.9	1.6	−53.2	−32.8	9
G316.81−0.06	14 45 25.5	−59 49 18	311.0	−47.2	1.6	−52.3	−25.7	41
G317.87+0.14	14 52 14.5	−59 10 49	5.1	−3.3	1.0	−4.2	0.7	NEW
G317.87−0.15	14 53 16.2	−59 26 28	18.0	−52.7	1.2	−54.4	−41.4	NEW
G317.98+0.12	14 53 08.7	−59 09 00	4.3	−59.1	0.9	−60.3	−44.5	NEW
G318.05+0.09	14 53 41.7	−59 08 36	805.3	−52.0	3.0	−61.0	−38.3	46
G318.78−0.13	14 59 30.6	−59 00 28	731.0	−135.7	2.7	−144.9	−39.1	NEW
G318.94−0.18	15 00 50.1	−58 58 21	3.7	−33.8	1.4	−38.5	−32.7	38
G319.34−0.32	15 04 04.7	−58 54 13	7.2	−36.0	1.4	−40.7	−34.9	NEW
G319.39−0.01	15 03 13.6	−58 36 13	11.0	−6.4	0.5	−8.9	−0.8	2

Table 2 – *continued*

Source name	RA (J2000) (h m s)	Dec. (J2000) (° ′ ″)	Strongest maser spot Peak flux density (Jy)	Velocity (km s^{-1})	FWHM (km s^{-1})	Velocity range Min (km s^{-1})	Max	Comments[1]
G319.83−0.19	15 06 52.2	−58 32 47	16.0	−12.1	2.9	−15.6	−0.5	38
G320.23−0.28	15 09 52.8	−58 25 31	5.7	−61.7	1.3	−67.5	−58.9	38
G320.24−0.08	15 09 09.8	−58 14 55	3.7	−9.9	1.1	–	–	NEW
G320.26−0.30	15 10 06.6	−58 25 38	7.0	−116.3	2.5	−127.9	−108.4	38
G320.34−0.20	15 10 16.2	−58 17 57	23.8	−107.7	1.3	−118.3	−102.3	NEW
G320.43+0.10	15 09 40.1	−57 59 52	12.3	−10.4	1.0	−16.6	−3.1	NEW
G320.90−0.29	15 14 15.9	−58 05 25	172.0	−35.9	1.6	−39.9	−33.2	47
G321.04−0.50	15 15 58.6	−58 11 41	12.0	−52.4	1.0	−67.3	−51.3	2
G321.38−0.29	15 17 22.5	−57 50 20	3.2	−53.9	0.7	−60.0	47.7	NEW
G321.93−0.00	15 19 41.1	−57 17 55	16.3	−38.6	2.2	−41.3	−34.5	NEW
G323.74−0.26	15 31 45.0	−56 30 33	11.3	−49.6	1.7	−52.7	−47.8	38
G324.18+0.41	15 31 36.1	−55 42 35	11.7	−56.6	1.1	–	–	NEW
G324.20+0.13	15 32 51.8	−55 55 57	82.9	−76.7	1.5	−91.8	−65.4	9
G325.63+0.29	15 40 20.8	−54 57 17	21.9	14.8	0.9	–	–	NEW
G326.06−0.14	15 44 32.5	−55 02 41	6.8	−75.0	2.6	−81.1	−70.4	NEW
G326.45+0.33	15 44 41.1	−54 25 45	6.2	−71.6	0.6	–	–	NEW
G326.48−0.37	15 47 48.0	−54 57 57	4.9	−51.6	1.0	–	–	NEW
G326.48+0.38	15 44 38.6	−54 22 50	67.9	−82.4	0.9	−85.7	−81.3	NEW, 48 – AGB star
G326.56+0.07	15 46 24.0	−54 34 21	10.3	1.9	1.0	–	–	NEW
G326.78−0.23	15 48 53.9	−54 40 11	93.9	−66.7	0.8	−70.9	−63.0	2
G327.40+0.45	15 49 17.7	−53 45 06	135.0	−80.2	1.0	−85.0	−75.8	9
G327.41−0.07	15 51 32.1	−54 08 56	9.3	−70.8	2.0	−95.5	−65.9	NEW, 30 – OH/IR star
G327.59−0.38	15 53 50.8	−54 16 18	24.3	−71.7	1.9	–	–	NEW
G327.65−0.38	15 54 09.2	−54 14 05	9.7	−73.1	2.2	–	–	NEW
G328.26−0.41	15 57 28.3	−53 52 10	11.9	−39.7	1.1	–	–	NEW
G328.31+0.43	15 54 06.1	−53 11 31	138.3	−94.7	1.1	–	–	9
G328.94−0.12	15 59 42.0	−53 12 18	5.5	−41.3	3.2	–	–	NEW
G328.99−0.43	16 01 20.5	−53 24 39	80.4	−84.9	1.5	−91.6	−82.1	NEW
G329.04−0.20	16 00 34.4	−53 12 07	4.2	−51.1	2.0	−55.9	−34.7	46
G329.09+0.42	15 58 09.5	−52 42 03	2.7	−55.0	3.5	–	–	NEW
G329.18−0.31	16 01 45.7	−53 11 26	171.1	−49.6	1.5	−128.4	−33.6	9
G329.21+0.44	15 58 38.4	−52 36 22	11.0	−106.1	2.1	−116.3	−102.3	NEW
G329.41+0.05	16 01 19.7	−52 46 22	28.2	−87.8	0.8	–	–	NEW, 29 – Carbon star
G329.41−0.45	16 03 30.9	−53 08 56	72.6	−75.6	1.3	−77.0	−68.3	9
G329.43−0.16	16 02 21.5	−52 54 47	12.4	−73.3	0.7	−103.9	−71.3	2
G329.53+0.09	16 01 43.4	−52 39 54	13.0	−91.7	0.8	–	–	NEW
G329.57−0.50	16 04 32.4	−53 04 36	4.2	−64.9	3.2	−67.8	−57.5	NEW
G329.63+0.14	16 02 00.2	−52 33 41	13.5	−89.5	1.7	−106.3	−87.2	2
G330.14−0.38	16 06 49.5	−52 36 38	5.8	−0.4	2.8	–	–	NEW
G330.29−0.39	16 07 37.2	−52 30 53	92.9	−78.8	1.0	−154.0	57.0	NEW
G330.47+0.03	16 06 35.9	−52 05 13	6.7	−58.0	0.8	−68.9	−40.5	NEW
G330.72+0.17	16 07 11.6	−51 48 46	50.3	70.3	0.5	–	–	NEW
G330.78+0.40	16 06 32.2	−51 36 11	3.0	−71.5	0.6	−81.4	−35.5	NEW
G330.85−0.43	16 10 27.5	−52 10 03	2.2	−33.6	1.2	−34.3	−26.2	NEW
G330.88−0.36	16 10 19.4	−52 05 59	90.6	−23.2	1.1	−109.9	−21.0	25
G330.95−0.18	16 09 51.9	−51 54 51	563.8	−91.5	2.8	−202.1	−66.5	42
G331.13−0.24	16 10 58.8	−51 50 12	165.4	−96.4	2.8	−115.0	−73.3	9
G331.14+0.16	16 09 14.9	−51 32 24	26.4	−76.0	1.8	−84.9	−73.9	NEW
G331.28−0.19	16 11 25.4	−51 41 51	120.3	−94.6	1.7	−104.8	−79.5	39
G331.44−0.18	16 12 11.3	−51 35 03	82.7	−88.5	1.5	−101.2	−83.6	2
G331.51−0.10	16 12 08.3	−51 28 30	927.3	−89.5	5.0	−164.5	−24.3	42
G331.55−0.12	16 12 25.6	−51 27 32	30.9	−101.5	1.2	−106.5	−84.0	9
G331.67+0.12	16 11 55.9	−51 12 39	7.5	−74.4	0.8	−76.4	−71.1	NEW
G331.75−0.32	16 14 16.1	−51 28 17	11.2	−34.1	4.8	−41.8	−18.5	NEW
G331.86+0.06	16 13 03.9	−51 07 10	7.9	−84.2	0.7	–	–	NEW
G331.97−0.24	16 14 53.5	−51 15 41	39.0	−86.3	1.0	–	–	NEW
G332.00−0.05	16 14 12.7	−51 06 22	3.2	−101.5	1.1	−102.4	−88.2	NEW
G332.09−0.42	16 16 15.1	−51 18 15	8.8	−59.4	0.6	−63.6	−52.4	2
G332.29−0.09	16 15 44.1	−50 55 52	69.5	−47.5	1.1	−52.6	−41.3	2
G332.33+0.18	16 14 41.2	−50 42 37	4.3	−47.6	0.6	–	–	NEW
G332.39−0.09	16 16 11.8	−50 51 56	4.2	−111.0	0.6	–	–	NEW

Table 2 – *continued*

Source name	RA (J2000) (h m s)	Dec. (J2000) (° ′ ″)	Strongest maser spot Peak flux density (Jy)	Velocity (km s^{-1})	FWHM (km s^{-1})	Velocity range Min (km s^{-1})	Max (km s^{-1})	Comments[1]
G332.61−0.15	16 17 24.7	−50 45 18	4.7	−26.7	0.9	−29.8	−24.1	2
G333.00−0.43	16 20 24.9	−50 40 37	11.7	−110.4	2.0	−147.0	−93.8	40
G333.03−0.45	16 20 37.2	−50 40 27	5.0	−60.1	1.8	−61.6	−51.0	40
G333.06−0.48	16 20 55.9	−50 40 38	4.4	1.3	0.8	−10.9	2.8	47
G333.06−0.10	16 19 15.1	−50 24 20	8.8	−37.5	1.3	−49.4	−32.2	NEW
G333.12−0.43	16 20 59.3	−50 35 48	114.0	−56.4	1.5	−123.6	−43.9	42
G333.23−0.06	16 19 49.8	−50 15 10	516.9	−87.3	2.8	−94.0	−83.0	41
G333.31+0.11	16 19 28.1	−50 04 37	25.0	−45.3	1.7	−50.1	−42.0	2
G333.37−0.20	16 21 04.9	−50 15 26	4.6	−58.5	0.7	−63.2	−57.1	NEW
G333.46−0.16	16 21 18.3	−50 09 40	5.0	−42.8	1.8	−45.9	−41.1	2
G333.61−0.21	16 22 10.4	−50 05 54	268.7	−51.5	1.2	−53.3	−14.7	42
G333.63−0.36	16 22 56.9	−50 11 01	4.7	−71.1	1.3	–	–	NEW
G334.21+0.09	16 23 28.0	−49 27 15	17.4	−63.2	1.2	−65.7	−60.8	NEW
G334.39−0.18	16 25 26.0	−49 30 42	5.9	−123.8	2.6	–	–	NEW
G334.68+0.13	16 25 17.7	−49 05 33	9.0	−94.4	0.9	−106.0	−85.2	NEW
G334.94−0.34	16 28 31.4	−49 13 58	6.0	−35.7	1.3	–	–	NEW
G335.08−0.42	16 29 25.6	−49 11 28	36.3	−90.9	2.0	−92.7	−35.2	2
G335.23−0.33	16 29 41.6	−49 01 08	3.1	−52.3	2.4	−53.5	−31.8	NEW
G335.29−0.13	16 29 01.2	−48 49 56	2.0	−49.2	0.9	–	–	NEW
G335.43−0.24	16 30 07.0	−48 48 18	23.2	−40.8	1.0	−43.1	−39.7	NEW
G335.59−0.29	16 30 58.4	−48 43 36	34.7	−45.4	1.2	−60.6	−27.2	2
G335.70+0.20	16 29 17.2	−48 18 43	45.3	−45.3	0.7	−57.6	−44.4	2
G335.79+0.18	16 29 46.8	−48 15 42	39.0	−63.8	1.0	−91.1	−47.8	9
G336.13+0.26	16 30 47.6	−47 57 23	20.3	−46.6	1.1	−68.1	−28.0	NEW
G336.25−0.49	16 34 36.6	−48 22 56	4.8	−57.5	2.9	–	–	NEW
G336.50−0.26	16 34 36.0	−48 02 18	28.4	−24.9	1.0	–	–	NEW
G336.53−0.18	16 34 21.7	−47 57 34	3.0	−88.9	3.1	–	–	NEW
G336.83−0.38	16 36 26.5	−47 52 28	8.8	−20.1	1.4	–	–	2
G336.87+0.01	16 34 54.8	−47 35 28	6.7	−67.7	0.8	–	–	2
G336.88+0.01	16 34 58.4	−47 34 53	6.8	−72.5	0.7	–	–	2
G336.96−0.22	16 36 16.6	−47 40 45	5.4	−56.7	0.9	–	–	NEW
G337.00−0.03	16 35 34.9	−47 30 50	254.4	−120.3	1.5	−130.1	−112.0	25
G337.00−0.33	16 36 53.9	−47 42 57	55.5	−33.2	1.0	−49.7	−30.5	NEW
G337.13−0.07	16 36 15.8	−47 26 59	7.5	−61.3	0.9	–	–	NEW
G337.17−0.03	16 36 17.1	−47 23 32	15.4	−67.1	2.0	–	–	NEW
G337.21+0.12	16 35 47.5	−47 16 02	25.1	−71.8	5.9	−75.2	−65.8	NEW
G337.36+0.01	16 36 51.9	−47 13 39	5.3	−99.7	1.5	–	–	NEW
G337.40−0.40	16 38 49.2	−47 27 55	166.3	−40.6	0.9	−41.6	−37.0	25
G337.42−0.16	16 37 49.7	−47 17 40	166.0	−25.0	0.8	−26.1	−19.3	NEW
G337.62−0.06	16 38 10.4	−47 04 41	15.5	−49.7	1.3	−59.0	−45.1	9
G337.64+0.15	16 37 21.1	−46 55 39	3.5	−150.6	2.4	–	–	2
G337.72−0.06	16 38 32.9	−47 00 14	40.1	−52.6	1.4	−127.0	−34.2	9
G337.72+0.08	16 37 57.7	−46 54 21	33.9	−74.0	1.1	−143.2	25.2	NEW
G337.87+0.27	16 37 43.6	−46 40 27	100.6	−43.9	1.2	−82.5	−41.7	25
G337.88−0.11	16 39 26.7	−46 54 55	1.7	−49.8	2.9	–	–	NEW
G337.92−0.48	16 41 12.1	−47 07 57	677.2	−36.5	0.5	−68.5	−27.5	42
G338.00+0.13	16 38 50.0	−46 39 58	12.3	−37.0	3.4	−51.4	−33.9	9
G338.00−0.13	16 39 59.8	−46 50 38	5.5	−62.6	2.7	−65.7	−44.5	NEW
G338.17−0.07	16 40 20.9	−46 40 26	4.7	−57.7	1.0	–	–	NEW
G338.28−0.19	16 41 20.5	−46 40 11	5.0	−90.7	1.0	−92.1	−87.5	NEW
G338.29+0.12	16 40 02.0	−46 27 32	16.2	−38.7	1.2	−75.7	−33.6	NEW
G338.39−0.01	16 40 57.7	−46 28 01	63.2	−46.1	1.0	–	–	NEW
G338.39+0.16	16 40 14.2	−46 21 23	1.4	−29.1	3.2	−37.3	−23.2	NEW
G338.44+0.06	16 40 49.1	−46 23 11	4.7	−41.8	1.4	–	–	NEW
G338.47−0.25	16 42 18.1	−46 34 11	25.7	−52.9	0.7	–	–	2
G338.48+0.29	16 39 58.8	−46 12 21	16.2	−53.3	1.5	–	–	2
G338.50+0.05	16 41 07.2	−46 20 49	18.5	−41.3	1.5	–	–	NEW
G338.58+0.11	16 41 09.3	−46 15 08	10.8	−76.4	1.7	–	–	2
G338.68−0.08	16 42 24.2	−46 17 52	1.8	−22.1	1.6	–	–	2
G339.06+0.15	16 42 50.3	−45 51 38	10.5	−82.0	1.3	−90.2	−80.4	NEW

Table 2 – *continued*

Source name	RA (J2000) (h m s)	Dec. (J2000) (° ′ ″)	Strongest maser spot Peak flux density (Jy)	Velocity (km s^{-1})	FWHM (km s^{-1})	Velocity range Min (km s^{-1})	Max (km s^{-1})	Comments[1]
G339.16−0.29	16 45 06.1	−46 04 09	3.1	−19.7	1.1	–	–	NEW
G339.20−0.02	16 44 05.8	−45 51 46	10.5	−14.6	0.7	–	–	NEW
G339.48+0.18	16 44 15.7	−45 31 26	2.9	−90.9	0.8	–	–	NEW
G339.52+0.27	16 44 01.2	−45 25 55	2.8	−14.5	0.7	−30.7	−13.7	NEW
G339.54−0.42	16 47 05.4	−45 52 11	1.2	−48.4	5.7	–	–	NEW
G339.59−0.14	16 46 02.7	−45 38 50	11.7	−33.2	1.2	−38.3	−24.6	9
G339.62−0.13	16 46 07.7	−45 36 59	238.9	−33.3	0.9	−38.4	−26.9	9
G339.75+0.10	16 45 37.0	−45 22 30	1.9	−77.9	4.4	–	–	NEW
G339.92−0.09	16 47 03.8	−45 21 38	6.0	−57.0	1.1	–	–	NEW
G340.05−0.24	16 48 12.5	−45 21 52	69.1	−55.2	2.0	−57.1	−46.4	9
G340.12−0.02	16 47 28.7	−45 10 05	69.9	−125.3	1.7	–	–	NEW
G340.13−0.18	16 48 15.6	−45 15 44	4.1	−4.7	1.7	–	–	NEW
G340.23−0.37	16 49 25.6	−45 18 14	52.0	−54.6	0.9	–	–	NEW
G340.25−0.04	16 48 04.4	−45 04 58	7.2	−127.6	1.5	–	–	NEW
G340.28−0.21	16 48 53.1	−45 10 14	10.7	−48.2	1.0	−49.0	−14.2	NEW
G340.29−0.03	16 48 11.2	−45 02 41	3.5	−114.3	3.4	−117.2	−111.7	NEW
G341.13−0.38	16 52 40.5	−44 37 23	11.0	−40.7	0.7	–	–	NEW
G341.22−0.21	16 52 16.7	−44 26 45	86.4	−40.9	1.0	−49.8	−37.9	3
G341.28+0.36	16 50 04.8	−44 02 03	10.0	−153.4	1.6	−157.6	−119.4	NEW
G341.31+0.19	16 50 52.8	−44 07 16	5.9	−110.6	1.8	−119.9	−103.5	NEW
G341.67+0.09	16 52 34.8	−43 54 28	7.3	−19.6	1.3	–	–	NEW
G341.99+0.26	16 53 00.3	−43 33 07	7.4	−38.1	1.1	−46.1	−19.8	39
G342.09+0.42	16 52 40.8	−43 22 23	34.8	−162.1	4.7	–	–	NEW
G342.33+0.10	16 54 50.6	−43 23 34	6.7	−97.5	1.6	−98.4	−92.4	NEW
G342.37+0.14	16 54 48.5	−43 20 01	8.1	−5.9	0.8	–	–	NEW
G342.47+0.20	16 54 55.9	−43 12 50	12.5	−50.5	0.7	−50.3	−31.0	NEW
G342.63−0.09	16 56 42.0	−43 16 46	3.3	−12.4	1.2	–	–	NEW
G343.13−0.06	16 58 16.4	−42 52 08	44.0	−19.8	0.8	−43.1	−14.8	9
G343.19−0.37	16 59 49.3	−43 00 26	3.1	−133.5	2.6	−135.7	−106.4	NEW
G343.48−0.06	16 59 28.4	−42 35 12	5.2	−33.3	1.4	–	–	NEW
G343.50−0.00	16 59 17.5	−42 32 20	21.9	−81.8	0.8	–	–	NEW
G343.50−0.06	16 59 32.3	−42 34 29	3.5	−34.3	1.0	–	–	NEW
G343.53−0.02	16 59 26.6	−42 31 45	11.0	−83.1	1.5	–	–	NEW
G343.69−0.02	16 59 59.7	−42 23 47	27.5	−36.0	1.2	−51.6	−31.6	NEW
G343.72−0.18	17 00 47.4	−42 28 47	13.8	36.3	1.2	–	–	NEW
G343.73−0.11	17 00 31.6	−42 25 13	20.5	−32.5	0.8	–	–	NEW
G343.75−0.15	17 00 45.3	−42 25 58	36.1	−23.5	0.9	−61.2	−22.1	NEW
G343.81+0.16	16 59 38.7	−42 11 54	7.6	22.2	1.2	–	–	NEW
G344.03−0.11	17 01 29.7	−42 11 26	78.7	−52.1	3.1	−60.2	−42.1	NEW
G344.30+0.16	17 01 16.1	−41 48 35	68.0	−30.2	5.5	–	–	NEW
G344.58−0.02	17 02 56.6	−41 42 13	1266.3	−4.1	1.5	−19.0	8.8	3
G344.65−0.22	17 04 00.3	−41 45 40	9.3	−60.2	1.3	–	–	NEW
G344.78−0.25	17 04 34.9	−41 40 29	4.6	−18.3	1.0	–	–	NEW
G344.89+0.12	17 03 23.0	−41 22 01	15.0	−28.5	1.4	−37.6	−25.1	NEW, 49 - S star
G344.93+0.02	17 03 56.6	−41 23 41	8.3	−22.6	3.2	−24.9	−18.0	50 - Mira variable
G345.13−0.16	17 05 17.9	−41 20 54	19.3	−25.1	1.3	−27.3	−19.0	NEW
G345.25−0.03	17 05 08.2	−41 10 06	16.4	−23.6	1.4	–	–	NEW
G345.43−0.06	17 05 51.8	−41 02 33	54.6	−14.3	1.0	−28.5	−11.2	2
G345.44+0.21	17 04 46.2	−40 52 28	10.9	−16.6	1.5	−20.7	1.1	NEW
G345.50+0.36	17 04 19.6	−40 44 14	4.1	−19.7	0.5	−28.8	−12.0	41
G345.58−0.02	17 06 10.2	−40 53 53	5.8	−8.8	1.7	–	–	NEW
G345.65+0.02	17 06 14.4	−40 49 27	48.4	−11.3	3.8	−19.9	−0.4	39
G345.69−0.08	17 06 45.7	−40 50 46	297.0	−6.6	3.6	−13.9	87.6	42
G345.80−0.34	17 08 14.1	−40 55 11	3.6	−94.6	1.7	–	–	NEW
G345.83−0.05	17 07 04.7	−40 43 29	5.2	−6.9	0.7	–	–	NEW
G345.91−0.05	17 07 20.5	−40 39 30	2.7	−125.5	0.9	–	–	NEW
G345.98−0.01	17 07 22.6	−40 34 46	13.3	−77.5	1.3	–	–	NEW
G346.18−0.08	17 08 18.9	−40 27 11	7.3	−14.3	0.7	–	–	NEW
G346.18+0.34	17 06 34.1	−40 12 13	4.1	3.0	1.2	–	–	NEW
G346.47−0.23	17 09 52.2	−40 19 10	2.9	−76.3	2.6	–	–	NEW
G346.52+0.11	17 08 35.6	−40 04 34	6.2	3.2	1.9	–	–	2

Table 2 – *continued*

Source name	RA (J2000) (h m s)	Dec. (J2000) (° ′ ″)	Strongest maser spot Peak flux density (Jy)	Velocity (km s−1)	FWHM (km s−1)	Velocity range Min (km s−1)	Max	Comments[1]
G346.53−0.12	17 09 33.8	−40 12 14	11.0	−47.4	0.6	–	–	NEW
G347.06+0.00	17 10 43.6	−39 42 17	3.7	−9.7	1.9	–	–	NEW
G347.23+0.02	17 11 10.0	−39 33 39	6.8	−77.8	1.2	−89.5	−73.5	NEW
G347.30+0.13	17 10 54.7	−39 25 54	42.3	−82.6	2.4	−98.4	−75.9	46
G347.32+0.02	17 11 26.9	−39 29 12	3.2	−8.5	1.1	–	–	NEW
G347.63+0.16	17 11 48.0	−39 09 18	15.0	−65.2	1.1	−127.9	−62.8	3
G347.63+0.22	17 11 34.9	−39 06 46	9.0	−90.2	1.7	–	–	51
G347.89−0.28	17 14 27.1	−39 11 52	4.9	−91.2	4.3	−94.4	−78.5	NEW
G348.18+0.48	17 12 06.9	−38 31 07	80.7	−1.4	0.7	−20.9	−0.8	39
G348.29+0.43	17 12 40.4	−38 27 12	5.2	−2.0	0.9	–	–	NEW
G348.32−0.18	17 15 16.6	−38 47 23	6.4	−100.8	1.4	−111.8	−97.2	NEW
G348.83+0.23	17 15 09.3	−38 08 11	3.5	−186.6	2.8	–	–	NEW
G348.89−0.18	17 17 01.0	−38 19 34	29.9	10.5	0.7	–	–	3
G349.10+0.11	17 16 24.5	−37 59 31	27.0	−79.5	2.4	−83.2	−69.8	25
G349.72+0.13	17 18 10.3	−37 28 14	149.6	17.9	2.7	11.6	22.5	NEW
G349.80+0.11	17 18 27.8	−37 25 06	107.5	−60.6	1.0	–	–	NEW
G350.11+0.09	17 19 25.9	−37 10 25	28.4	−72.9	4.3	−76.5	−27.8	3
G350.42−0.06	17 20 55.9	−37 00 24	62.4	−36.1	0.9	−37.0	−21.4	NEW
G350.53−0.34	17 22 24.5	−37 04 40	5.3	−17.3	0.7	–	–	NEW
G350.69−0.48	17 23 27.7	−37 01 15	60.3	−14.2	0.5	–	–	NEW
G350.88−0.29	17 23 11.6	−36 45 40	9.6	−53.9	1.0	–	–	NEW
G351.38+0.21	17 22 33.0	−36 04 00	5.3	7.3	0.7	–	–	NEW
G351.58−0.35	17 25 24.8	−36 12 34	137.9	−94.0	2.4	−96.0	−88.6	3
G351.62+0.18	17 23 21.6	−35 53 09	11.5	−42.2	0.8	−88.1	−9.7	NEW
G352.16+0.41	17 23 53.8	−35 18 18	158.7	−4.3	0.9	–	–	NEW
G352.21+0.10	17 25 17.3	−35 26 15	7.0	−28.2	0.7	−29.1	−21.6	NEW
G352.25−0.29	17 26 59.8	−35 37 16	6.4	−96.2	3.2	−98.6	−93.5	NEW
G352.55+0.20	17 25 49.2	−35 05 53	9.9	−52.2	0.6	–	–	NEW
G352.93+0.07	17 27 22.9	−34 51 40	8.9	−2.7	1.2	–	–	NEW, 52 – AGB star
G353.22−0.24	17 29 26.4	−34 47 30	85.7	−19.3	0.6	−22.7	−13.8	NEW
G353.26−0.24	17 29 33.0	−34 45 27	9.3	7.0	0.9	–	–	NEW
G353.39+0.43	17 27 11.0	−34 16 18	22.7	−40.6	4.4	−58.1	−10.1	NEW
G353.42−0.37	17 30 29.0	−34 41 38	10.9	−19.7	1.0	–	–	9
G353.82+0.32	17 28 47.4	−33 58 58	128.9	−70.5	2.6	–	–	NEW
G354.31−0.11	17 31 48.2	−33 48 25	13.7	9.0	0.8	6.5	17.9	NEW
G355.13−0.30	17 34 44.0	−33 13 07	106.4	224.8	1.0	4.3	227.6	NEW
G355.18−0.42	17 35 20.0	−33 14 23	21.1	0.2	1.8	−4.8	1.7	NEW
G355.34+0.15	17 33 28.1	−32 47 59	47.7	9.6	0.9	–	–	3
G355.79−0.18	17 35 55.6	−32 35 51	9.8	−2.1	0.7	–	–	NEW
G355.82+0.28	17 34 09.9	−32 19 43	14.2	−114.5	1.2	−117.0	−88.9	NEW
G355.93−0.34	17 36 57.4	−32 34 03	12.8	−49.7	1.7	−65.2	−42.8	NEW
G356.43+0.10	17 36 27.8	−31 55 07	2.8	−6.6	0.8	–	–	NEW
G356.47+0.01	17 36 54.7	−31 55 46	17.3	1.3	1.1	–	–	NEW
G356.55+0.08	17 36 49.4	−31 49 09	8.3	−19.0	2.7	−21.4	−15.0	NEW
G356.65−0.32	17 38 40.0	−31 56 57	11.7	4.6	3.1	−13.7	17.3	9
G357.57−0.32	17 40 57.6	−31 10 23	95.0	−8.4	1.9	−10.1	7.0	NEW
G357.57+0.07	17 39 27.5	−30 57 47	1.3	−48.0	4.6	–	–	NEW
G357.93−0.34	17 41 56.6	−30 52 56	15.4	1.4	0.8	–	–	NEW
G357.97−0.16	17 41 19.1	−30 44 58	130.7	−50.8	4.5	−70.6	92.6	46
G358.24+0.12	17 40 54.9	−30 22 16	94.0	−13.3	0.7	−15.6	−1.4	3
G358.30+0.08	17 41 11.5	−30 20 24	78.4	−9.2	1.1	−17.6	6.4	53
G358.39−0.48	17 43 38.9	−30 33 36	47.2	−0.6	2.7	−4.5	1.2	53
G358.47−0.38	17 43 26.1	−30 26 37	13.1	−4.7	1.1	–	–	NEW
G358.48−0.33	17 43 14.7	−30 23 58	10.0	0.3	1.0	–	–	NEW
G358.67−0.04	17 42 34.8	−30 05 39	60.9	−9.0	1.5	−21.1	−5.0	3
G358.88+0.04	17 42 46.5	−29 51 59	8.5	−17.6	2.0	−18.9	−10.3	NEW
G359.14+0.03	17 43 27.2	−29 39 23	498.7	−1.7	1.9	−13.2	24.6	54
G359.30+0.03	17 43 50.2	−29 30 50	20.1	0.9	1.5	−33.1	3.2	NEW
G359.42+0.07	17 43 57.1	−29 23 35	4.3	−5.3	1.5	–	–	NEW
G359.42+0.32	17 42 59.8	−29 15 49	4.4	9.5	0.8	–	–	NEW

Table 2 – *continued*

Source name	RA (J2000) (h m s)	Dec. (J2000) (° ′ ″)	Strongest maser spot Peak flux density (Jy)	Velocity ($km\,s^{-1}$)	FWHM ($km\,s^{-1}$)	Velocity range ($km\,s^{-1}$) Min	Max	Comments[1]
G359.44−0.10	17 44 41.1	−29 28 08	18.1	−58.4	2.2	–	–	3
G359.51−0.15	17 45 02.4	−29 25 59	5.6	7.2	0.8	–	–	53
G359.62−0.25	17 45 40.4	−29 23 35	106.4	−15.9	1.5	−25.5	11.6	3
G359.73−0.38	17 46 28.9	−29 21 56	42.2	−4.8	0.6	−14.8	−1.6	1
G359.94−0.15	17 46 03.4	−29 03 57	10.6	−18.7	1.7	−20.9	24.7	55
G359.97−0.46	17 47 21.6	−29 12 08	26.3	26.8	0.7	3.9	27.5	3

[1] ‘NEW’ indicates a newly detected maser, otherwise a number (refer to Table 3) is given for a previous detection. The majority of masers are presumed to be associated with star formation. Previously known associations with evolved stars are referenced, but we await higher precision positions to associate the majority of masers.

of multiple maser sites, so that 540 maser sites are almost certainly a lower limit.

There are 303 H_2O maser sites that show more than one peak in the maser spectrum (we refer to such single peaks in the spectrum as maser spots). Of these sites with more than one maser spot, the widest velocity distribution is exhibited by G9.10−0.40, over 351.3 $km\,s^{-1}$. This maser site was previously reported by Walsh et al. (2009), based on HOPS data, and is a water fountain associated with a post-AGB star. Subsequent observations by Walsh et al. (2009) found maser emission over an even wider range of 398 $km\,s^{-1}$.

In total, there are 14 maser sites with maser spots spread over a velocity range greater than 100 $km\,s^{-1}$. The median velocity spread is 17 $km\,s^{-1}$. The distribution of velocity spreads of maser sites with multiple maser spots can be seen in Fig. 7. The figure shows that the occurrence of maser sites with high-velocity features is relatively rare, but there is a population of about 10 per cent of maser sites with maser spots that span velocity ranges greater than 50 $km\,s^{-1}$.

When comparing the line FWHM of maser spots, we find that G27.08+0.20 exhibits the widest FWHM of 13.3 $km\,s^{-1}$. However, because maser sites usually consist of multiple peaks in the spectrum, it is likely that any single peak may comprise multiple unresolved components in the spectrum. This is likely to be the case for G27.08+0.20, whose H_2O maser emission is very weak and dominated by noise, possibly masking multiple components. The median line FWHM is 1.2 $km\,s^{-1}$ and 90 per cent of maser spots are no broader than 3.1 $km\,s^{-1}$.

In Table 2, the last column indicates whether a maser site is coincident with the position and shows similar spectral features to the H_2O maser emission from a known evolved star. There are 15 maser sites so far associated with evolved stars. Due to the 2arcmin beam of the Mopra observations, we await higher resolution observations to associate all masers with a particular class of astrophysical object. There are certainly known evolved stars within 2.2 arcmin of H_2O masers which we have not yet associated because we cannot compare our H_2O maser spectrum to a previously published spectrum. We thus expect there to be more associations with evolved stars to be uncovered, but with the majority of maser sites associated with star-forming regions. See Section 7.4 for further evidence that leads us to this expectation. We plan to conduct follow-up observations of the maser sites with the ATCA, which will give us high positional accuracy, allowing us to identify the majority of maser sites with known astrophysical objects.

7 DISCUSSION

7.1 Noise measurements

We expect the noise level in our spectra to vary by about a factor of 2 because observations were made at a range of elevations and weather conditions, which gave rise to system temperature variations in the range 50–120 K. In order to determine the sensitivity limits of the water maser data, we measure the rms noise levels for each quarter square degree. This is done by taking a single channel from the data cube where no emission is expected (typically a channel at a velocity of +250 $km\,s^{-1}$ was used). Then the rms noise is measured for each quarter square degree using the MIRIAD task IMSTATS. We also check the noise levels at different parts of each zoom band and find that the noise does not vary significantly within each zoom. This is done for each of the IFs containing the H_2O maser, NH_3 (1,1), HCCCN (3–2) and H69α emission. These IFs were chosen because they contain the most important emission lines in the survey and because they sample close to the full range of frequencies observed in HOPS from 19.6 (H69α) to 27.3 GHz (HCCCN (3–2)).

Fig. 8 shows histograms of the noise levels measured for each of the IFs. The rms noise levels are typically around 0.15–0.2 K in terms of main beam brightness temperature. We show the H_2O maser rms noise level in terms of Jy, as this is a more typical intensity scale used for masers (assuming 12.4 $Jy\,K^{-1}$). For H_2O masers, we find that the rms noise level is below 2 Jy for 95 per cent of the survey and below 1.4 Jy for 50 per cent of the survey. The full range of noise levels varies by a factor of 2.9, but we find that 87 per cent of the H_2O maser observations are characterized by an rms noise level between 1 and 2 Jy.

We find that 90 per cent of the rms noise levels in the IFs containing NH_3 (1,1), H69α and HCCCN (3–2) emission are between 0.12 and 0.24 K. Thus, we consider that the rms noise levels in the survey are well characterized by the variation of a factor of 2, but note that approximately 10 per cent of the rms noise levels in the survey lie outside this range.

7.2 H_2O maser completeness limits

In order to estimate the completeness of the H_2O maser observations, we took an H_2O maser data cube, with a representative noise level of 1.5 Jy (rms), but without any identified H_2O masers. We injected fake signals into the spectrum, using the IMGEN task in MIRIAD, to mimic the typical characteristics of a real H_2O maser: a

Table 3. References for Table 2.

Comment in Table 2	Reference
1	Caswell, Breen & Ellingsen (2011)
2	Breen et al. (2010)
3	Caswell et al. (1983a)
4	Genzel & Downes (1977)
5	Mehringer et al. (1998)
6	Benson et al. (1990)
7	Palla et al. (1991)
8	Kazarovets et al. (2006)
9	Batchelor et al. (1980)
10	Brand et al. (1994)
11	Healy, Hester & Claussen (2004)
12	Caswell et al. (1983b)
13	Kleinmann, Sargent & Dickinson (1978)
14	Deacon et al. (2007)
15	Genzel & Downes (1979)
16	Churchwell, Walmsley & Cesaroni (1990)
17	Engels, Schmid-Burgk & Walmsley (1986)
18	Forster & Caswell (1989)
19	Codella et al. (1995)
20	Johnston, Sloanacker & Bologna (1973)
21	Jaffe, Guesten & Downes (1981)
22	Urquhart et al. (2009)
23	Benson & Little-Marenin (1996)
24	Nassau, Blanco & Morgan (1954)
25	Caswell et al. (1976)
26	Matthews et al. (1985)
27	Comoretto et al. (1990)
28	Deguchi et al. (2007)
29	Alksnis et al. (2001)
30	Sevenster et al. (2001)
31	Szymczak, Pillai & Menten (2005)
32	Palagi et al. (1993)
33	Wood & Churchwell (1989a)
34	Messineo et al. (2002)
35	Codella et al. (1994)
36	Braz et al. (1989)
37	Deguchi, Nakada & Forster (1989)
38	Caswell et al. (1989)
39	Braz & Scalise (1982)
40	Walsh et al. (2008)
41	Kaufmann et al. (1976)
42	Caswell et al. (1974)
43	Johnston et al. (1972)
44	Caswell & Breen (2010)
45	Sloan & Price (1998)
46	Scalise, Rodriguez & Mendoza-Torres (1989)
47	Breen et al. (2007)
48	Le Bertre, Heydari-Malayeri & Epchtein (1988)
49	Westerlund & Olander (1978)
50	Deacon et al. (2007)
51	Kaufmann et al. (1977)
52	Le Bertre et al. (2003)
53	Taylor, Morris & Schulman (1993)
54	Forster & Caswell (2000)
55	Sjouwerman et al. (2002)

three-dimensional Gaussian with the size of the beam in the spatial axes and linewidth being the same as the median H_2O maser linewidth of 1.2 km s^{-1}. The same data reduction routines and visualisation methods were used to identify the fake masers. In each test we used 100 fake masers and each test was repeated for four discrete input flux densities. We found the following successful recovery rate of fake masers in the data cube: at 11.1 Jy, we recovered 100 per cent of the fake masers, at 8.4 Jy we recovered 98 per cent, at 6.7 Jy we recovered 86 per cent and at 5.5 Jy we recovered 50 per cent. Therefore, we consider that for typical observing conditions, we are complete to about 10 Jy and 50 per cent complete to about 5.5 Jy.

Fig. 9 shows the distribution of peak flux densities of the strongest maser spot in each maser site. This figure shows that the number of masers sharply rises from the strongest masers down to about 5 Jy, The distribution above the 100 per cent completeness limit (10 Jy) is well matched to a power law with slope −0.66 down to this point (the solid straight line in Fig. 9). The dotted curve extending from the straight line indicates the expected numbers of masers, assuming that the real distribution of maser fluxes would follow the straight line extended to lower flux levels, together with the above completeness figures. The apparent turnover seen in the dotted line is consistent with the distribution of detected maser flux densities, shown by the histogram, given error bars that are based on $\sqrt{N}$ statistics. This means that although the distribution shows a peak of masers, this is likely due to the completeness limit of the survey and not due to an intrinsic turnover in the maser flux density population.

7.3 Other maser detections

Within the HOPS region we made occasional detections of other maser lines towards 11 regions. These include detections from the CH_3OH (J_2–J_1) E series near 25 GHz and the previously unknown masing transition of CH_3OH at 23.444 GHz. The 23.444 GHz CH_3OH detection has been confirmed as a maser by Voronkov et al. (2011). In addition to this, we detected possible maser emission in the NH_3 inversion transitions (11, 9), (8, 6) and (3, 3). Details of the NH_3 detections are given below.

7.3.1 NH_3 (11, 9) and (8, 6)

Emission in these two inversion transitions of NH_3 have previously been reported towards one position: NGC 6334 I (Walsh et al. 2007a) and confirmed as new masing transitions. We detect emission from both transitions in HOPS towards one new position: G19.61−0.23. Spectra of emission in the two transitions are shown in Fig. 10. We also detect H_2O maser emission at this position, as detailed in Table 2 and shown in Fig. 6. However, we note that the emission of the NH_3 transitions at approximately 55.5 km s^{-1} is on the edge of the extent of the H_2O maser emission and about 11 km s^{-1} offset from the strongest H_2O maser spot.

We cannot confirm that these two emission lines are due to masers with the current data, but the fact that the lines are typically narrow [1.5 and 1.1 km s^{-1} for (11, 9) and (8, 6), respectively] and that these transitions have only been previously detected as masers suggests that a maser origin is more likely than a thermal origin.

G19.61−0.23 is a well-known region of high-mass star formation in the Galaxy, containing OH (Caswell & Haynes 1983) and CH_3OH masers (Caswell et al. 1995; Walsh et al. 1998), including the rare 9.9 GHz CH_3OH maser (Voronkov et al. 2010), cold dust continuum emission (Walsh et al. 2003; Thompson et al. 2006), molecular line emission (Santangelo et al. 2010) and multiple ultracompact (UC) H II regions (Garay et al. 1998). Kolpak et al. (2003) determined a distance to G19.61−0.23 of 12.3 kpc, based on HI observations. It is surprising that one of the only two known sources of emission in these NH_3 lines is at such a large distance.

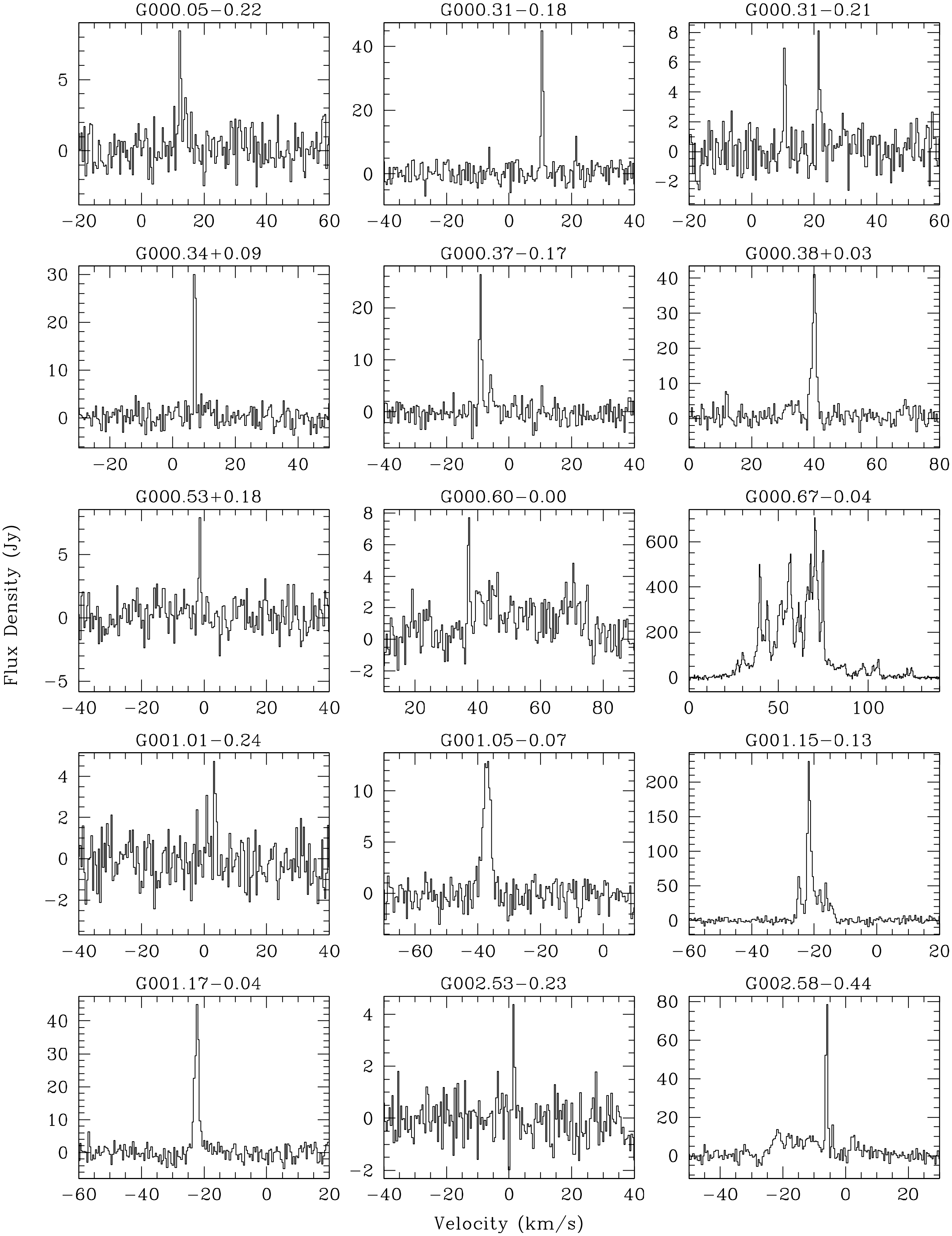

Figure 6. Spectra of water masers. The source name is given at the top of each panel.

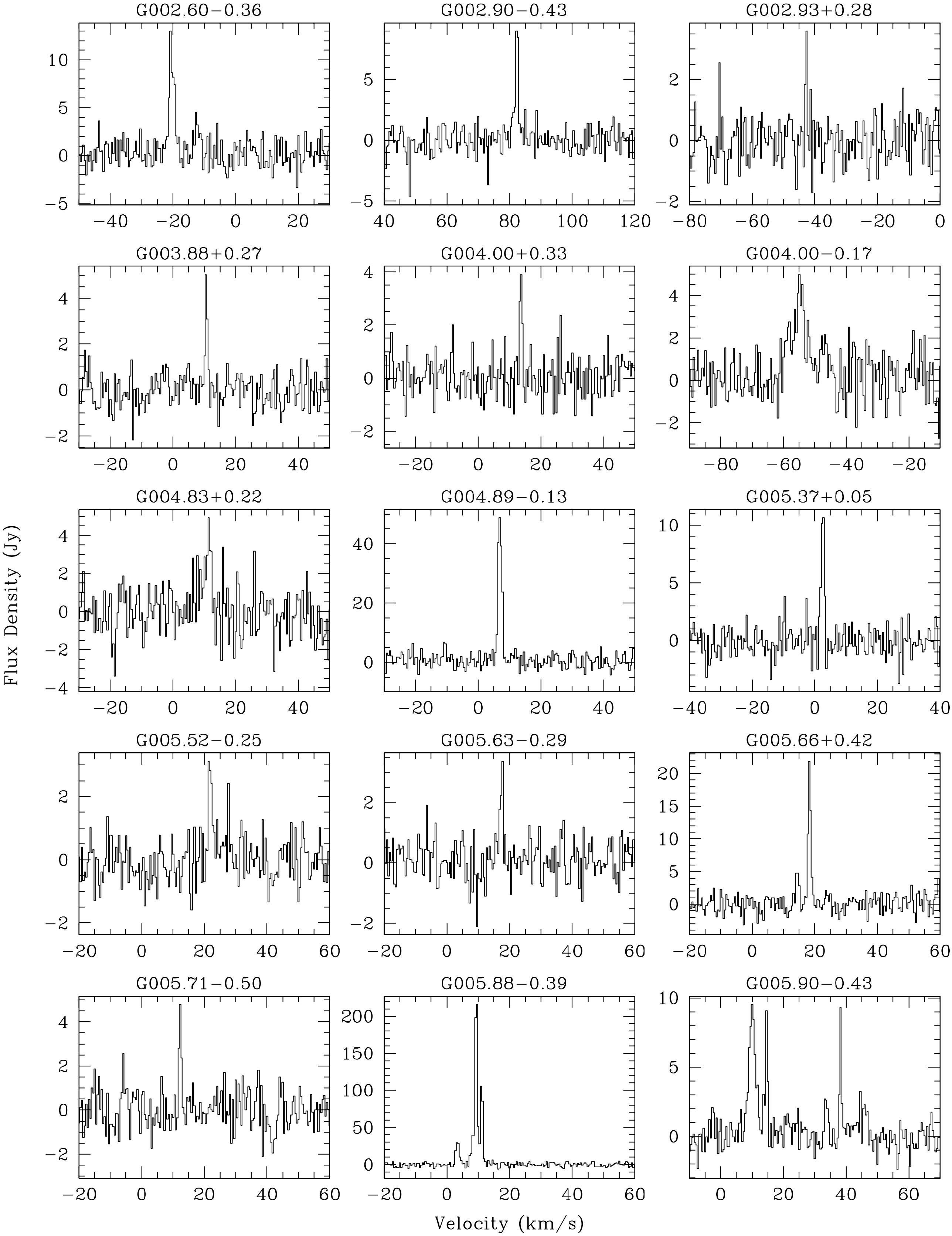

Figure 6 – *continued*

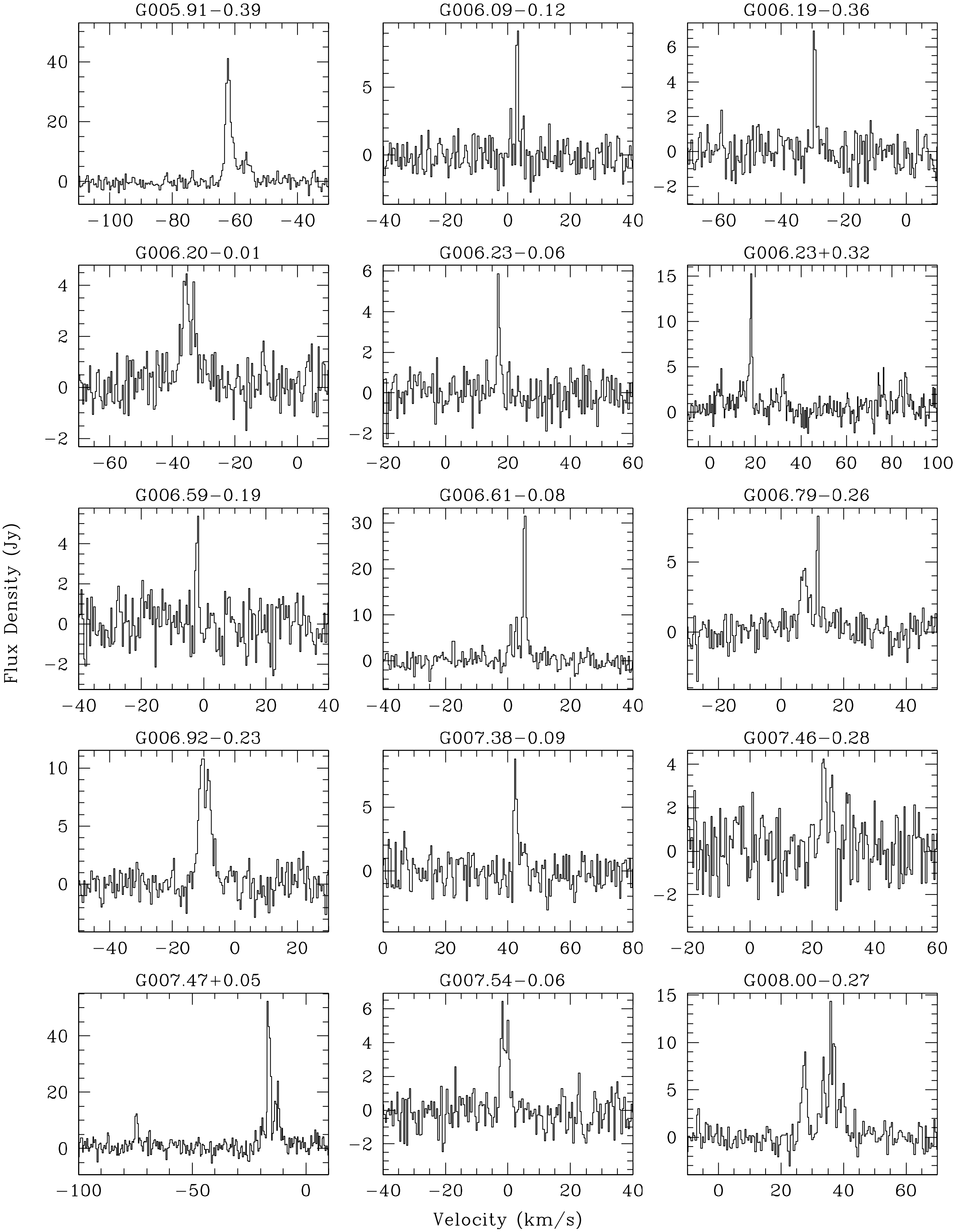

Figure 6 – *continued*

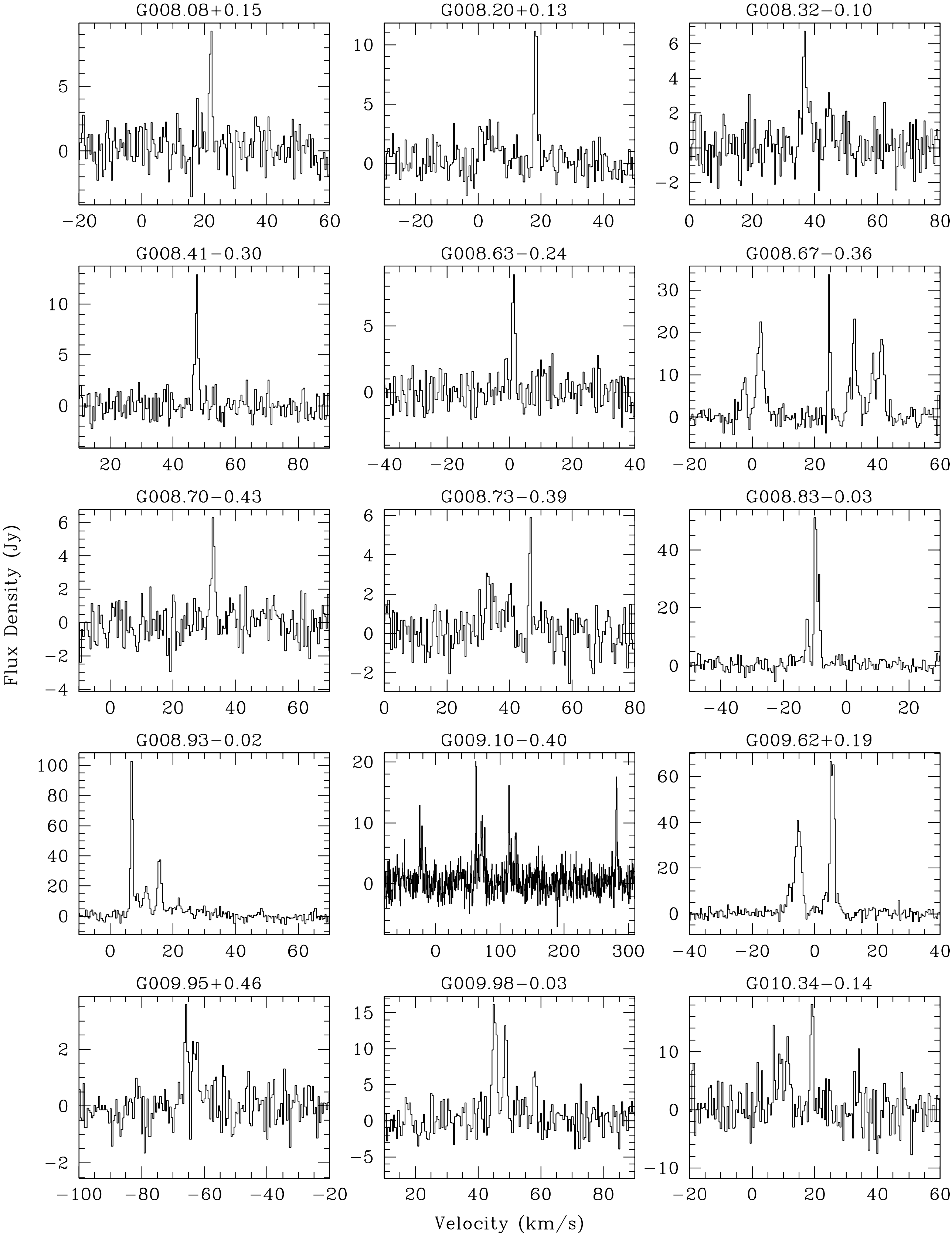

Figure 6 – *continued*

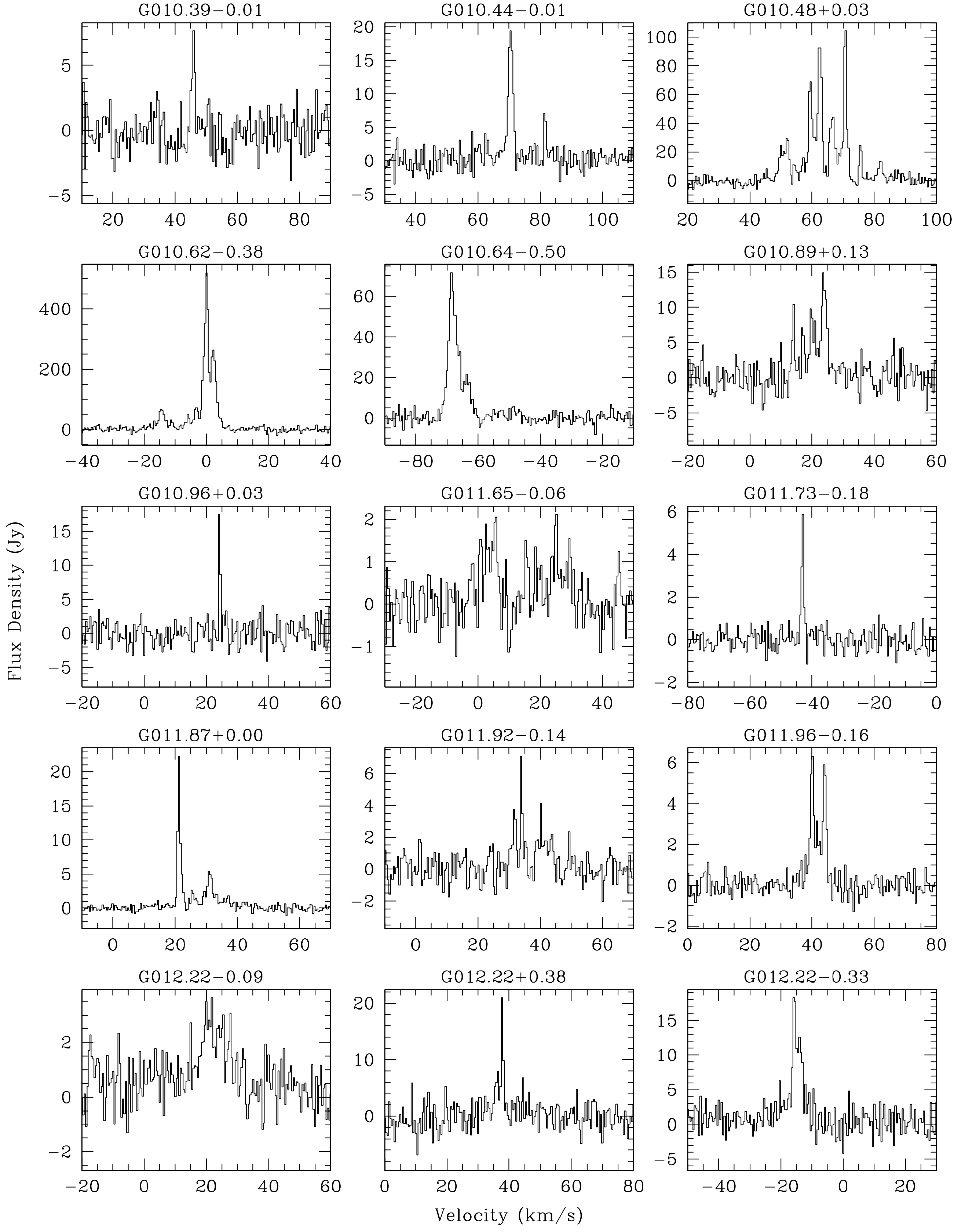

Figure 6 – *continued*

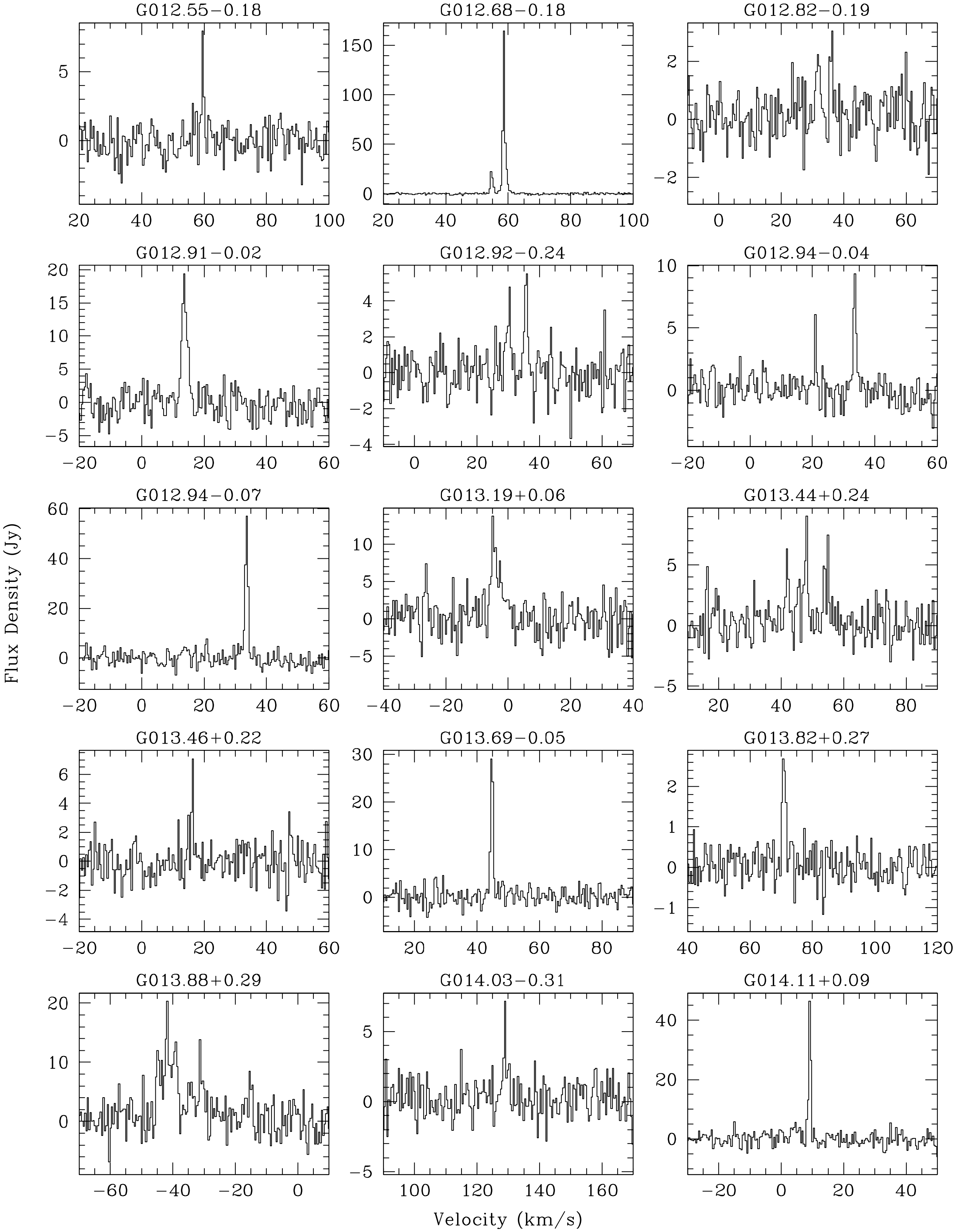

Figure 6 – *continued*

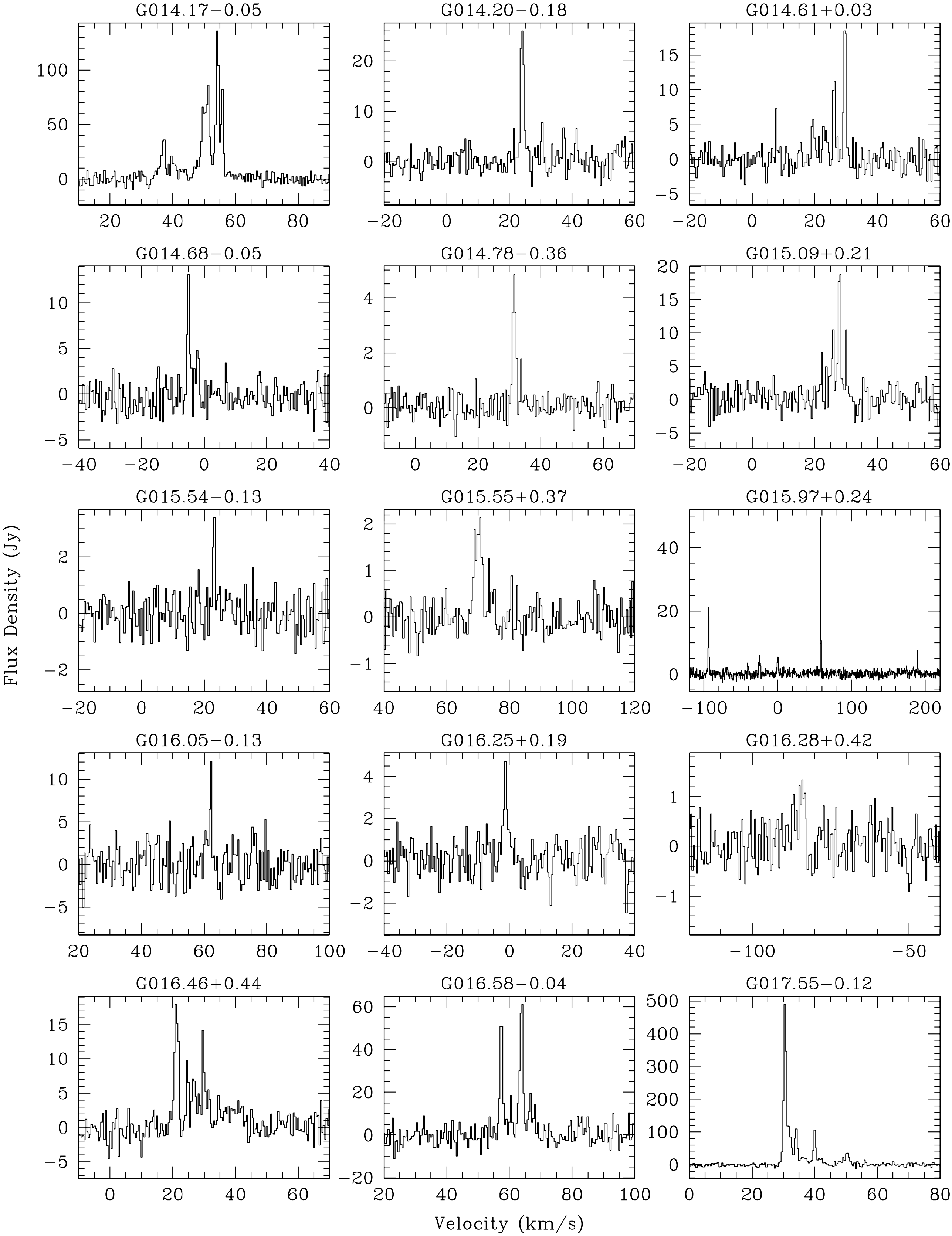

Figure 6 – *continued*

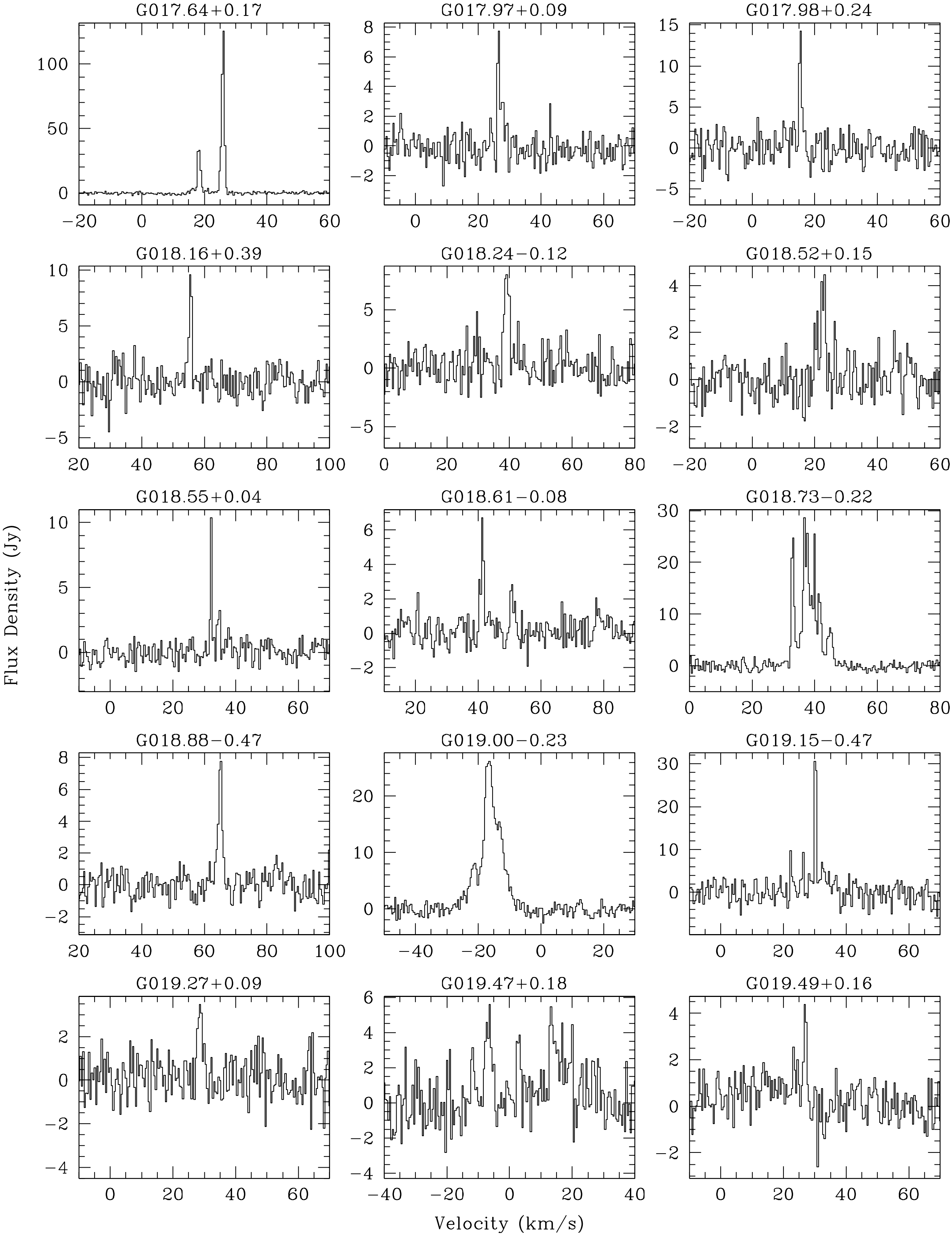

Figure 6 – *continued*

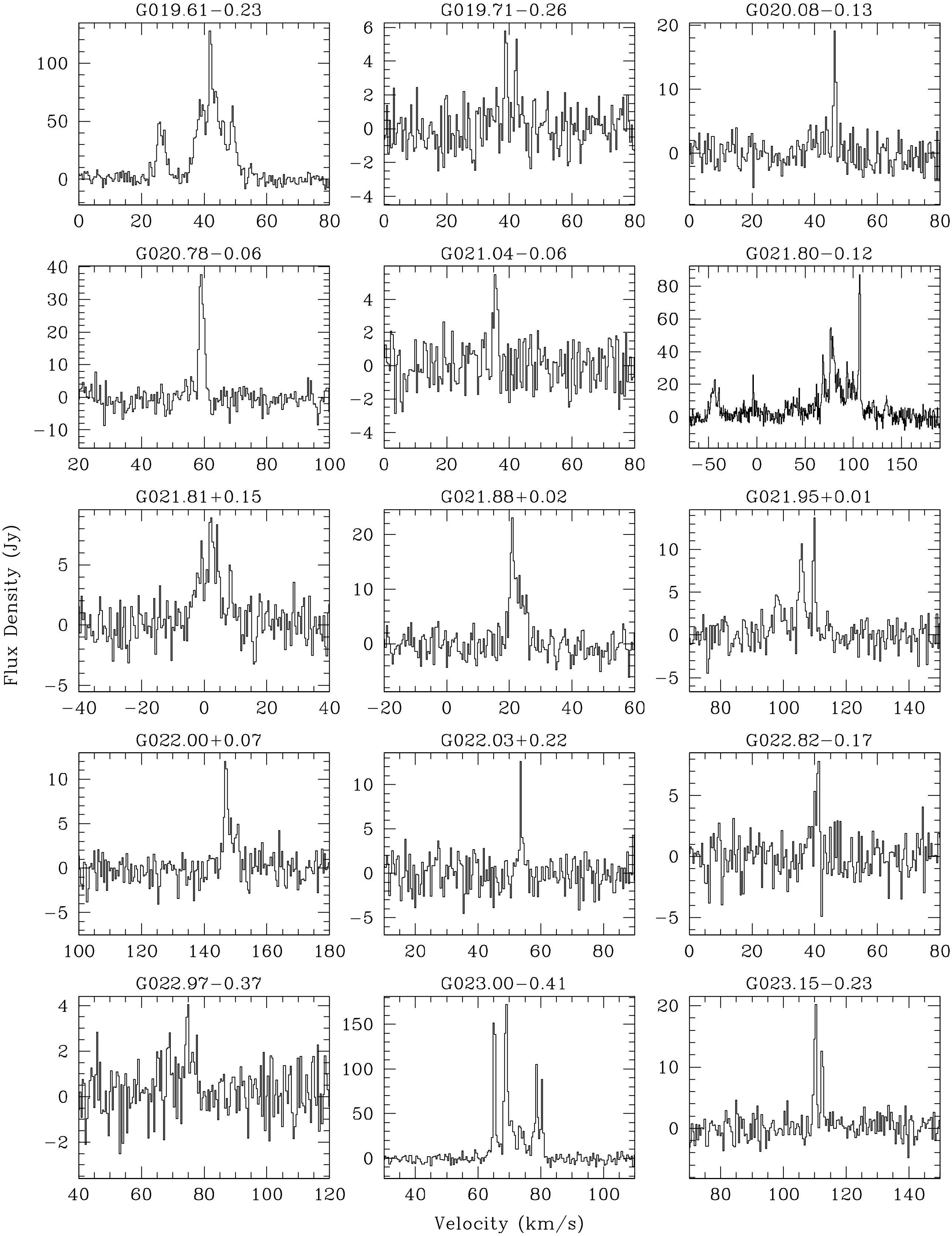

Figure 6 – *continued*

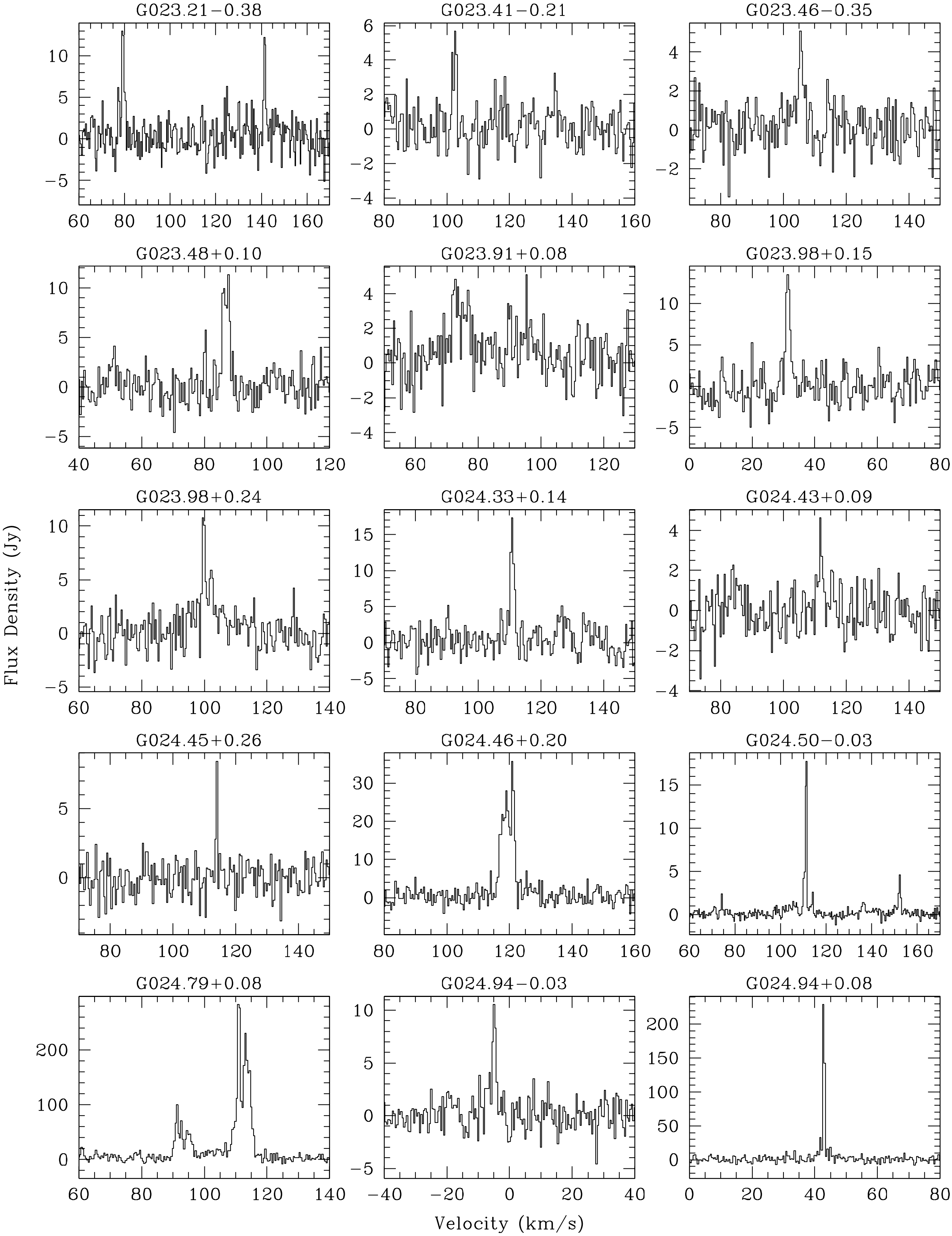

Figure 6 – *continued*

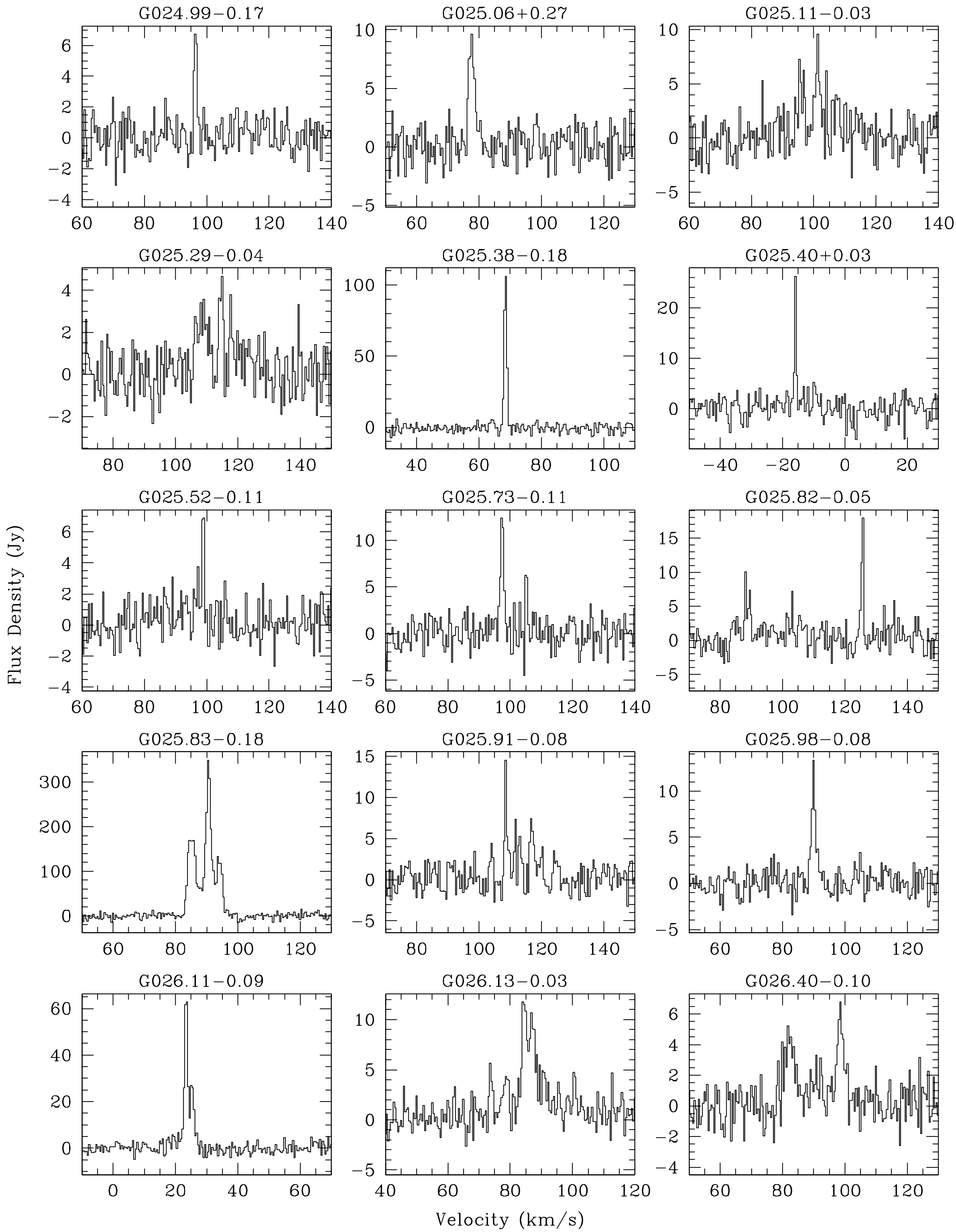

Figure 6 – *continued*

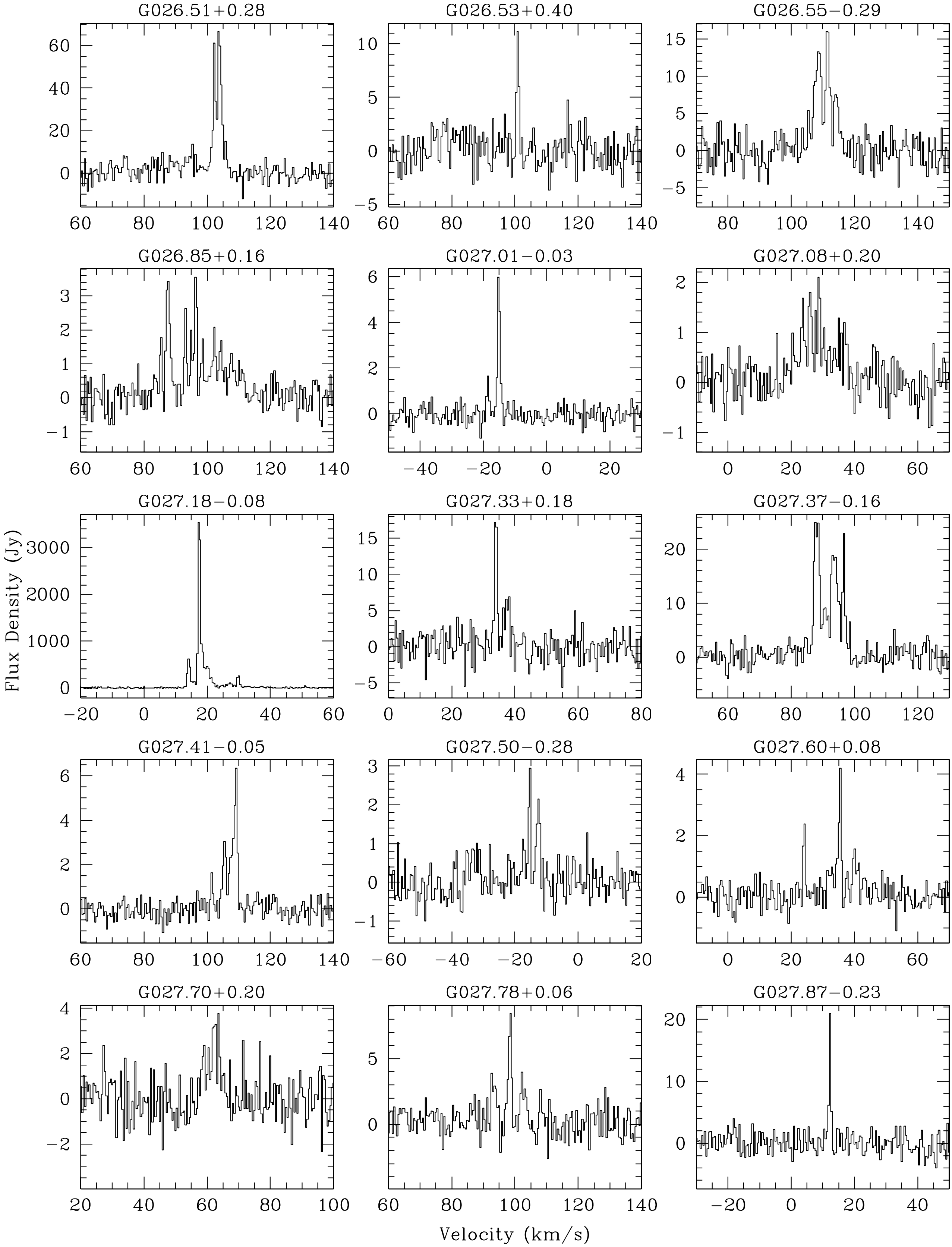

Figure 6 – *continued*

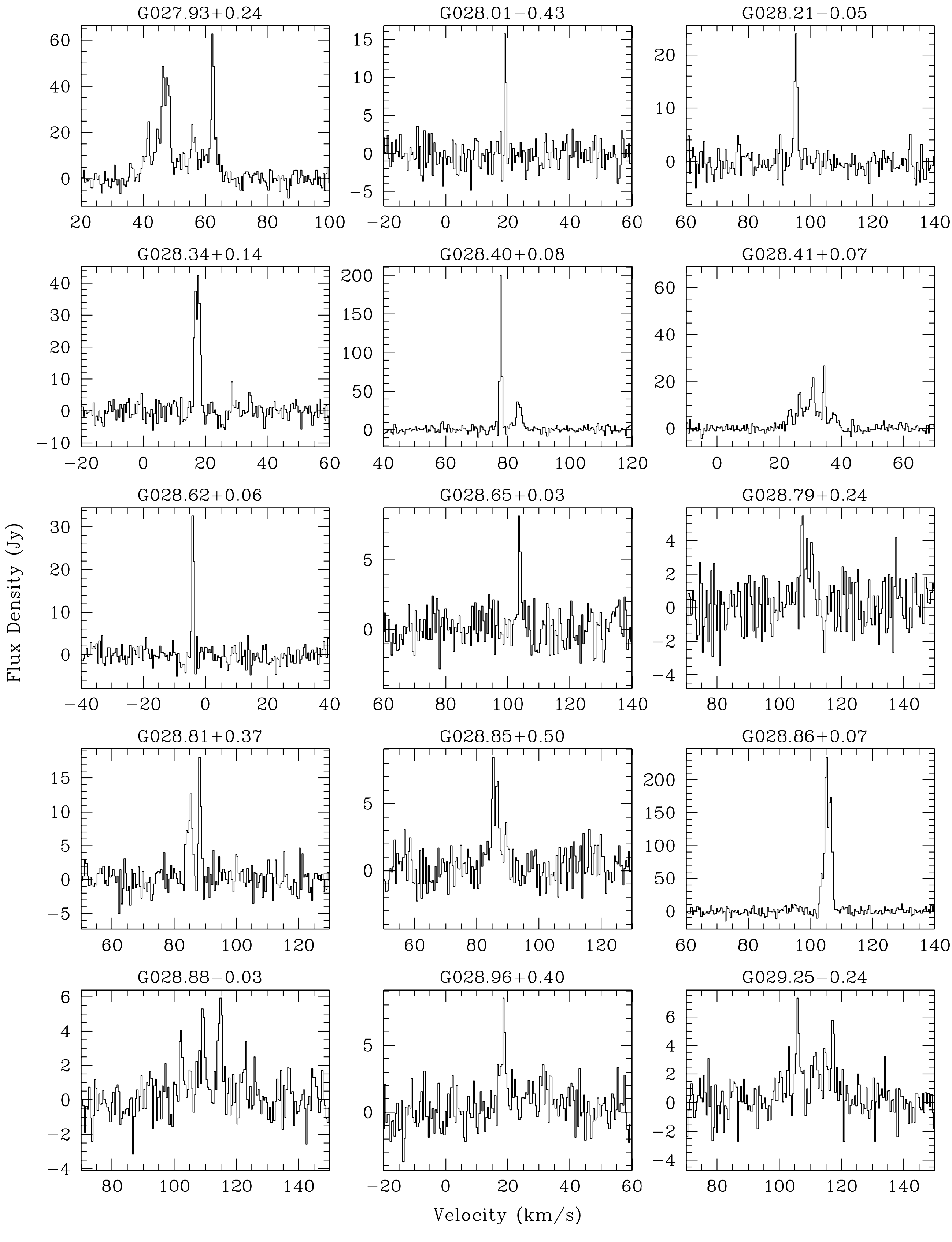

Figure 6 – *continued*

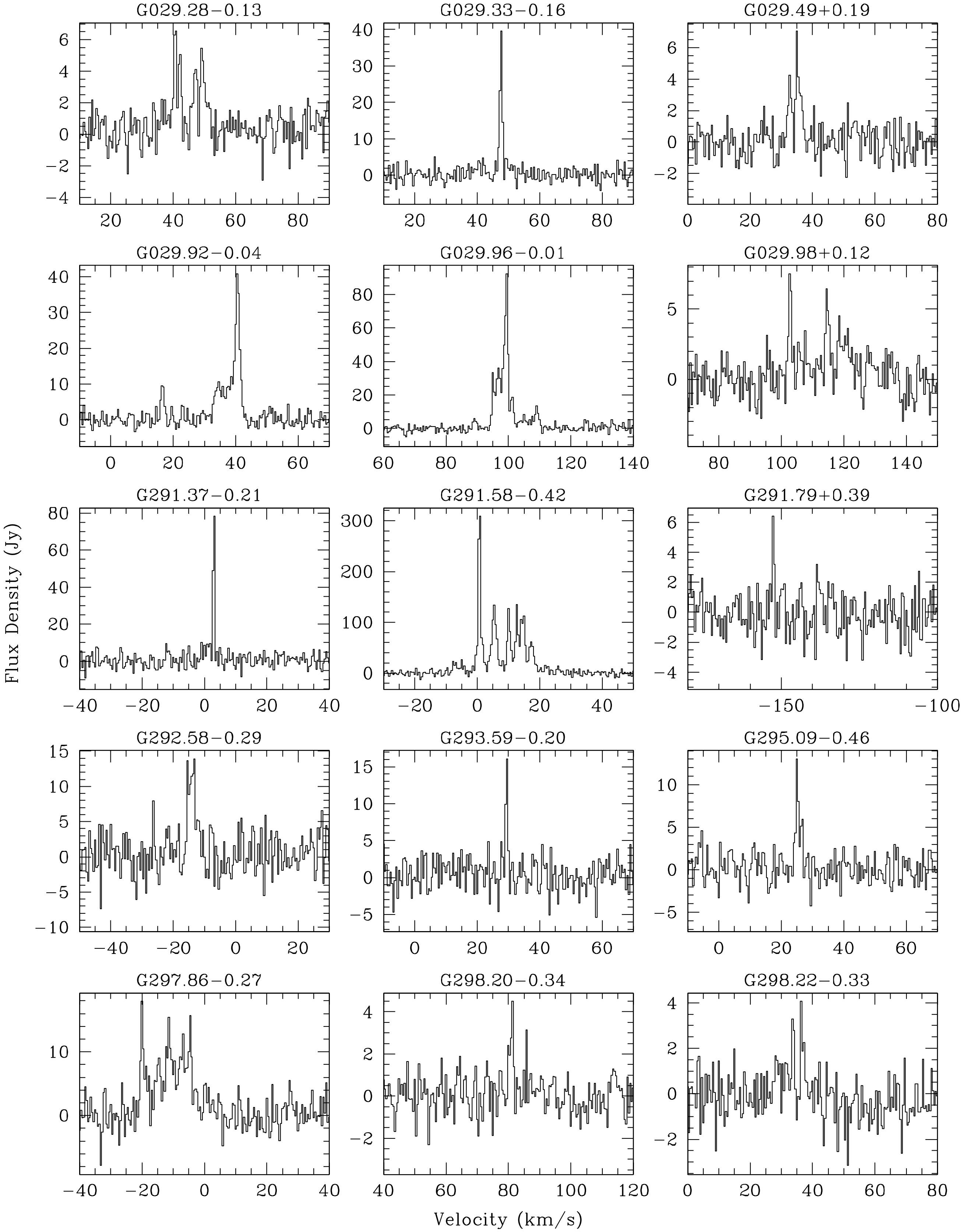

Figure 6 – *continued*

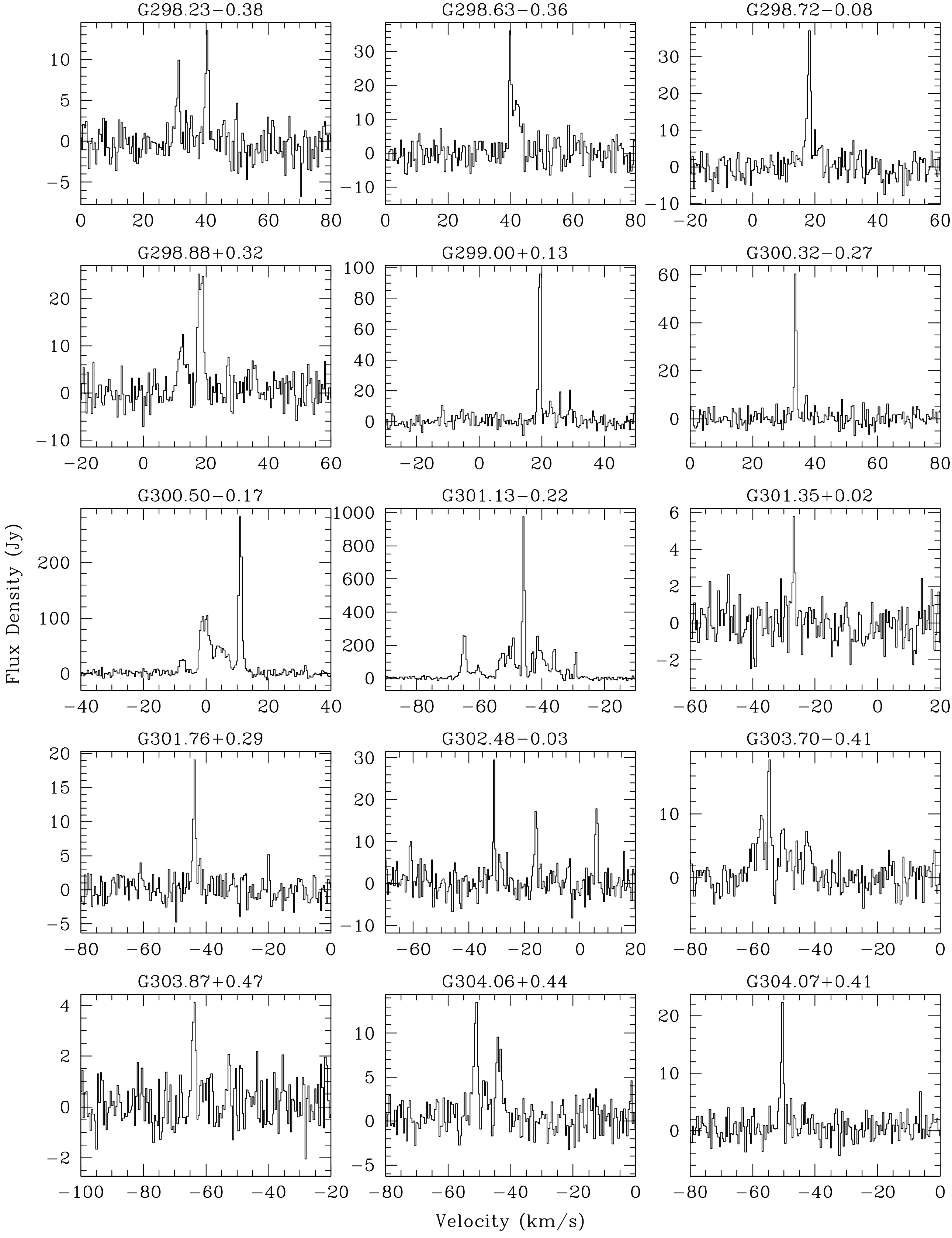

Figure 6 – *continued*

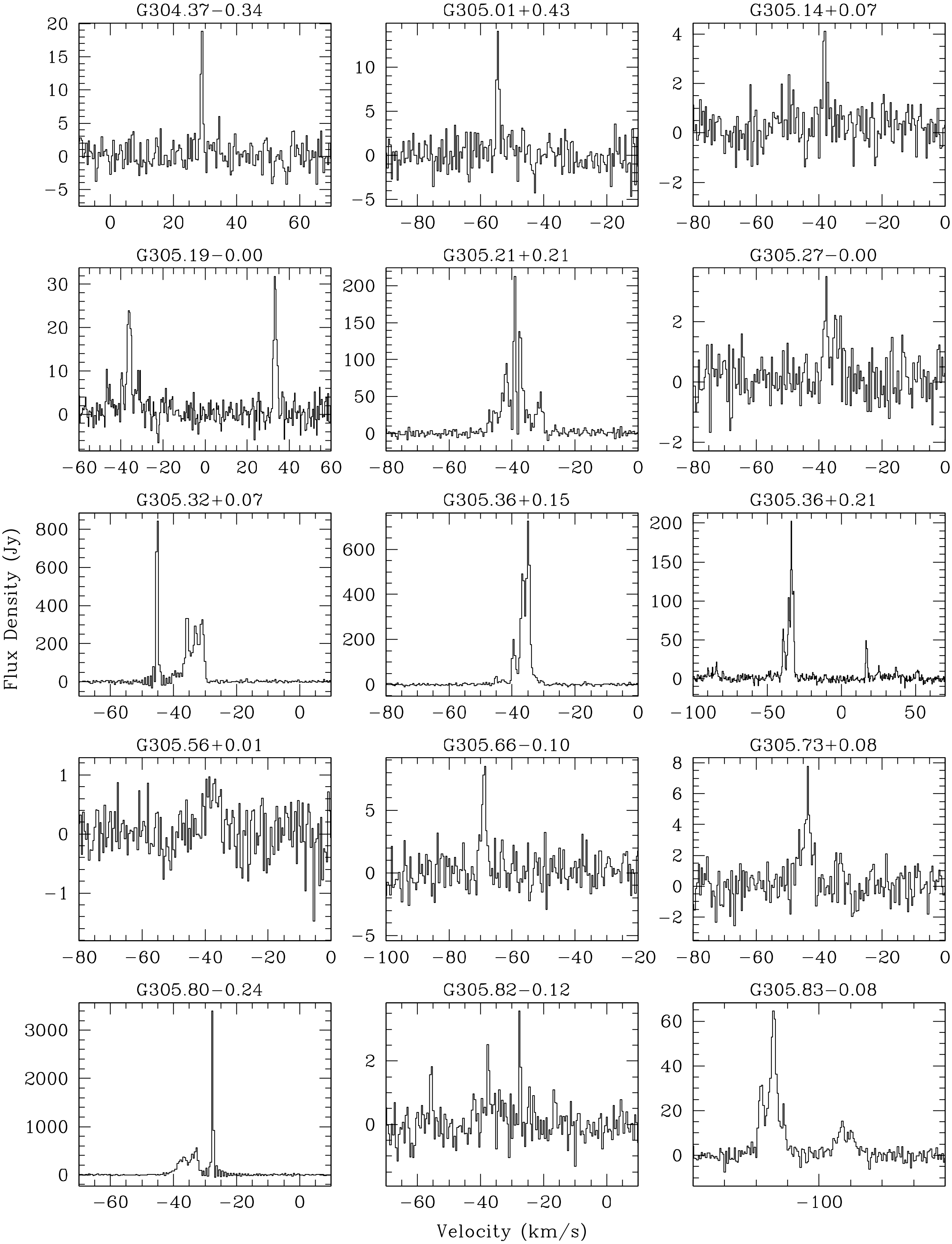

Figure 6 – *continued*

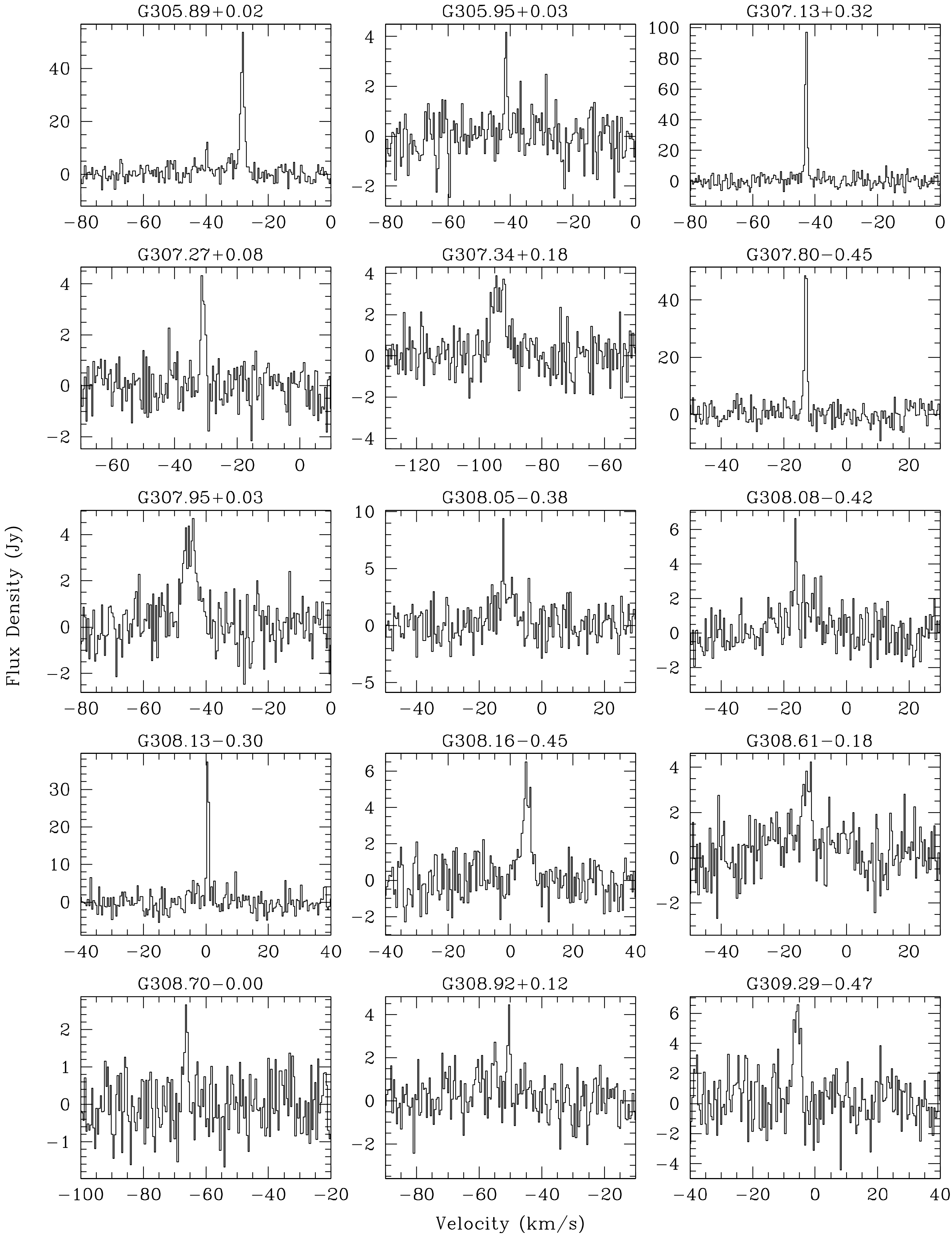

Figure 6 – *continued*

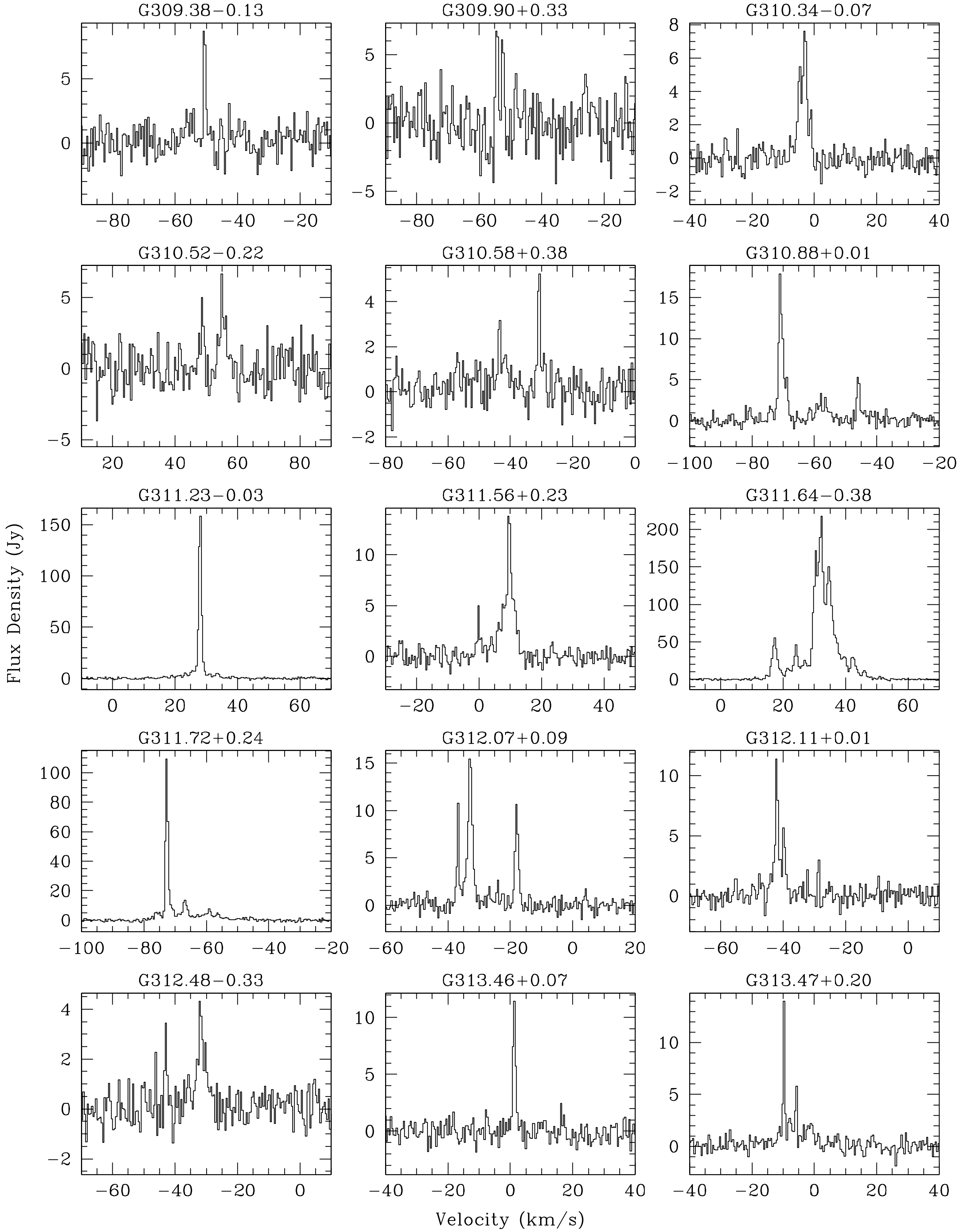

Figure 6 – *continued*

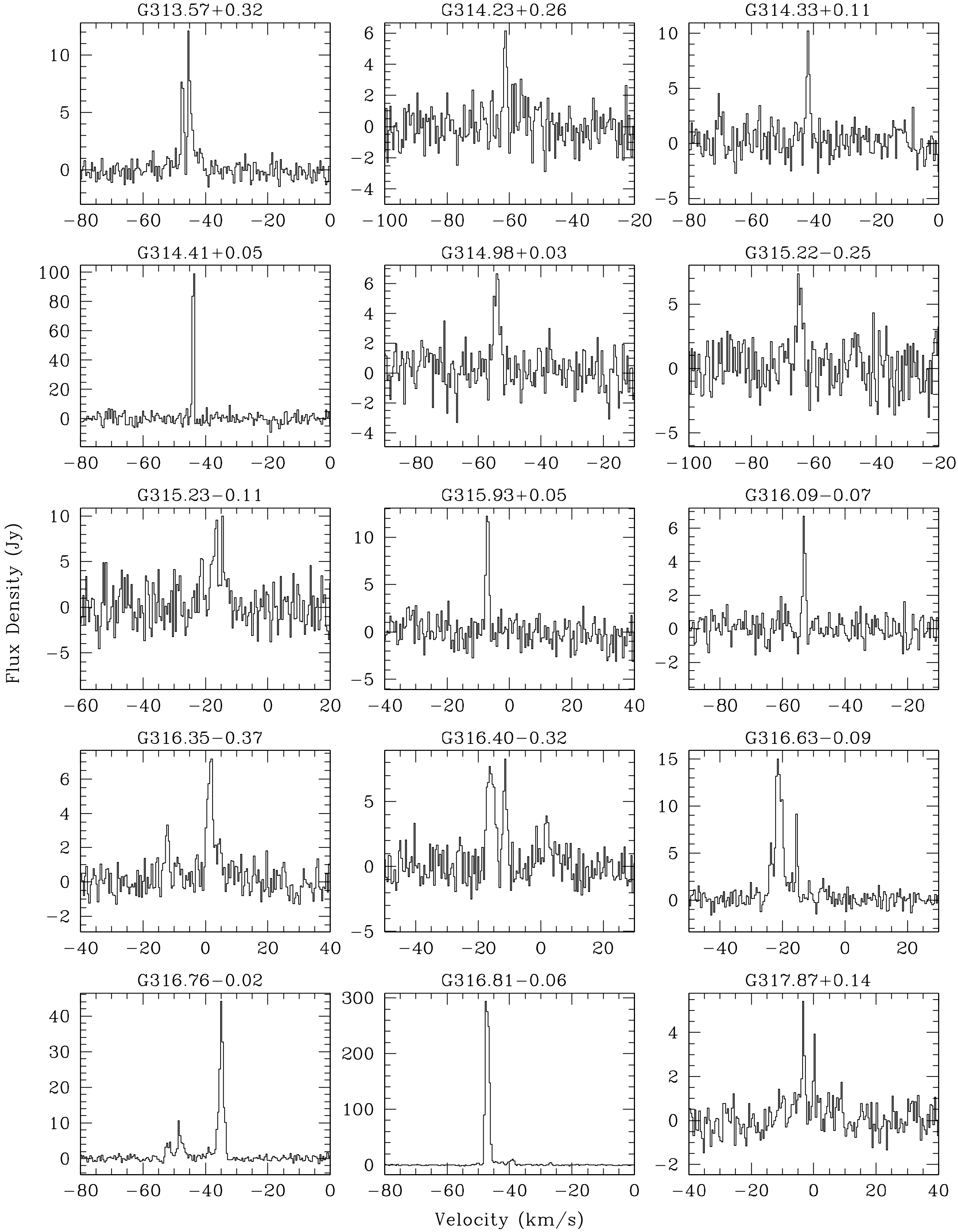

Figure 6 – *continued*

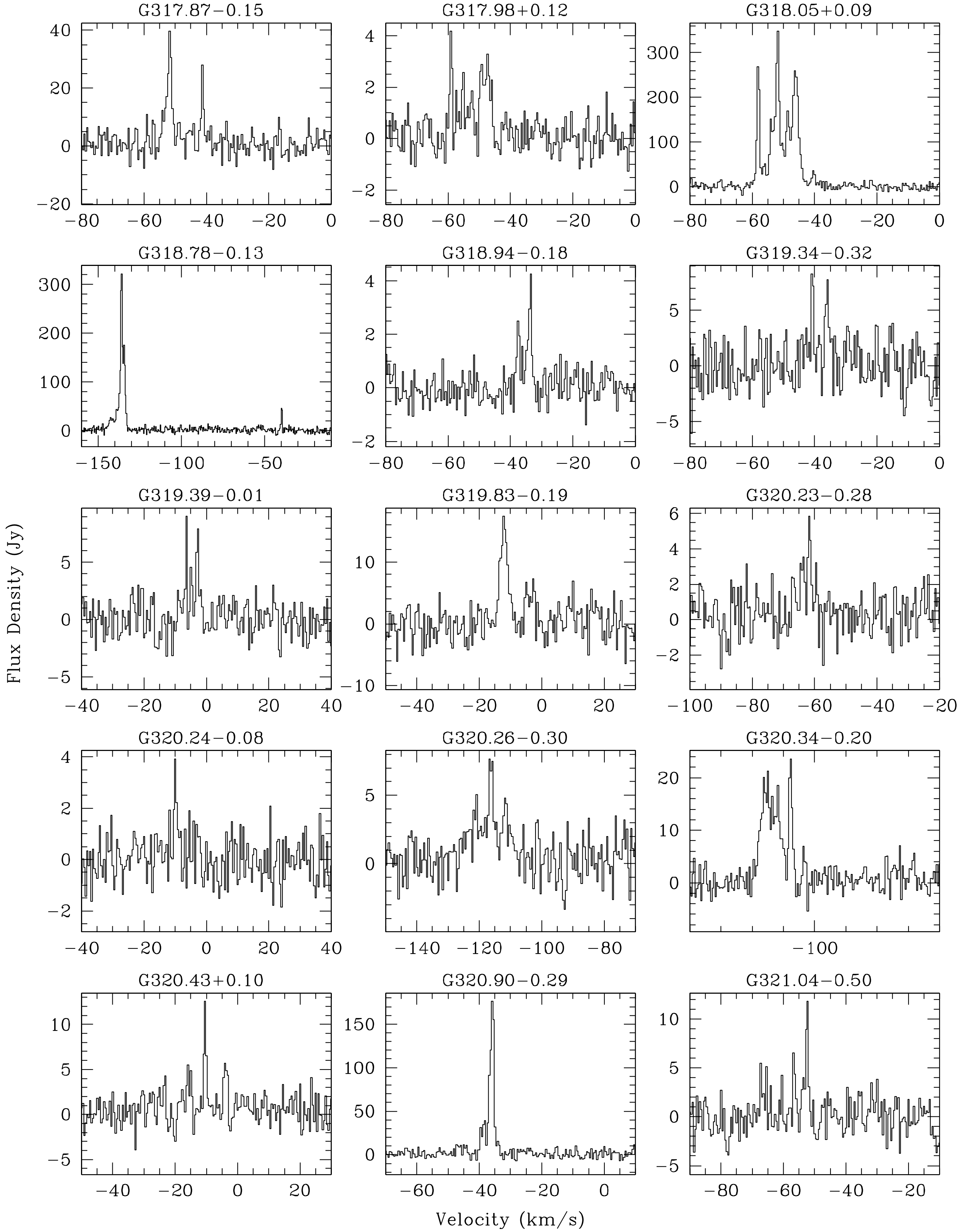

Figure 6 – *continued*

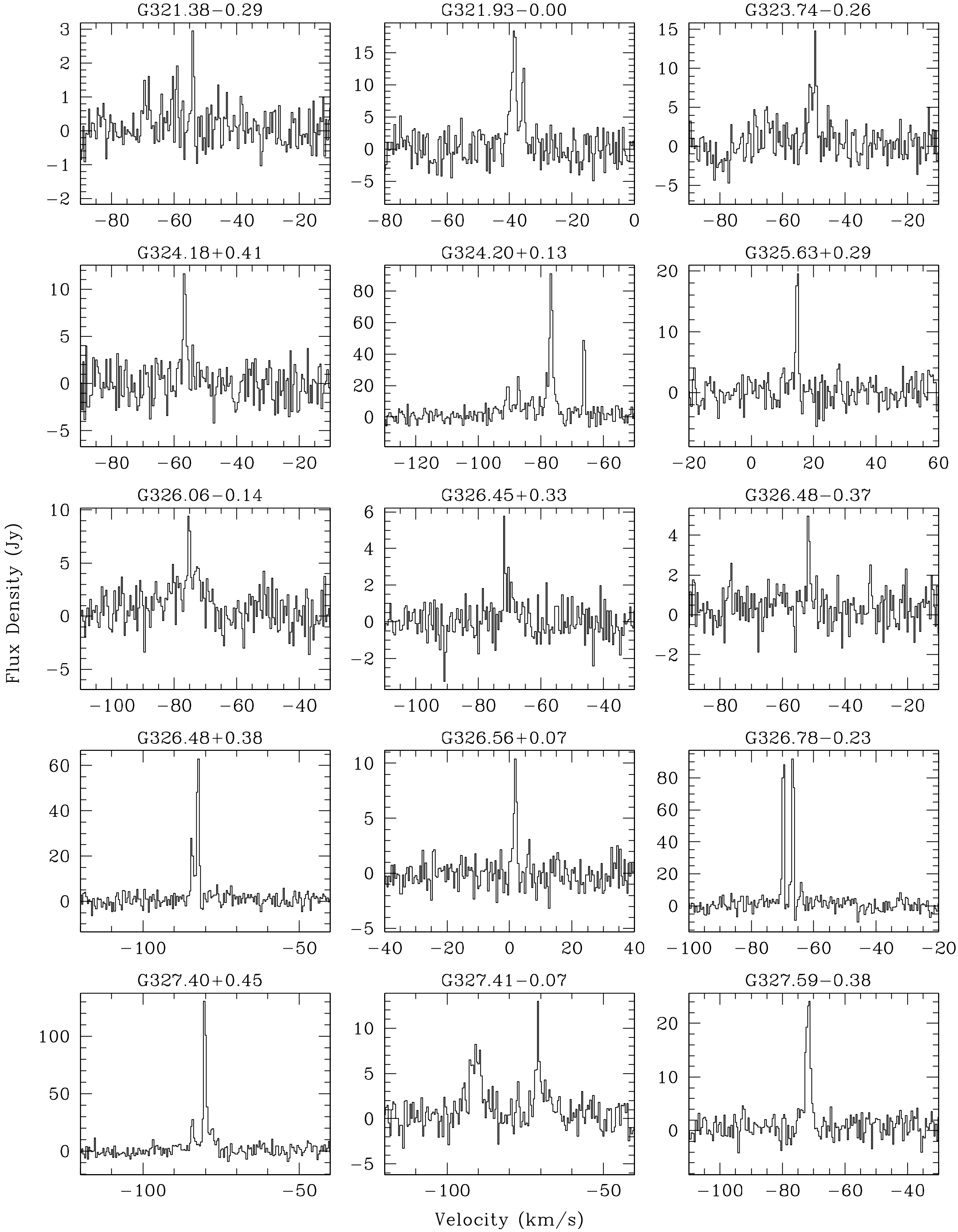

Figure 6 – *continued*

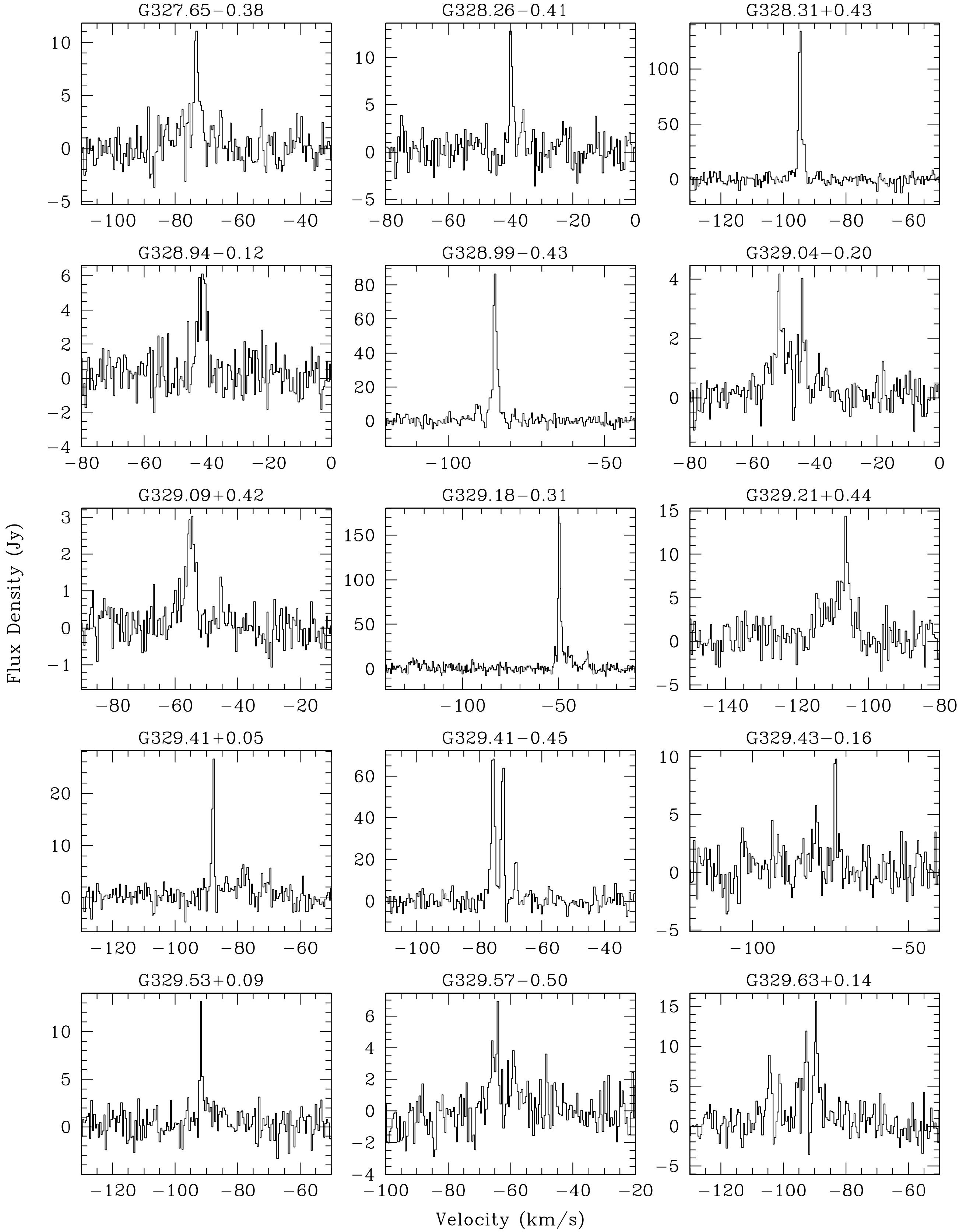

Figure 6 – *continued*

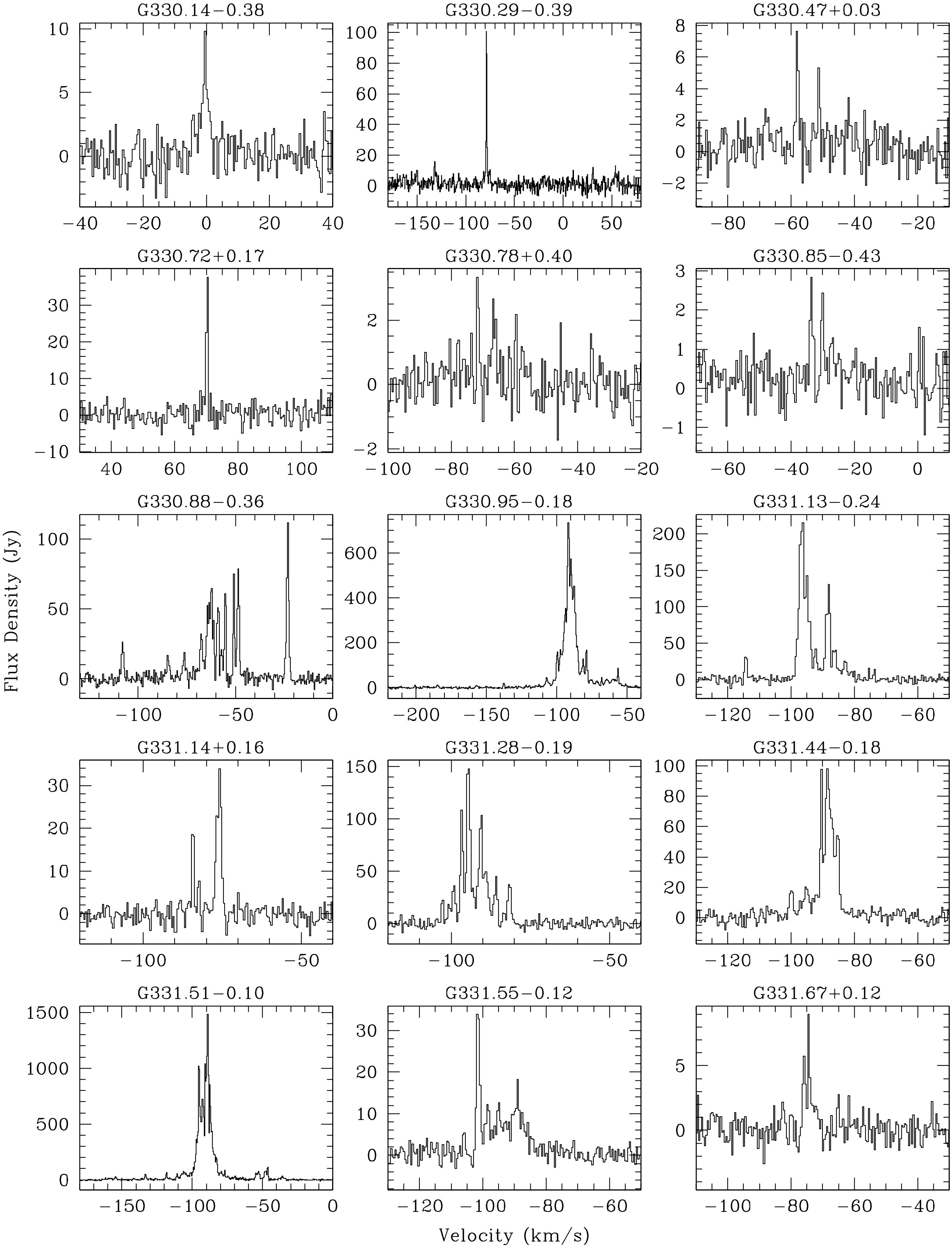

Figure 6 – *continued*

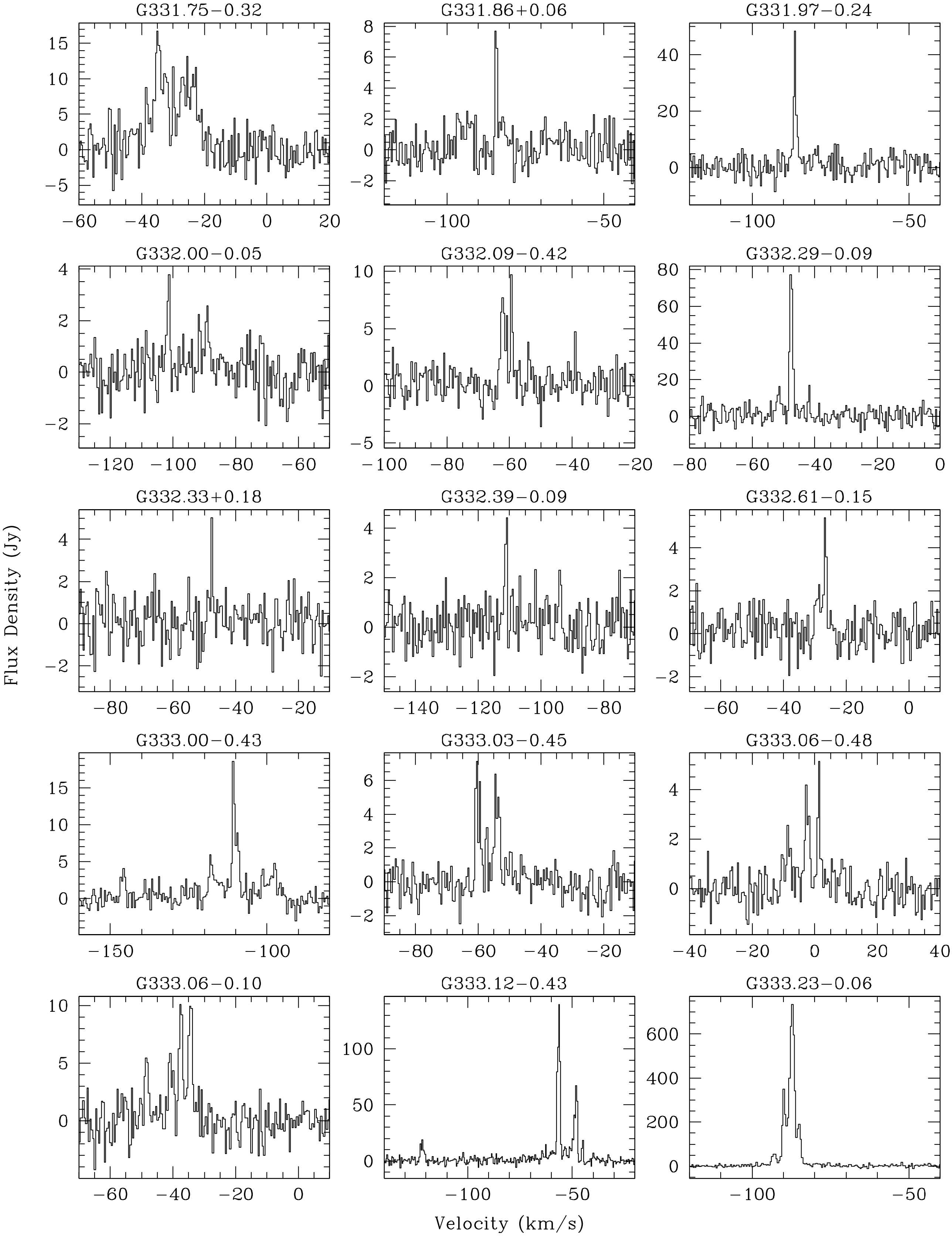

Figure 6 – *continued*

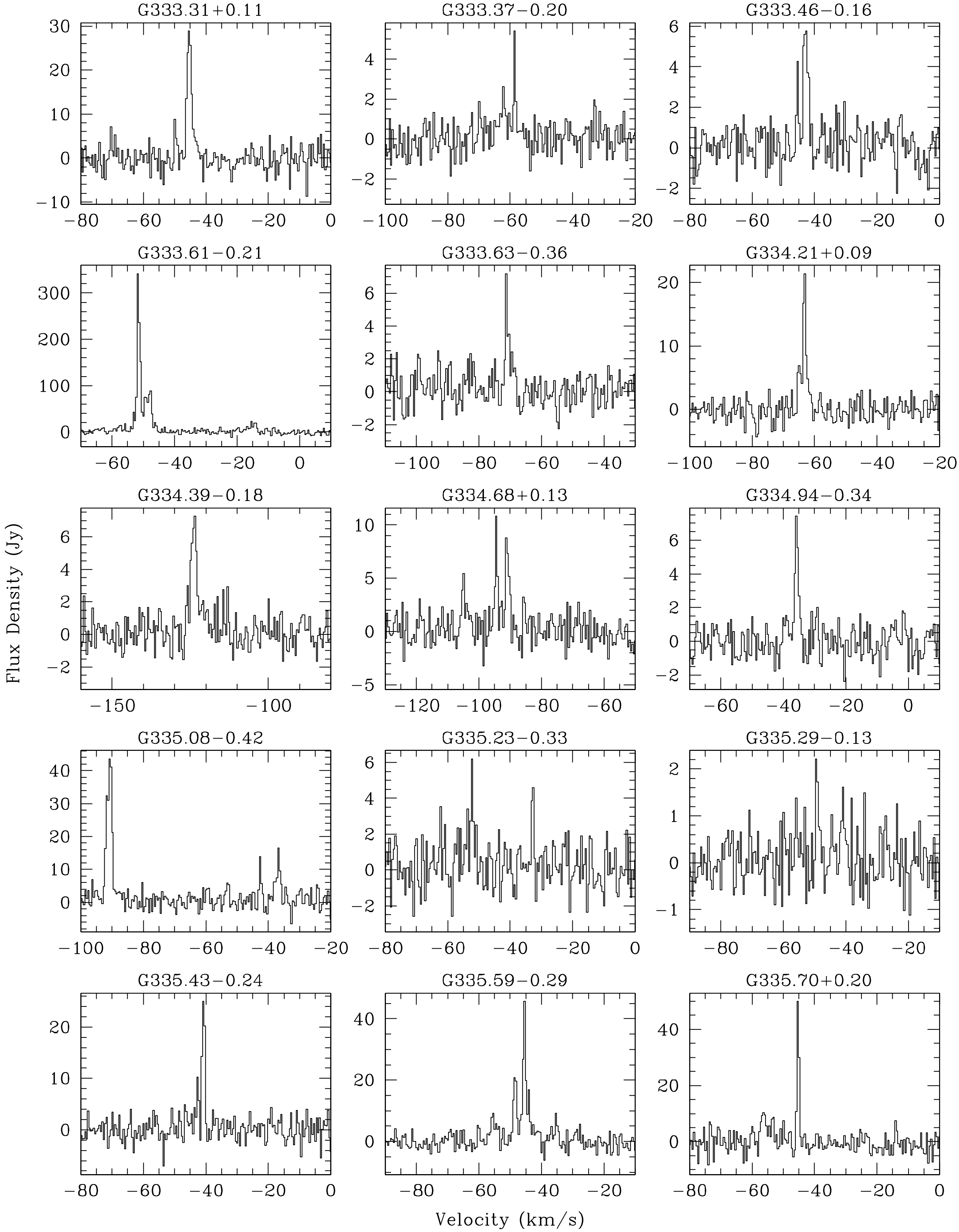

Figure 6 – *continued*

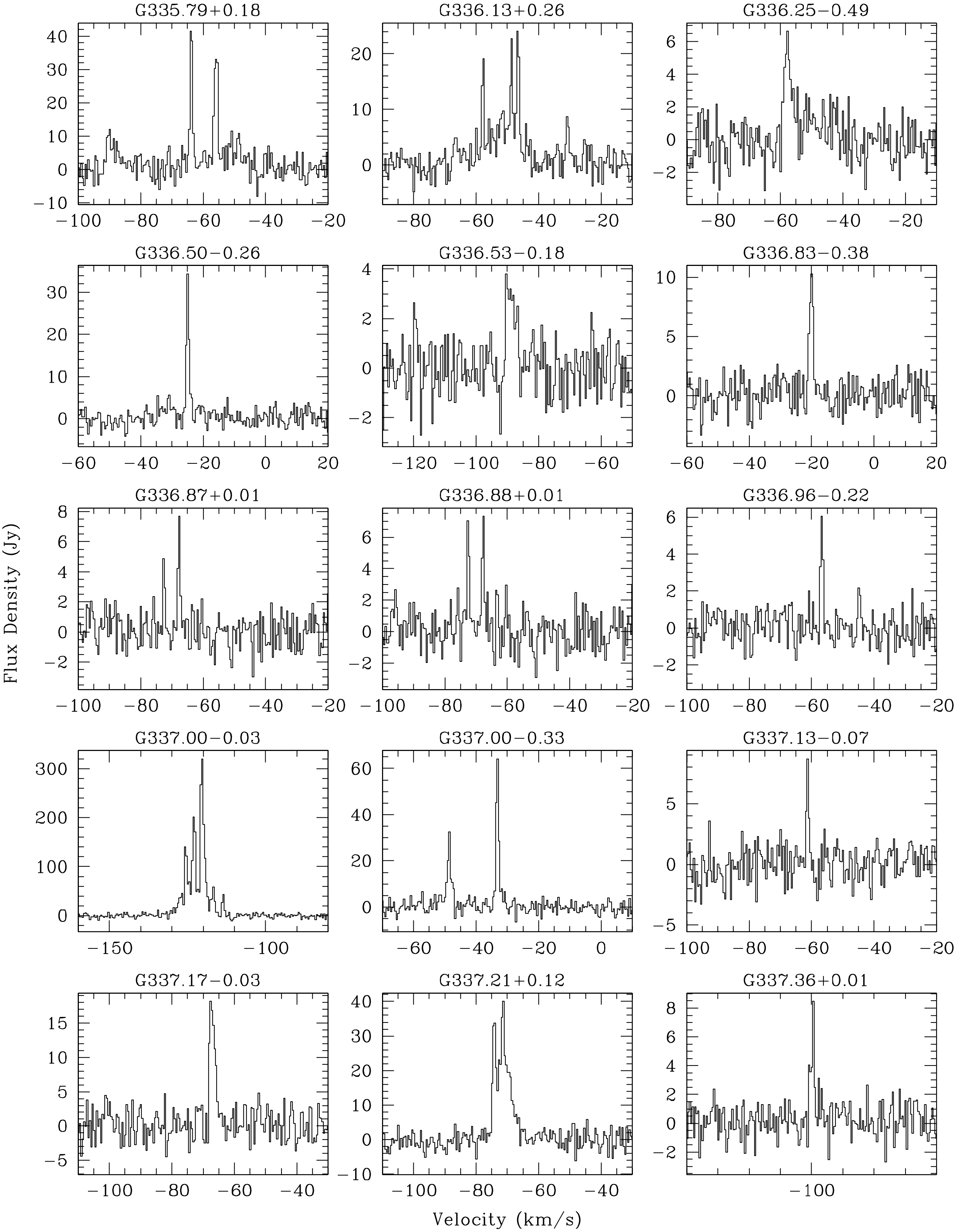

Figure 6 – *continued*

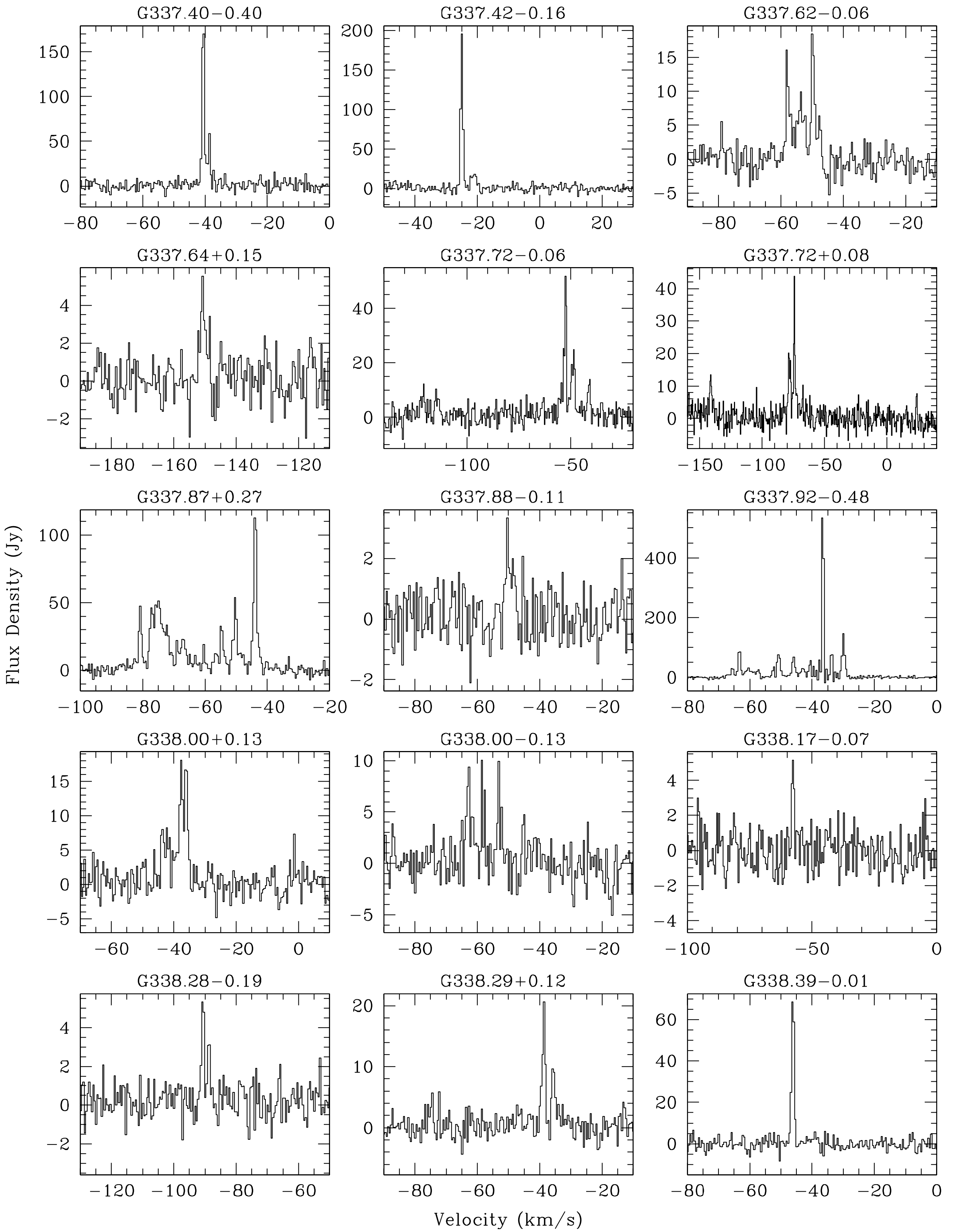

Figure 6 – *continued*

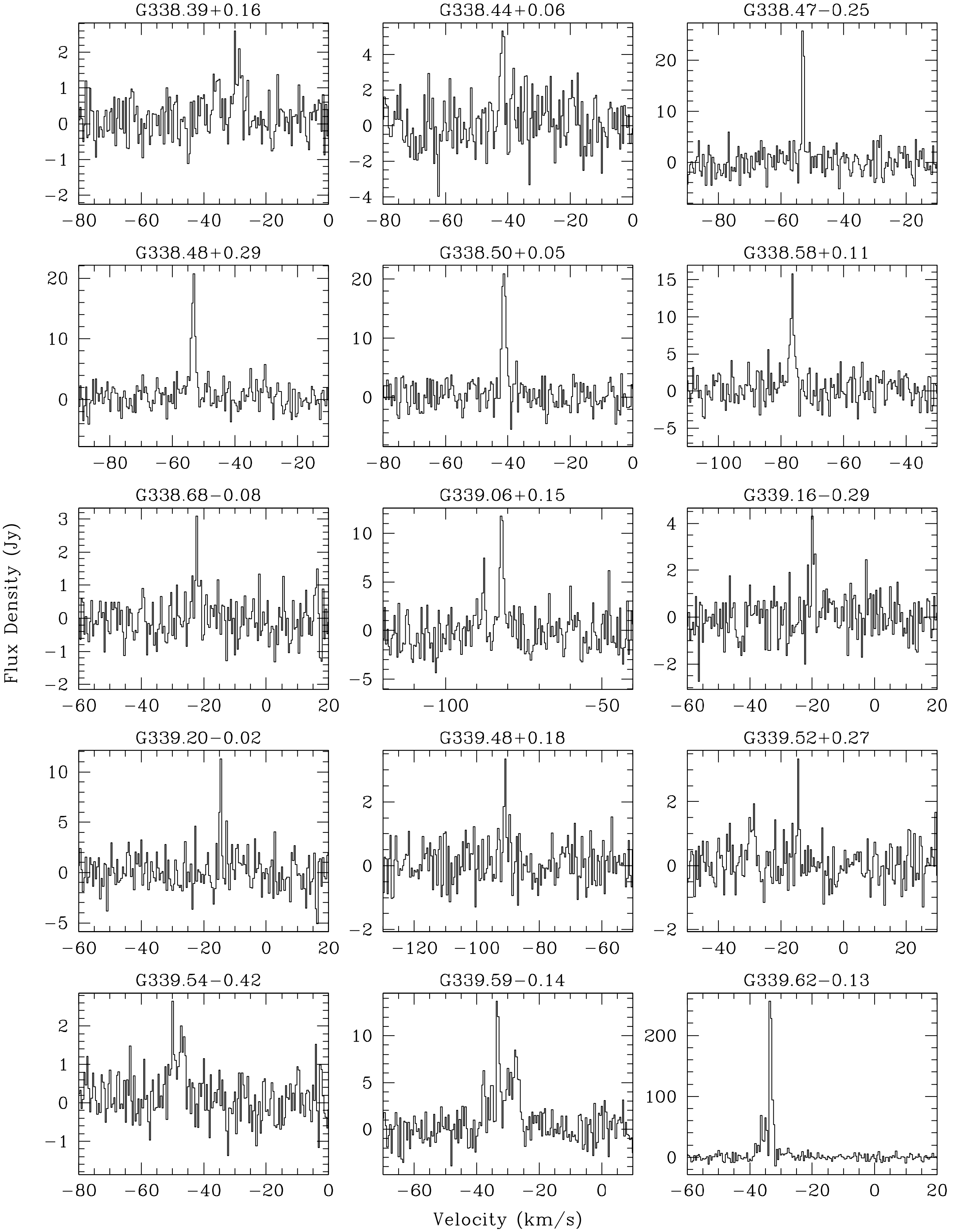

Figure 6 – *continued*

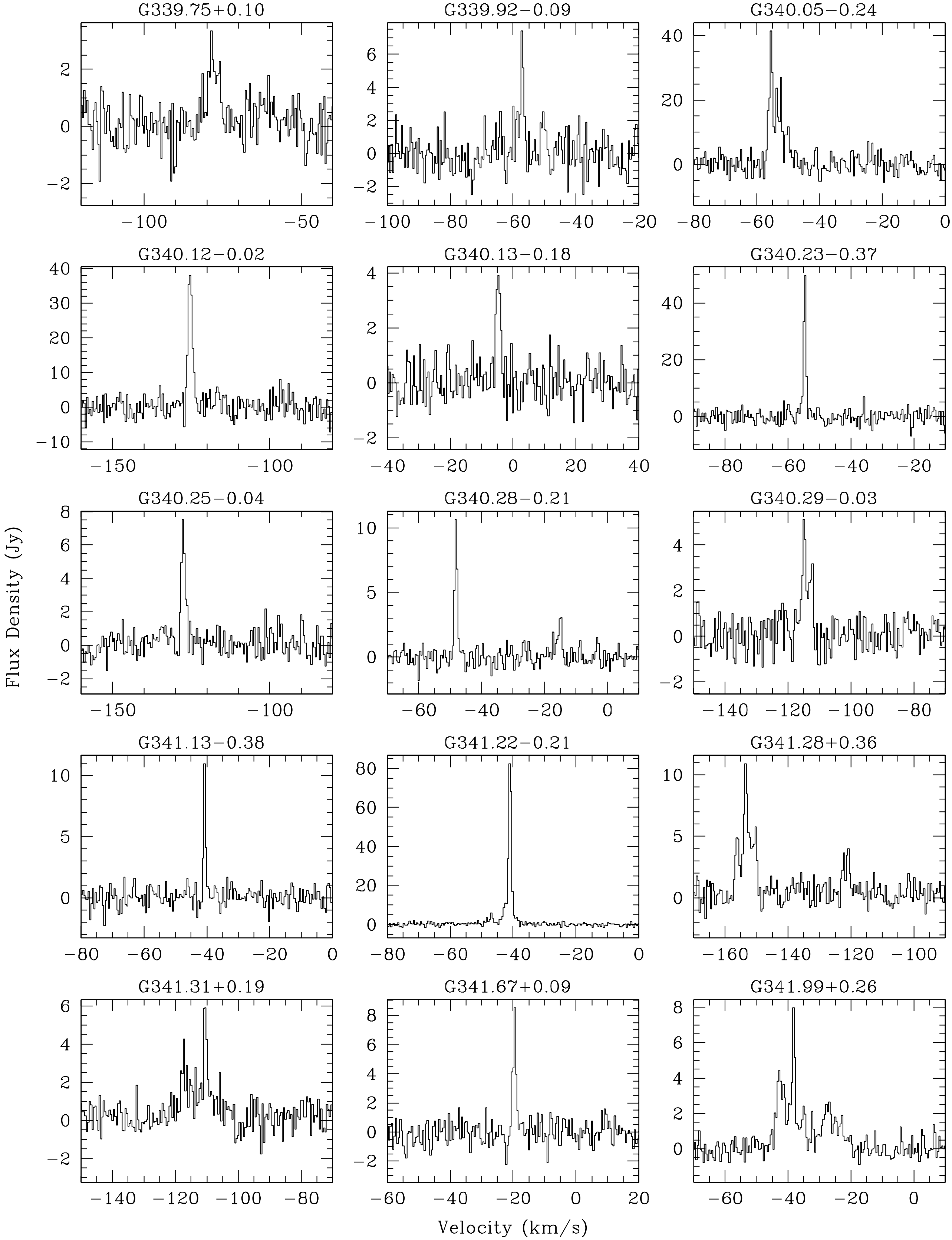

Figure 6 – *continued*

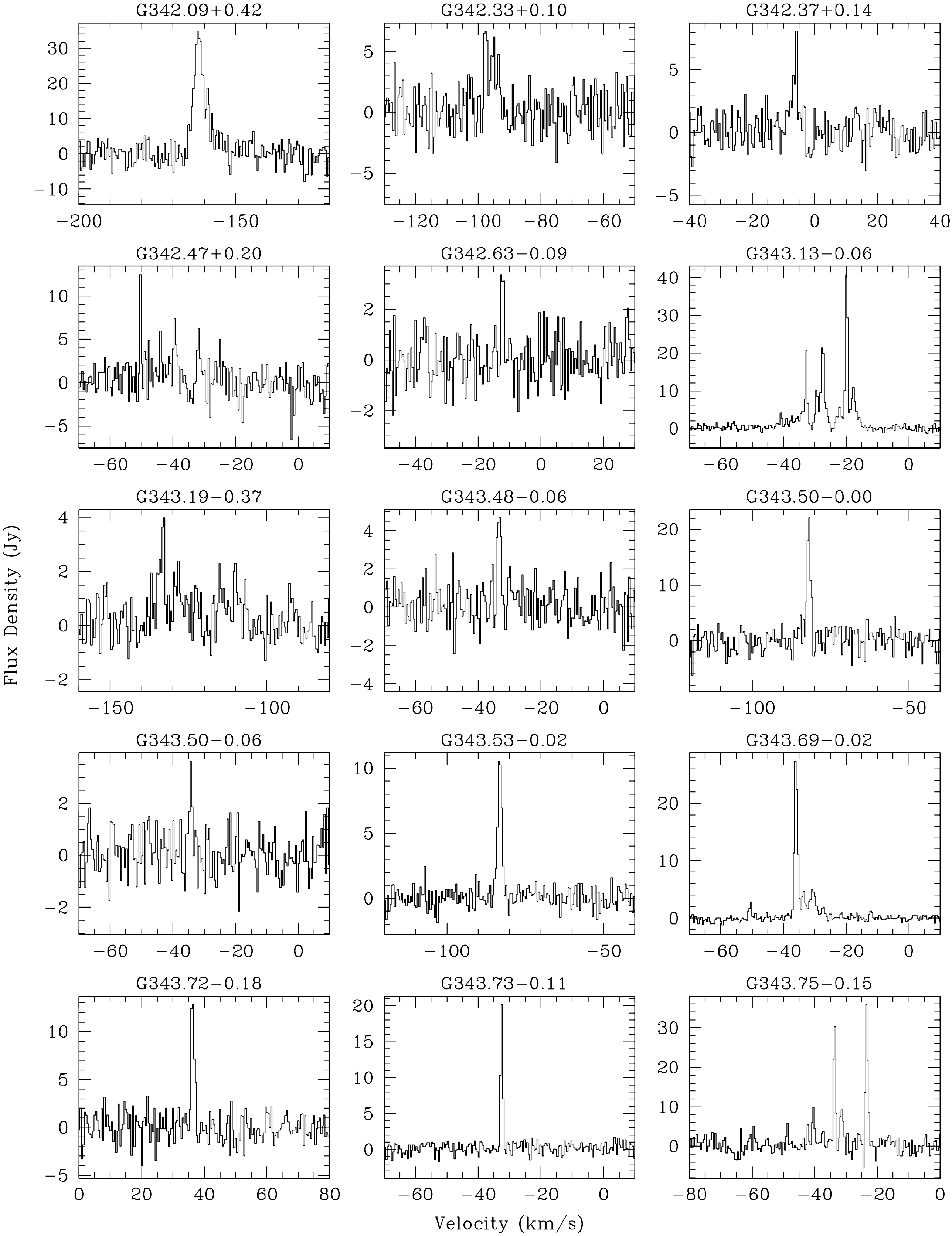

Figure 6 – *continued*

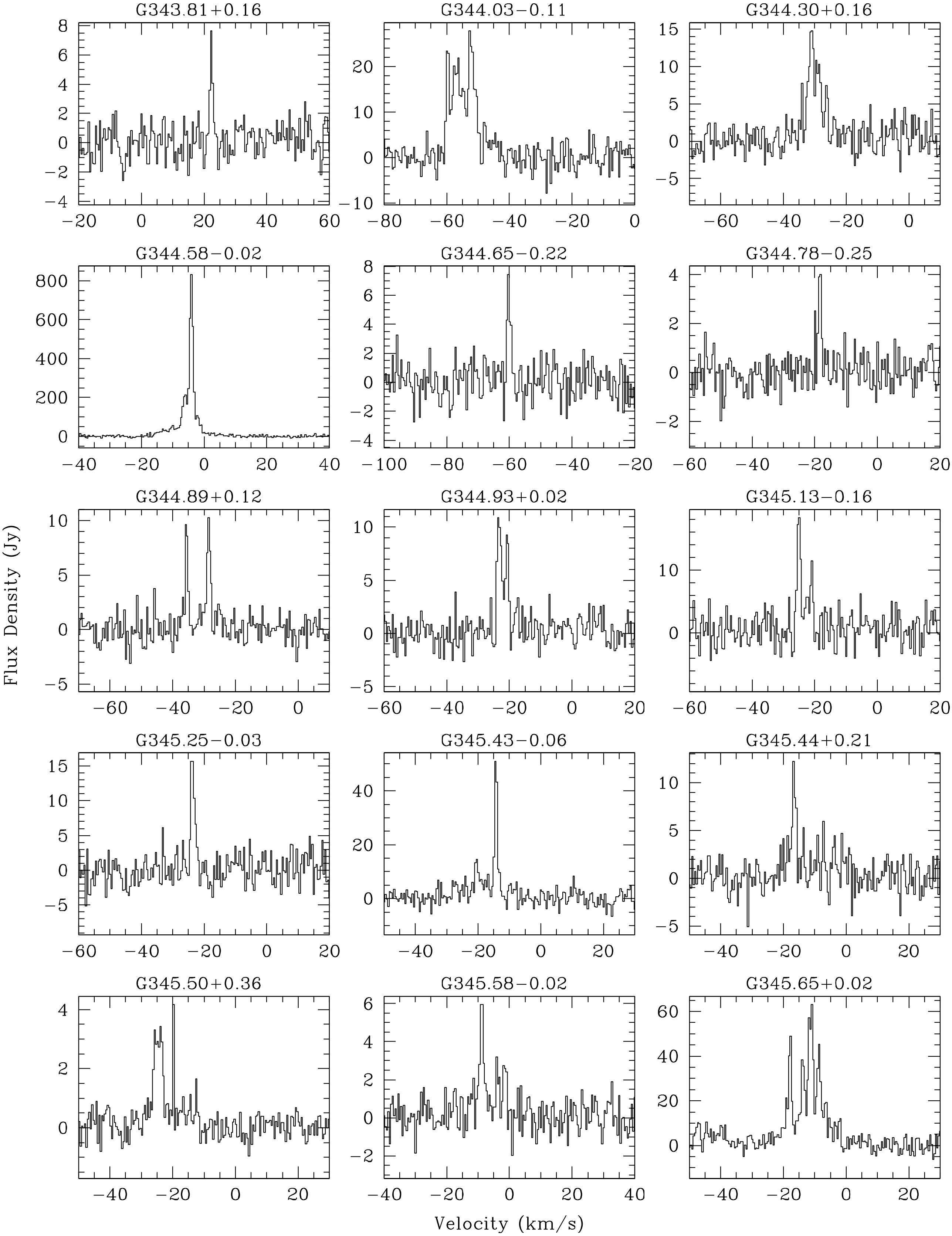

Figure 6 – *continued*

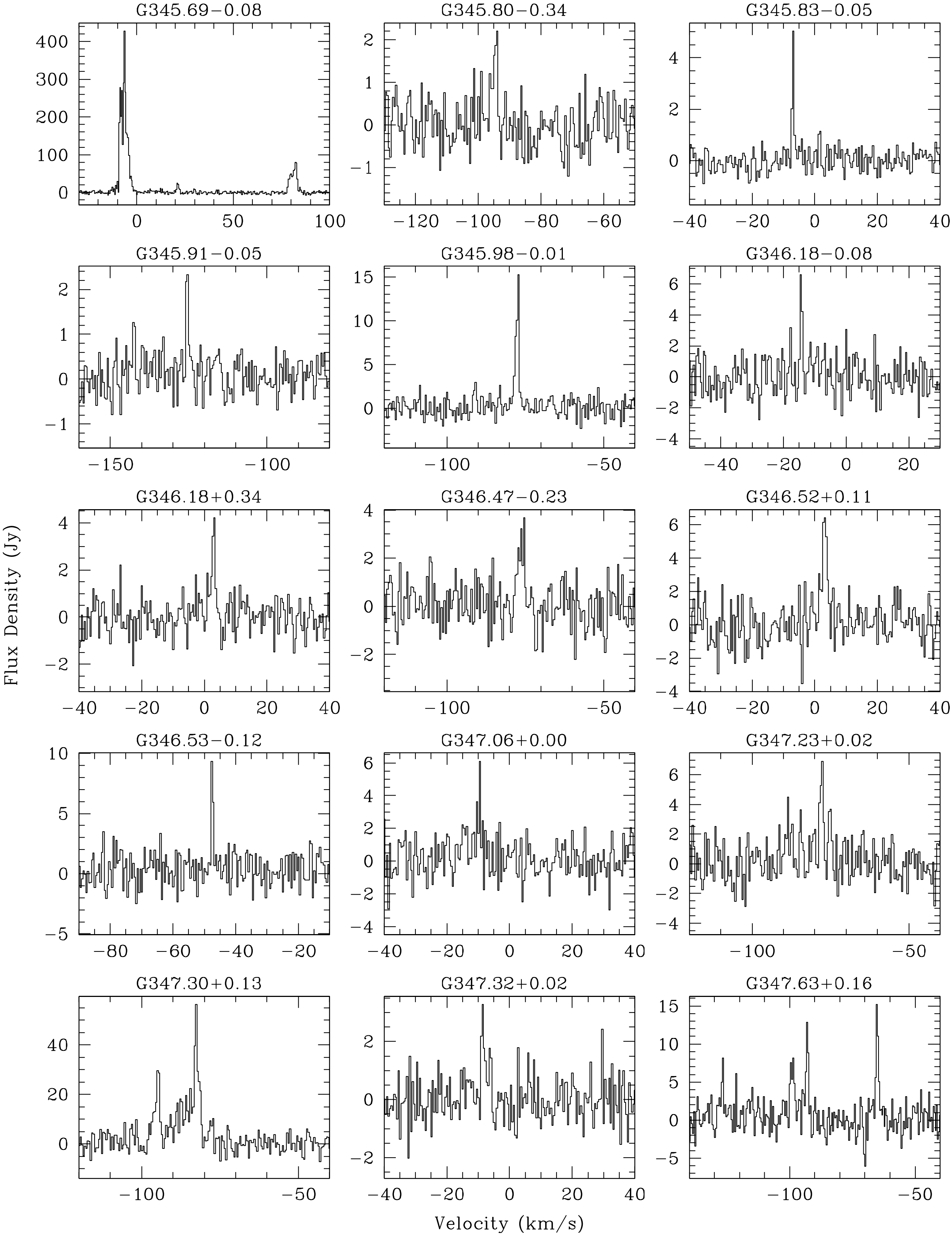

Figure 6 – *continued*

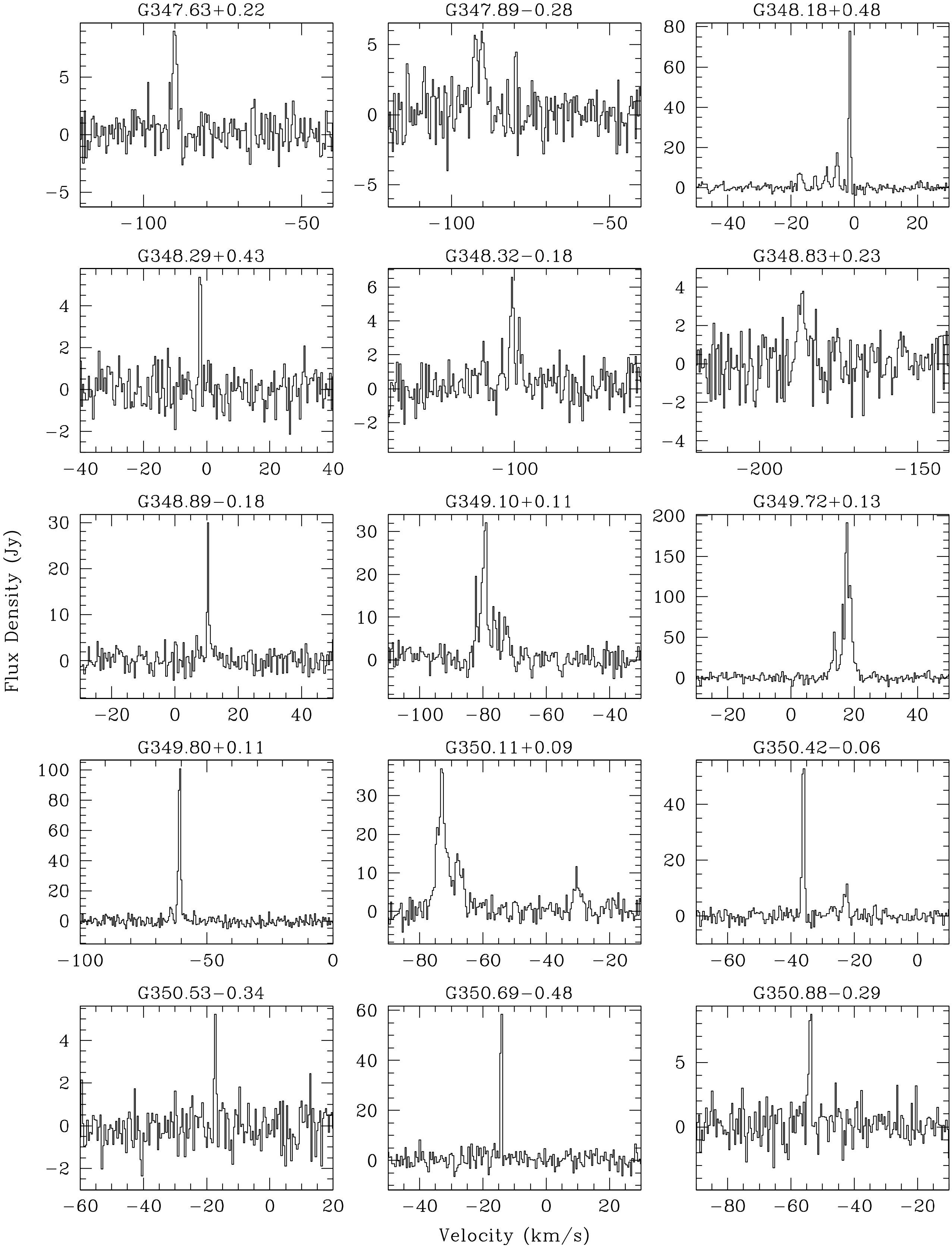

Figure 6 – *continued*

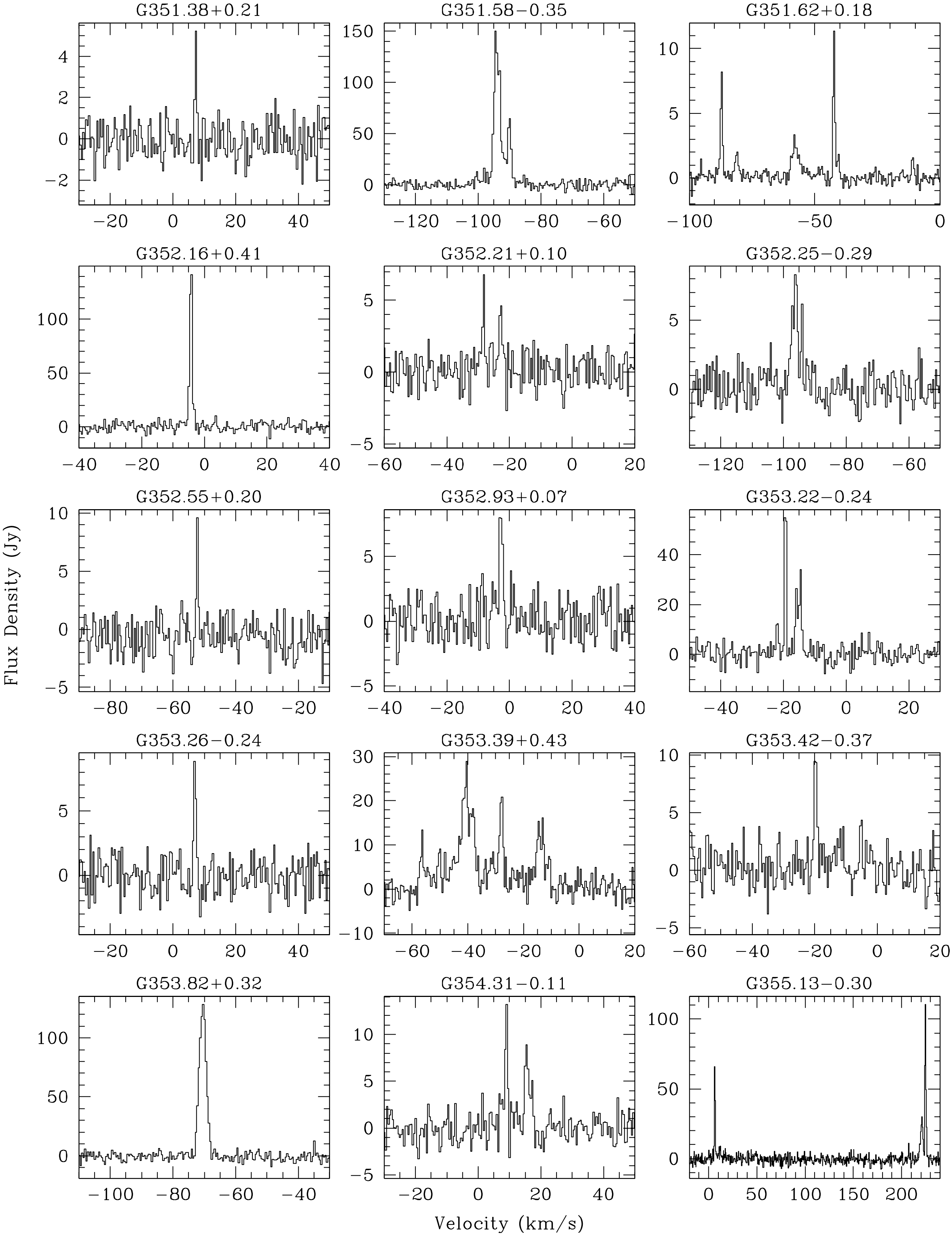

Figure 6 – *continued*

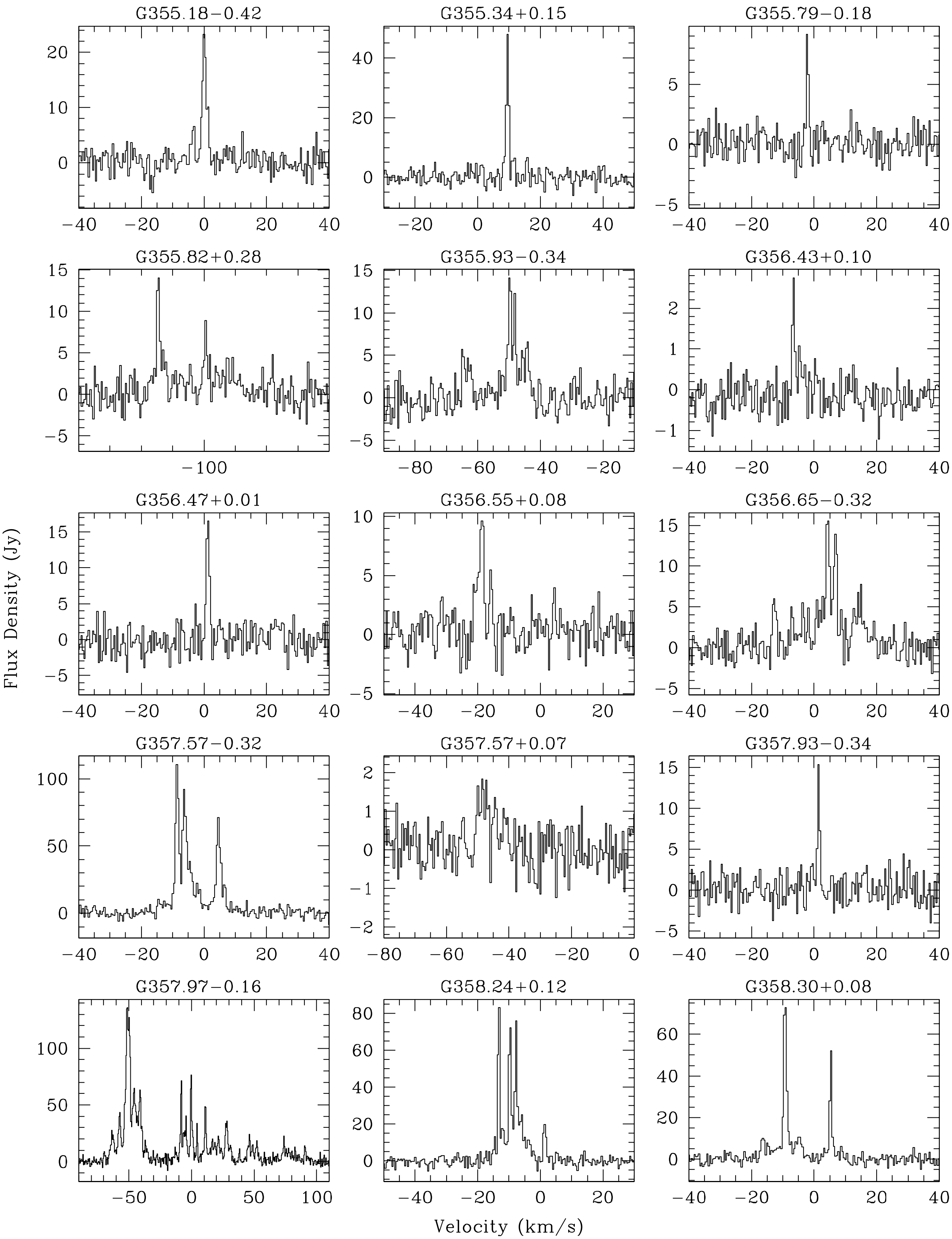

Figure 6 – *continued*

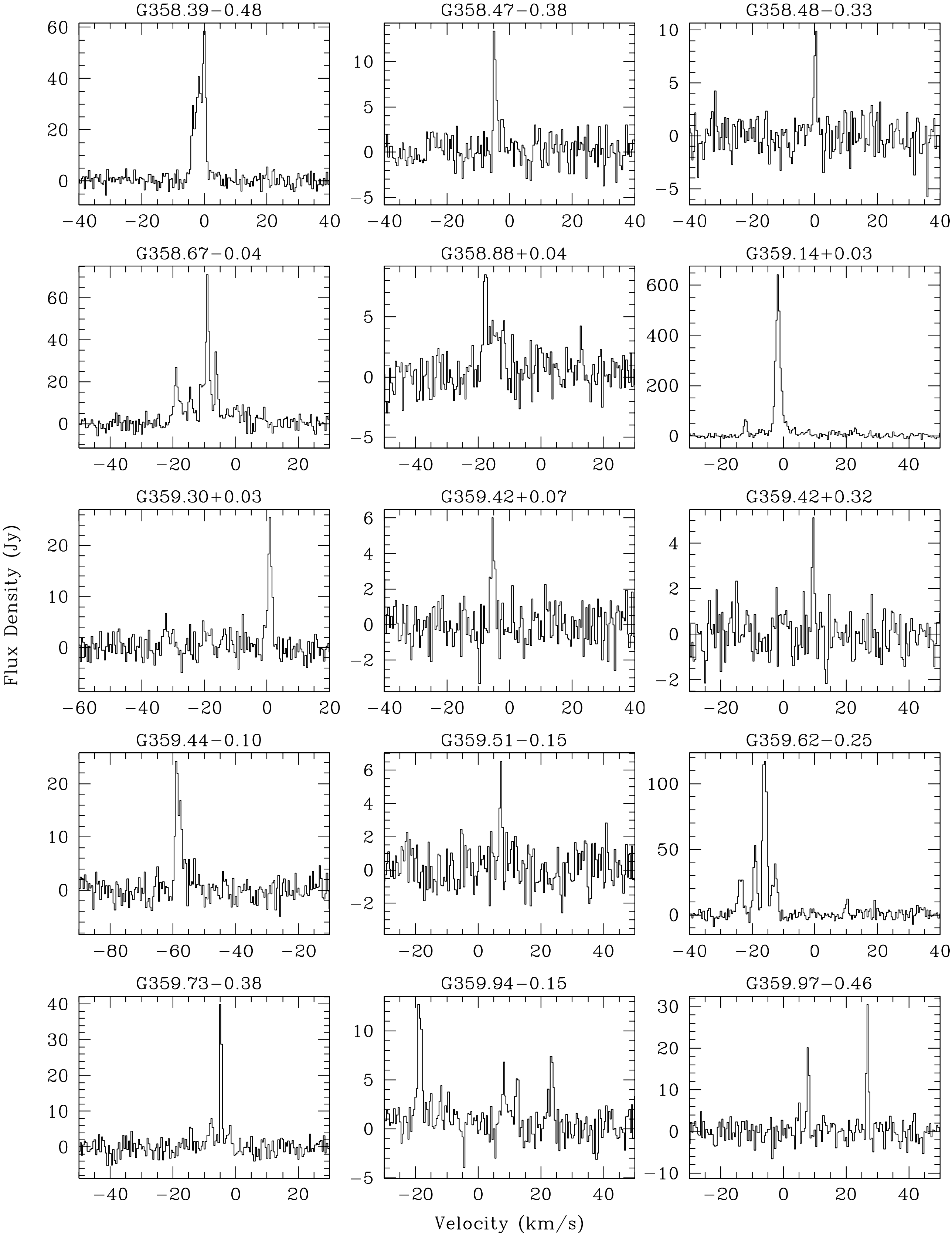

Figure 6 – *continued*

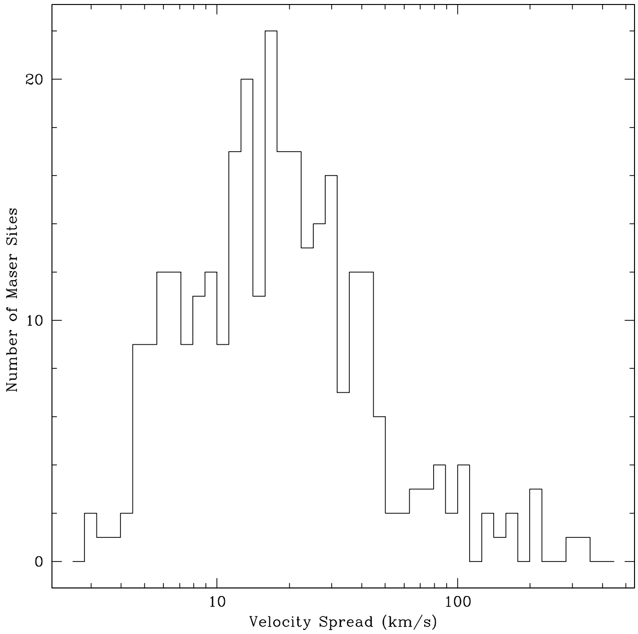

Figure 7. Distribution of H_2O maser velocity spreads for maser sites showing more than one maser spot. The majority of maser sites are confined to a velocity spread of less than 17 km s^{-1} and 90 per cent of maser sites have a velocity spread of less than 50 km s^{-1}.

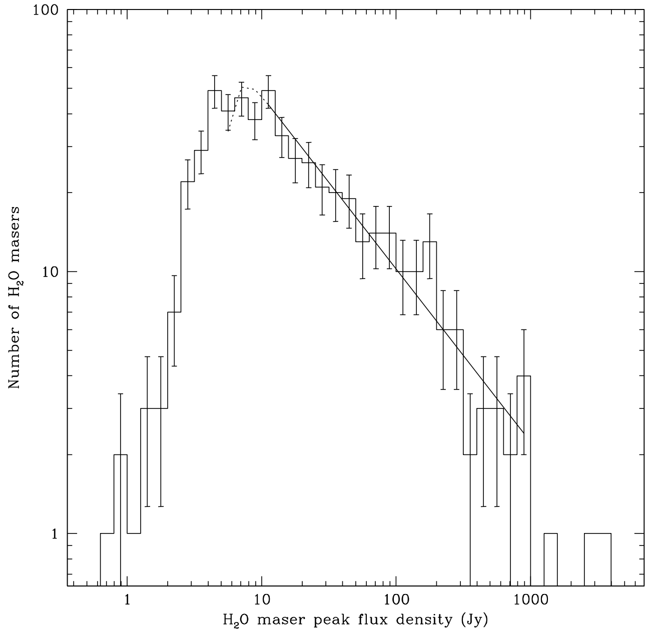

Figure 9. Distribution of H_2O maser peak flux densities, based on the strongest maser spot in each maser site. The histogram shows the distribution of detected masers, with error bars representing $\sqrt{N}$ statistics. The solid straight line is a power-law fit to the distribution above the 100 per cent completeness limit of 10 Jy, with slope −0.66. The dotted line represents the apparent turnover in the distribution due to the completeness limit. This dotted line is consistent with the histogram implying that we do not see a significant turnover in the population of H_2O maser flux densities.

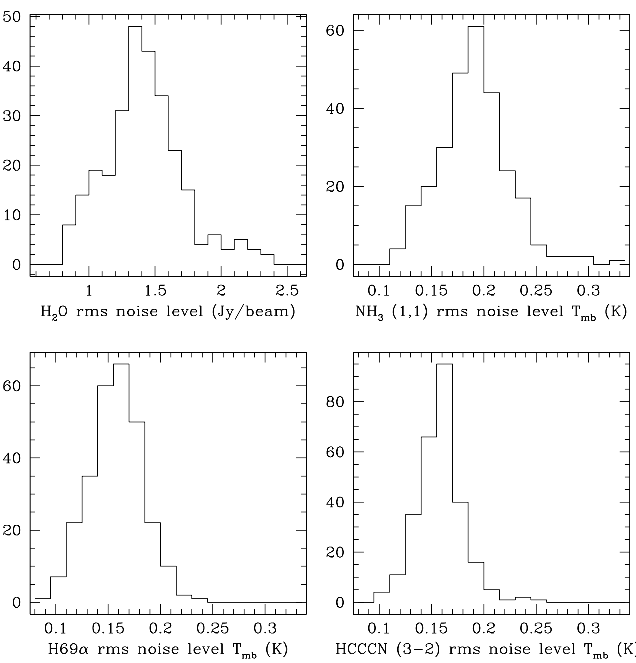

Figure 8. Histograms of rms noise levels. Top-left: H_2O maser noise levels in units of Jy beam^{-1}, assuming a conversion factor of 12.4 Jy K^{-1}. Top-right: NH_3 (1, 1) rms noise levels in units of main beam brightness temperature. Bottom-left: H69α radio recombination line rms noise levels in units of main beam brightness temperature. Bottom-right: HCCCN (3–2) rms noise levels in units of main beam brightness temperature.

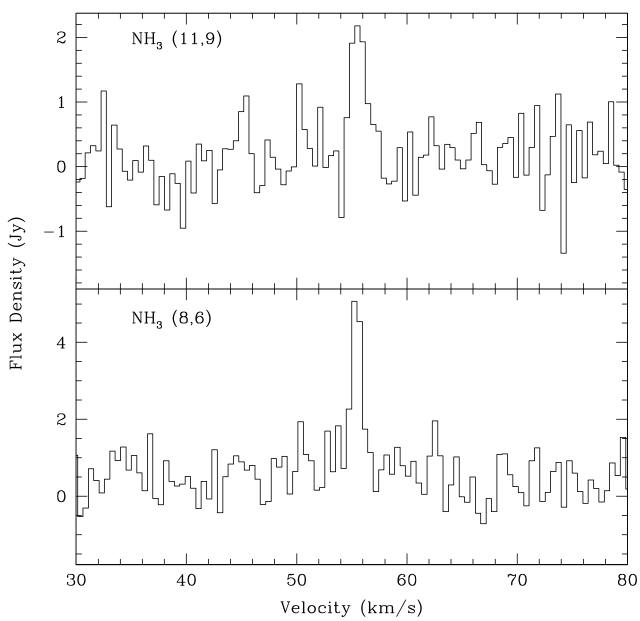

Figure 10. NH_3 emission spectra towards G19.61−0.23 in the (11, 9) inversion transition (top) and (8, 6) transition (bottom). Emission in the (11, 9) transition has a peak flux density of 2.2 Jy, line velocity of 55.6 km s^{-1} and line FWHM of 1.5 km s^{-1}. Emission in the (8, 6) transition has a peak flux density of 4.9 Jy, line velocity of 55.4 km s^{-1} and line FWHM of 1.1 km s^{-1}.

This suggests that G19.61−0.23 may be an unusual region of maser activity in the Galaxy; otherwise, we would expect to detect other maser sites closer to us. Garay et al. (1998) concluded that in this region an ionization front is driven by an expanding H II region into a molecular cloud. Together with the presence of the rare 9.9 GHz CH_3OH maser, which is known to trace strong shocks, it is possible that the NH_3 masers are created in the shock interface between the H II region and molecular cloud.

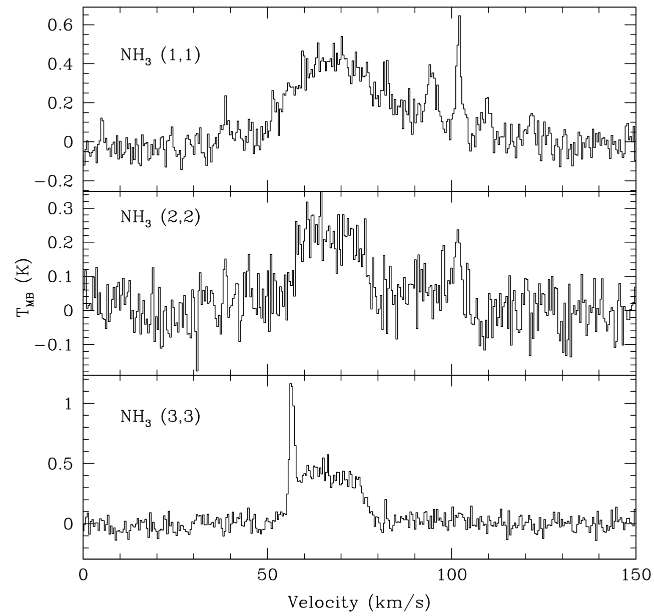

Figure 11. NH_3 emission spectra towards G23.33−0.30. Top: NH_3 (1, 1) emission showing a broad peak centred at approximately 70 km s^{-1} and a line FWHM of approximately 40 km s^{-1}. There is a second NH_3 (1, 1) source centred at approximately 102 km s^{-1}, with a line FWHM of 1.9 km s^{-1}. The second source also exhibits a hyperfine structure. Middle: NH_3 (2, 2) emission also showing the two features identified in the (1, 1) spectrum at a somewhat weaker level. Bottom: NH_3 (3, 3) emission showing a broad emission feature, as for the (1, 1) and (2, 2) spectra, with the peak around 64 km s^{-1} and line FWHM approximately 20 km s^{-1}. A new narrow-lined feature is seen in the (3, 3) spectrum at 56.7 km s^{-1}, with a linewidth of 1.2 km s^{-1}. This feature is suspected to be a maser.

7.3.2 NH_3 (3, 3)

We find widespread thermal NH_3 (3, 3) emission throughout the HOPS region. However, here we report on the possible detection of a maser in this transition. The possible maser is located at G23.33−0.30. The spectra of NH_3 (1, 1), (2, 2) and (3, 3) emission at the position of G23.33−0.30 are shown in Fig. 11.

We suspect that the narrow-lined emission peak at 56.7 km s^{-1} is a maser because this feature is not seen in either of the (1, 1) or (2, 2) spectra. It also shows an unusually narrow-line FWHM of 1.2 km s^{-1}, i.e. much narrower than the typical (1, 1) and (2, 2) thermal linewidths (Longmore et al. 2007). We await further observations to confirm, or otherwise, the maser nature of this emission feature, as it is not possible to conclude given the current data. The NH_3 (3, 3) transition has previously been detected as a maser in DR 21(OH) (Mangum & Wooten 1994), W51 (Zhang & Ho 1995), NGC 6334 I (Kraemer & Jackson 1995) and G5.89−0.39 (Hunter et al. 2008). However, in all previous detections, the NH_3 (3, 3) maser has never been seen stronger than 0.5 Jy. Our observations of the suspected maser in G23.33−0.30 give a peak flux density of 9.7 Jy above the NH_3 (3, 3) thermal emission, which would make it the brightest NH_3 (3, 3) maser known by over an order of magnitude.

G23.33−0.30 is associated with an infrared dark cloud (Perettero & Fuller 2009) and cold dust continuum source (Di Francesco et al. 2008). It is also associated with a Class II CH_3OH maser (Szymczak, Hrynek & Kus 2000); however, the CH_3OH maser emission is seen over a velocity that ranges between 63 and 76 km s^{-1} and does not overlap with the suspected NH_3 (3, 3) maser. Based on the possible associations, the suspected NH_3 (3, 3) maser is likely to arise from a high-mass star-forming region, although the exact nature of any associations will almost certainly require higher spatial resolution observations to investigate the spatial coincidence of the NH_3 (3, 3) emission and other features in this region.

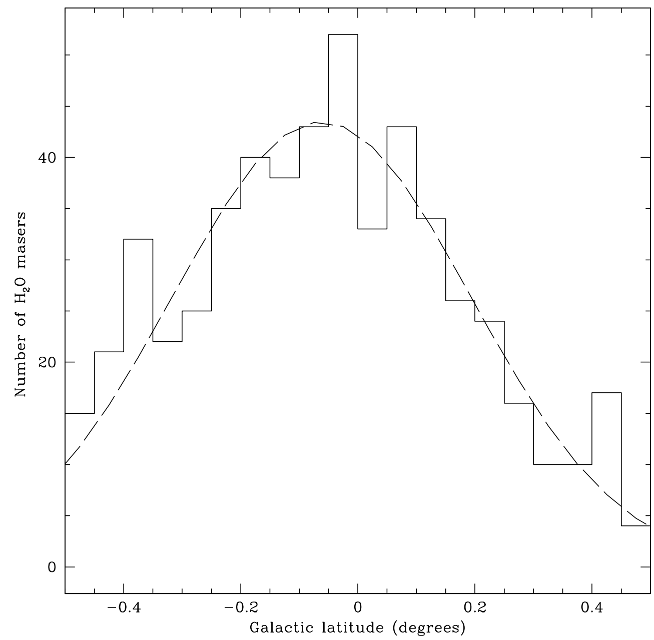

Figure 12. Galactic latitude distribution of H_2O masers detected in HOPS. The number of water masers is shown by the histogram and a fitted Gaussian to the distribution is shown as the dashed line. The fitted Gaussian has a peak at −0.062° and the FWHM of 0.60°.

7.4 H_2O maser Galactic latitude distribution

Fig. 12 shows the Galactic latitude distribution for water masers detected in HOPS. The dashed line in Fig. 12 shows a fitted Gaussian to the distribution, which has a peak at −0.062° and the FWHM of 0.60°. The FWHM corresponds to a scaleheight of 0.5°, which is slightly smaller than the scaleheight for UC HII regions of 0.6° (Wood & Churchwell 1989b) and slightly larger than the scaleheight found for Class II CH_3OH masers of 0.4° (Walsh et al. 1997). Both UC HII regions and Class II CH_3OH masers are reliable tracers of high-mass star formation and their scaleheight appears to be the smallest known for any class of Galactic object. Since the H_2O masers appear to be as tightly constrained as the UC HII regions and the CH_3OH masers, we surmise that the majority of detected H_2O masers are likely drawn from the same population as regions of high-mass star formation.

Given the fitted Gaussian to the Galactic latitude distribution, we can estimate the number of water masers that are detectable, but lie at Galactic latitudes outside the survey area, between Galactic longitudes of 290° and 30°. This is done by integrating under the entire Gaussian curve and comparing this number to the 540 detected masers in the area under the curve between −0.5° and +0.5°. We find that this analysis yields about 32 undetected maser sites, or 6 per cent. We expect this number of undetected masers is a lower limit. This is because, as mentioned above, the Gaussian is dominated by maser sites associated with high-mass star formation. But H_2O masers are known to also be associated with evolved stars, which have a larger scaleheight about the Galactic plane. Based on a 1612 MHz OH maser survey towards evolved stars (Sevenster et al. 1997), we estimate that the scaleheight of evolved stars is 1.5°.

Therefore, we expect more detections of water masers at higher Galactic latitudes from evolved stars. Only 15 maser sites in our survey have been associated with evolved stars, with possibly some other maser sites yet to be associated. We estimate that probably no more than 10 per cent of all detected masers will be associated with evolved stars, making them a minor contribution to the total number of masers. Assuming up to 10 per cent of masers are associated with evolved stars, which have a scaleheight of 1.5°, we estimate that no more than about 73 detectable masers lie in this region.

7.5 H_2O maser Galactic longitude distribution

Note that we have only considered the regions at greater Galactic latitudes, but within the same Galactic longitude range, as the survey area. This covers approximately 28 per cent of all Galactic longitudes. If we assume that the distribution of H_2O masers is symmetrical about the Galactic centre in the Galactic longitude, then given that there are 339 masers between $l = 290°$ and 0°, we estimate that there are at least 680 masers between $l = 290°$ and 70° and $|b| < 0.5°$. Based on the scaleheights given above, we estimate that there are about 800 detectable masers at all Galactic latitudes, within this Galactic longitude range. Without knowing the true distribution of H_2O masers in the outer Galaxy, we cannot reliably extrapolate to the number of detectable masers in the entire Galaxy. However, we expect that the remaining 45 per cent of the Galaxy will not contain as many detectable H_2O masers as the inner Galaxy, so we place an approximate upper limit of 1500 in the entire Galaxy. In conclusion, we estimate that there are between 800 and 1500 H_2O masers in the Galaxy that are detectable with a survey sensitivity comparable to HOPS.

Fig. 13 shows the distribution of H_2O masers in the Galactic longitude. There are three prominent concentrations of H_2O masers at approximately 310°, 335° and 25°. These positions in the Galaxy correspond to tangent points of Galactic spiral arms. Towards the Galactic centre, we do not find any peak in the number of H_2O masers, compared to other longitudes within 20° of the Galactic centre. This is somewhat surprising as the Galactic centre is very prominent in many spectral line tracers, such as NH_3, reported in Longmore et al. (in preparation). We will compare the positions of H_2O masers and dense molecular gas in future papers.

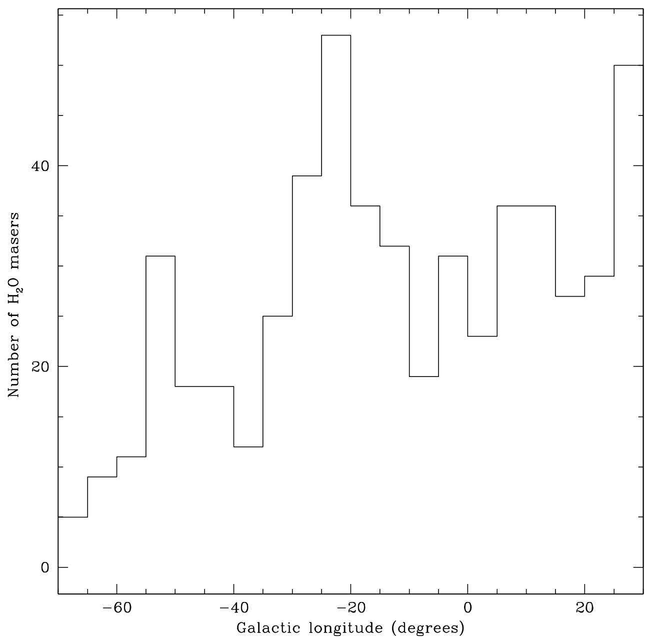

Figure 13. Galactic longitude distribution of H_2O masers detected in HOPS. Three peaks are seen at approximately 310°, 335° and 25°, which correspond to tangent points of the Galactic spiral arms. There is no prominent peak towards the Galactic centre.

8 CONCLUSIONS

We have completed observations of 100 deg^2 of the Galactic plane, using the Mopra Radio Telescope in the 12 mm band, in a survey we call HOPS (the H_2O Southern Galactic Plane Survey). Our observations concentrated on spectral line emission from the H_2O maser at 22.2 GHz, the NH_3 inversion transitions (1, 1), (2, 2), (3, 3), (6, 6) and (9, 9), HCCCN (3–2), and radio recombination lines H69α and H62α. We have reported on the survey design, covering Galactic longitudes from $l = 290°$ to 30° and Galactic latitudes $|b| < 0.5°$.

Within the survey region, we found 540 H_2O masers, of which 334 (62 per cent) are new detections. We find maser peak flux densities ranging from 0.7 to 3933 Jy, with 62 masers (9 per cent) over 100 Jy. We find maser spot velocities spread over ranges up to 351.3 km s^{-1}, with 14 maser sites showing spot velocities spread over at least 100 km s^{-1}. We estimate that at least 90 per cent of the detected masers could be associated with high-mass star formation, with the remainder being associated with evolved stars or low-mass star formation. This is based on the number of known associations of H_2O masers and evolved stars in our survey (15) and the Galactic latitude distribution of the H_2O masers, which closely resembles the distribution of high-mass star formation sites.

Our rms noise levels for the H_2O maser observations are between 1 and 2 Jy for 87 per cent of the survey, with 95 per cent of the survey having an rms noise level below 2 Jy. We estimate that the survey is 98 per cent complete down to a flux limit of about 8.4 Jy and 50 per cent complete down to about 5.5 Jy. We estimate that there are between 800 and 1500 H_2O masers in the Galaxy that are detectable in a survey with such completeness limits.

We detect possible masers in transitions of CH_3OH and NH_3. This includes the detection of NH_3 (11, 9) and (8, 6) emission towards G19.61−0.23. If these transitions are confirmed as masers, they will be only the second known examples of these transitions showing maser activity. We also report possible maser emission in the NH_3 (3, 3) line towards G23.33−0.30. If confirmed as a maser, it will be the strongest known maser in this line by at least an order of magnitude.

In Paper II (Purcell et al. in preparation) we present NH_3 (1, 1) and (2, 2) data, the source-finding algorithm and thermal line-fitting routines. Paper III (Longmore et al. in preparation) will detail properties of all other thermal lines detected in HOPS.

ACKNOWLEDGMENTS

The HOPS team would like to thank the dedicated work of CSIRO Narrabri staff who supported the observations beyond the call of duty. PAJ acknowledges partial support from Centro de Astrofísica FONDAP 15010003 and the GEMINI-CONICYT FUND. NL acknowledges partial support from the Center of Excellence in Astrophysics and Associated Technologies (PFB 06) and Centro de Astrofísica FONDAP 15010003. NL's postdoctoral position at CEA/Irfu was funded by the Ile-de-France Region. The University of New South Wales Digital Filter Bank used for the observations (MOPS) with the Mopra Telescope was provided with support from the Australian Research Council, CSIRO, The University of New South Wales, Monash University and The University of Sydney.

The Mopra Radio Telescope is part of the Australia Telescope National Facility which is funded by the Commonwealth of Australia for operation as a National Facility managed by CSIRO.

REFERENCES

Aikawa Y., Ohashi N., Inutsuka S., Herbst E., Takakuwa S., 2001, ApJ, 552, 639
Alksnis A., Balklavs A., Dzervitis U., Eglitis I., Paupers O., Pundure I., 2001, Balt A, 10, 1
Barlow M. J. et al., 1996, A&A, 315, L341
Batchelor R. A., Caswell J. L., Goss W. M., Haynes R. F., Knowles S. H., Wellington K. J., 1980, Australian J. Phys., 33, 139
Benson P. J., Little-Marenin I. R., 1996, ApJS, 106, 579
Benson P. J., Little-Marenin I. R., Woods T. C., Attridge J. M., Blais K. A., Rudolph D. B., Rubiera M. E., Keefe H. L., 1990, ApJS, 74, 911
Bergin E. A., Langer W. D., 1997, ApJ, 486, 316
Bergin E. A., Alves J., Huard T., Lada C. J., 2002, ApJ, 570, L101
Brand J. et al., 1994, A&AS, 103, 541
Braz M. A., Scalise E., Jr, 1982, A&A, 107, 272
Braz M. A., Gregorio Hetem J. C., Scalise E., Jr, Monteiro Do Vale J. L., Gaylard M., 1989, A&AS, 77, 465
Breen S. L. et al., 2007, MNRAS, 377, 491
Breen S. L., Caswell J. L., Ellingsen S. P., Phillips C. J., 2010, MNRAS, 406, 1487
Caselli P., Walmsley C. M., Tafalla M., Dore L., Myers P. C., 1999, ApJ, 523, L165
Caswell J. L., Breen S. L., 2010, MNRAS, 407, 2599
Caswell J. L., Haynes R. F., 1983, Australian J. Phys., 36, 417
Caswell J. L., Batchelor R. A., Haynes R. F., Huchtmeier W. K., 1974, Australian J. Phys., 27, 417
Caswell J. L., Batchelor R. A., Goss W. M., Haynes R. F., Wellington K. J., Yabsley D. E., Knowles S. H., Balister M., 1976, PASA, 3, 61
Caswell J. L., Batchelor R. A., Forster J. R., Wellington K. J., 1983a, Australian J. Phys., 36, 401
Caswell J. L., Batchelor R. A., Forster J. R., Wellington K. J., 1983b, Australian J. Phys., 46, 443
Caswell J. L., Batchelor R. A., Forster J. R., Wellington K. J., 1989, Australian J. Phys., 42, 331
Caswell J. L., Vaile R. A., Ellingsen S. P., Whiteoak J. B., Norris R. P., 1995, MNRAS, 272, 96
Caswell J. L., Breen S. L., Ellingsen S. P., 2011, MNRAS, 410, 1283
Churchwell E., Walmsley C. M., Cesaroni R., 1990, A&AS, 83, 119
Claussen M. J. et al., 1984, ApJ, 285, L79
Claussen M. J., Wilking B. A., Benson P. J., Wootten A., Myers P. C., Terebey S., 1996, ApJS, 106, 111
Codella C., Felli M., Natale V., Palagi F., Palla F., 1994, A&A, 291, 261
Codella C., Palumbo G. G. C., Pareschi G., Scappini F., Caselli P., Attolini M. R., 1995, MNRAS, 276, 57
Comoretto G. et al., 1990, A&AS, 84, 179
Dame T. M., Hartmann D., Thaddeus P., 2001, ApJ, 547, 792
Deacon R. M., Chapman J. M., Green A. J., Sevenster M. N., 2007, ApJ, 658, 1096
Deguchi S., Nakada Y., Forster J. R., 1989, MNRAS, 239, 825
Deguchi S., Nakashima J., Kwok S., Koning N., 2007, ApJ, 664, 1130
Di Francesco J., Johnstone D., Kirk H., MacKenzie T., Ledwosinska E., 2008, ApJS, 175, 277
Dickinson D. F., 1976, ApJS, 30, 259
Engels D., Schmid-Burgk J., Walmsley C. M., 1986, A&A, 167, 129
Evans N. J., III, 1999, ARA&A, 37, 311
Felli M. et al., 2007, A&A, 476, 373
Forster J. R., Caswell J. L., 1989, A&A, 213, 339
Forster J. R., Caswell J. L., 1999, A&AS, 137, 43
Forster J. R., Caswell J. L., 2000, ApJ, 530, 371
Gaines L., Casleton K. H., Kukolich S. G., 1974, ApJ, 191, L99
Garay G., Moran J. M., Rodriguez L. F., Reid M. J., 1998, ApJ, 492, 635
Genzel R., Downes D., 1977, A&AS, 30, 145
Genzel R., Downes D., 1979, A&A, 72, 234
Green J. A. et al., 2009, MNRAS, 392, 783
Healy K. R., Hester J. J., Claussen M. J., 2004, ApJ, 610, 835
Hinkle K. H., Barnes T. G., 1979, ApJ, 227, 923
Ho P. T. P., Townes C. H., 1983, ARA&A, 21, 239
Hunter T. R., Brogan C. L., Indebetouw R., Cyganowski C. J., 2008, ApJ, 680, 1271
Imai H. et al., 2007, PASJ, 59, 1107
Jackson J. M. et al., 2006, ApJS, 163, 145
Jaffe D. T., Guesten R., Downes D., 1981, ApJ, 250, 621
Jennings D. E., Fox K., 1982, ApJ, 254, 111
Johnston K. J., Robinson B. J., Caswell J. L., Batchelor R. A., 1972, ApJ, 10, L93
Johnston K. J., Sloanaker R. M., Bologna J. M., 1973, ApJ, 182, 67
Kaifu N., Suzuki H., Ohishi M., Miyaji T., Ishikawa S., Kasuga T., Morimoto M., Saito S., 1987, ApJ, 317, L111
Kaufmann P. et al., 1976, Nat, 260, 306
Kaufmann P., Scalise E., Jr, Schaal R. E., Gammon R. H., Zisk S., 1977, AJ, 82, 577
Kazarovets E. V., Samus N. N., Durlevich O. V., Kireeva N. N., Pastukhova E. N., 2006, Inf. Bull. Var. Stars, 5721, 1
Kleinmann S. G., Sargent D. G., Dickinson D. F., 1978, AJ, 83, 1206
Kolpak M. A., Jackson J. M., Bania T. M., Clemens D. P., Dickey J. M., 2003, ApJ, 582, 756
Kraemer K. E., Jackson J. M., 1995, ApJ, 439, L9
Kukolich S. G., 1967, Phys. Rev., 156, 83
Kukolich S. G., 1969, J. Chem. Phys., 50, 3751
Kukolich S. G., Wofsky S. G., 1970, J. Chem. Phys., 52, 5477
Lafferty W. J., Lovas F. J., 1978, J. Phys. Chem. Ref. Data, 7, 441
Le Bertre T., Heydari-Malayeri M., Epchtein N., 1988, A&A, 197, 143
Le Bertre T., Tanaka M., Yamamura I., Murakami H., 2003, A&A, 403, 943
Lilley A. E., Palmer P., 1967, ApJS, 16, 143
Longmore S. N., Burton M. G., Barnes P. J., Wong T., Purcell C. R., Ott J., 2007, MNRAS, 379, 535
McClure-Griffiths N. M., Dickey J. M., Gaensler B. M., Green A. J., Haverkorn M., Strasser S., 2005, ApJS, 158, 178
Mangum J. G., Wootten A., 1994, ApJ, 428, L33
Matthews H. E., Olnon F. M., Winnberg A., Baud B., 1985, A&A, 149, 227
Mehringer D. M., Goss W. M., Lis D. C., Palmer P., Menten K. M., 1998, ApJ, 493, 274
Mehrotra S. C., Dreizler H., Mäder H., 1985, Z. Naturforschung, 40A, 683
Messineo M., Habing H. J., Sjouwerman L. O., Omont A., Menten K. M., 2002, A&A, 393, 115
Miranda L. F., Gómez Y., Anglada G., Torrelles J. M., 2001, Nat, 414, 284
Müller H. S. P., Menten K. M., Mäder H., 2004, A&A, 428, 1019
Nassau J. J., Blanco V. M., Morgan W. W., 1954, ApJ, 120, 478
Palagi F., Cesaroni R., Comoretto G., Felli M., Natale V., 1993, A&AS, 101, 153
Palla F., Brand J., Comoretto G., Felli M., Cesaroni R., 1991, A&A, 246, 249
Peretto N., Fuller G. A., 2009, A&A, 505, 405
Poynter R. L., Kakar R. K., 1975, ApJS, 29, 87
Reid M. J. et al., 2009, ApJ, 700, 137
Santangelo G. et al., 2010, A&A, 520, 50
Scalise E.Jr, Rodriguez L. F., Mendoza-Torres E., 1989, A&A, 221, 105
Schuller F. et al., 2009, A&A, 504, 415
Sevenster M. N., Chapman J. M., Habing H. J., Killeen N. E. B., Lindqvist M., 1997, A&AS, 124, 509
Sevenster M. N., van Langevelde H. J., Moody R. A., Chapman J. M., Habing H. J., Killeen N. E. B., 2001, A&A, 366, 481
Sjouwerman L. O., Lindqvist M., van Langevelde H. J., Diamond P. J., 2002, A&A, 391, 967
Sloan G. C., Price S. D., 1998, ApJS, 119, 141
Stil J. M. et al., 2006, AJ, 132, 1158
Szymczak M., Hrynek G., Kus A. J., 2000, A&AS, 143, 269
Szymczak M., Pillai T., Menten K. M., 2005, A&A, 434, 613

Tafalla M., Myers P. C., Caselli P., Walmsley C. M., Comito C., 2002, ApJ, 569, 815
Taylor G. B., Morris M., Schulman E., 1993, AJ, 106, 1978
Taylor A. R. et al., 2003, AJ, 125, 3145
Thompson M. A., Hatchell J., Walsh A. J., MacDonald G. H., Millar T. J., 2006, A&A, 453, 1003
Urquhart J. S. et al., 2009, A&A, 507, 795
Urquhart J. S. et al., 2010, PASA, 27, 321
Voronkov M. A., Caswell J. L., Ellingsen S. P., Sobolev A. M., 2010, MNRAS, 405, 2471
Voronkov M. A., Walsh A. J., Caswell J. L., Ellingsen S. P., Breen S. L., Longmore S. N., Purcell C. R., Urquhart J. S., 2011, MNRAS, 413, 2339
Walsh A. J., Hyland A. R., Robinson G., Burton M. G., 1997, MNRAS, 291, 261
Walsh A. J., Burton M. G., Hyland A. R., Robinson G., 1998, MNRAS, 301, 640
Walsh A. J., Macdonald G. H., Alvey N. D. S., Burton M. G., Lee J.-K., 2003, A&A, 410, 597
Walsh A. J., Longmore S. N., Thorwirth S., Urquhart J. S., Purcell C. R., 2007a, MNRAS Lett., 382, 35
Walsh A. J., Myers P. C., Di Francesco J., Mohanty S., Bourke T. L., Gutermuth R., Wilner D., 2007b, ApJ, 655, 958
Walsh A. J., Lo N. Burton M. G., White G. L., Purcell C. R., Longmore S. N., Phillips C. J., Brooks K. J., 2008, PASA, 25, 105
Walsh A. J., Breen S. L., Bains I., Vlemmings W. H. T., 2009, MNRAS, 394, L70
Westerlund B. E., Olander N., 1978, A&AS, 32, 401
Willacy K., Langer W. D., Velusamy T., 1998, ApJ, 507, L171
Wood D. O. S., Churchwell E., 1989a, ApJS, 69, 831
Wood D. O. S., Churchwell E., 1989b, ApJ, 340, 265
Zhang Q., Ho P. T. P., 1995, ApJ, 450, L63

This paper has been typeset from a TEX/LATEX file prepared by the author.